

VOIDS AS PROBES OF THE NATURE OF DARK ENERGY
Groot Onderzoek thesis

PATRICK (E.G.P.) BOS
Supervisor: Rien van de Weijgaert
Kapteyn Astronomical Institute, University of Groningen

July 6, 2010



Image: slice of a void-rich region of the Millennium Simulation (Springel et al., 2005), blended with an image of the void-like region of the skull of H.J. Simpson, pondering the nature of dark energy.

1	Introduction	4
1.1	Background and definitions	6
1.2	Dark energy	7
1.2.1	Modeling (time dependent) dark energy	9
1.2.2	Models of dark energy used in this thesis	10
1.2.3	General parameterization	14
1.2.4	Probes of dark energy	14
1.3	Voids	15
1.3.1	Void evolution	15
1.3.2	Void shapes	18
1.3.3	Observing voids	20
2	Data	24
2.1	Producing simulations with GADGET	24
2.2	Dark matter particles	25
2.2.1	High resolution	26
2.2.2	Low resolution	30
2.3	Redshift space	30
3	Structure finding	35
3.1	Halo	35
3.1.1	Friends-of-Friends group finder	36
3.1.2	SUBFIND halo finder	36
3.1.3	Halo data	38
3.2	Voids	39
3.2.1	Watershed Void Finder	39
3.2.2	Void properties	43
4	Analysis	45
4.1	Introduction	45
4.2	Density field	46
4.3	Point distribution statistics	48
4.3.1	One-point probability density function	48

4.3.2	Two-point correlation function	51
4.4	Void Probability Functions	52
4.4.1	Void probability function	52
4.4.2	Modified void probability function	56
4.5	Void Morphology Parameters	62
4.5.1	Volume and shape distributions	62
4.5.2	Shape versus redshift	65
5	Summary and discussion	73
5.1	Results from our probes	73
5.1.1	Summary	73
5.1.2	Theory: results from N-body simulations	74
5.1.3	Practice: results from (simulated) observations	75
5.2	The σ_8 degeneracy problem	77
5.3	Open questions	78
6	Conclusions	80
	Acknowledgements	81
A	Coffee and cream	90
B	“Concordance” Cosmology	91
C	Research plan	93
C.1	Motivation and goals	93
C.2	Methods	93
C.3	Research plan	94

The fact that we seem to be drawing a fairly decent picture of the global physics governing the observable universe in the form of “concordance” cosmology, does not in the slightest imply that we understand the intricate details that abound in the structures of our cosmos. We can summarize the universe as a whole in a few equations and parameters. However, we are only beginning to understand what the implications of our models are for other structures in the universe. Neither do we know the exact underlying causes of the behaviour of our universe as we observe it.

It is in the nature of (astro)physicists to try to understand every natural phenomenon on every possible scale. In this light, cosmology and particle physics can be seen as two extreme approaches to this goal (see figure 1.1). Results from cosmology can be used to provide hints on where to look for new particles in particle physics and vice versa: new-found particles can be used to explain cosmological results or even lead towards new approaches for observing the universe. These two different yet complementary fields will undoubtedly lead to new insights in the laws of physics.

One of today’s greatest puzzles is that of the nature of the dark components of our universe: dark matter (DM) and dark energy (DE). Making up respectively 21.7% and 73.8% of the total cosmic energy content (Komatsu et al., 2010), a total of 95.5%, our ignorance of its true nature is embarrassing. Up to now, attempts at understanding these enigmas of modern science have been largely theoretical in nature. We have no compelling evidence of the precise nature of DM and DE (Komatsu et al., 2010; Amanullah et al., 2010). Whereas by now we largely agree on several physical properties of DM, e.g. that the bulk of it must be cold¹ and that it interacts with baryonic matter mainly through gravity, we have no such clues about DE, making it an even greater mystery. The best we can manage on the subject is a plethora of highly abstract and generalised field theories. Observational constraints, however, are continuously closing in and although we still have quite a lot of unexplored parameter space, it may not be long before we approach some equilibrium and will be able to exclude some of our most esoteric models.

Until the time when we can use our observations and experiments to pin down the

¹Where “cold” means slowly moving with respect to the Hubble expansion, at the time of decoupling of the DM species from the rest of matter and radiation. It is contrasted with “hot” DM, which moves relativistically.

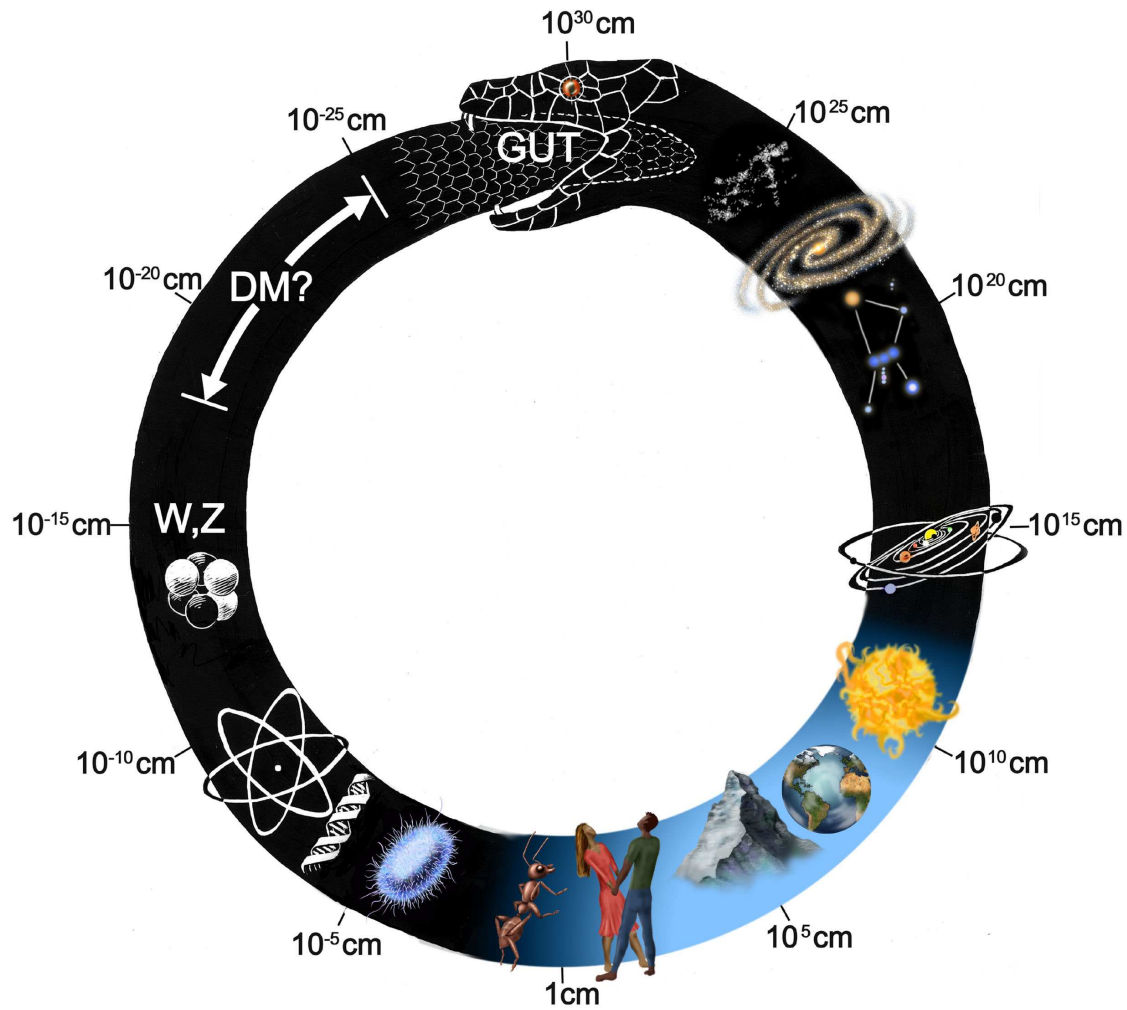


Figure 1.1: Uroboros, the cosmic snake biting its own tail. It represents the different scales of physical phenomena and the hope that one day the most extreme scales can be described by the Grand Unified Theory, the holy grail of current day physics. Image from Primack and Abrams (2007).

nature of DM and DE, we must prepare ourselves. We should follow recent attempts like ESA's EUCLID mission (Cimatti et al., 2009) and try to find reliable probes for determining the exact nature of dark energy. In this thesis we aim to do just that by trying to find probes of the nature of DE. Specifically, we are interested in the effects of time dependent DE models. In this, we specifically concentrate on voids. Recent studies (Park and Lee, 2007; Lee and Park, 2009; Lavaux and Wandelt, 2010) have pointed out that voids may be very sensitive probes of DE.

Before we delve into the specifics of the DE models we review some of the necessary background and definitions from cosmology and cosmic structure formation. Following this general introduction, we will treat time dependent models of dark energy. In the final section of this chapter, we will provide the arguments of why we expect voids to be an interesting probe of dark energy.

The outline of the rest of this thesis is as follows. First we will give a description of the data (both quantitatively and qualitatively) in chapter 2. Structure finding algorithms, like halo and void finders, are invaluable to our analysis and we will elaborate on them in chapter 3. In chapter 4 we list the results from our analysis of the data. We conclude with a summary and discussion chapter 5 and conclusions in chapter 6.

1.1 Background and definitions

The standard reference point for cosmological research like our own is that of ‘‘concordance’’ cosmology (Ostriker and Steinhardt, 1995). This model of the universe is based on the cosmological principle that states that, on large scales, the universe is homogeneous and isotropic. Under these two assumptions, we can derive from Einstein's equations the Friedmann-Lemaître-Robertson-Walker (FLRW) metric. We end up with the Friedmann equations that govern the dynamics of homogeneous and isotropic universes (see appendix B for a slightly more detailed derivation).

In this model the universe is made up of four main components: baryonic matter, dark matter, radiation and dark energy (as modelled by a cosmological constant Λ). The relative energy densities of these components are usually given as a fraction of the so-called critical density ρ_c . The critical density is the density of a spatially flat universe (one of the three possibilities in a FLRW metric). We then define for each component i the density parameter

$$\Omega_i \equiv \frac{\rho_i}{\rho_c}. \quad (1.1)$$

The actual densities, obtained from the most recent (7th year) release of the WMAP data (Komatsu et al., 2010; Larson et al., 2010) are the following:

$$\Omega_b = 0.0445, \quad \Omega_r = 0.005, \quad \Omega_d = 0.217, \quad \Omega_\Lambda = \frac{\Lambda}{3H^2} = 0.738. \quad (1.2)$$

The dynamics of our universe in terms of these contributions may be inferred from the Hubble parameter H :

$$H^2 = H_0^2 \left[\frac{\Omega_r}{a^4} + \frac{\Omega_b + \Omega_d}{a^3} + \frac{1 - \sum_i \Omega_i}{a^2} + \Omega_\Lambda \right], \quad (1.3)$$

where a is the cosmological scale factor and $H \equiv \dot{a}/a$. Another important dynamical

aspect is described by the Friedmann equation for the acceleration of the expansion \ddot{a} :

$$\frac{\ddot{a}}{a} = -\frac{4\pi G}{3} \left(\rho + \frac{3P}{c^2} \right), \quad (1.4)$$

where ρ is the energy density and P is the pressure of the universal components.

In the realm of structure formation, we usually do not talk about the total density ρ , nor do we use Ω . The essence of structure formation is that it deals with departures from the initial homogeneous state of the universe. This means that it is far more illustrative to look at perturbations from the average state of things. In the case of densities we define the density contrast parameter $\delta_i(x)$:

$$\delta_i(x) = \frac{\rho_i(x) - \bar{\rho}_i}{\bar{\rho}_i}, \quad (1.5)$$

where $\bar{\rho}_i$ is the average density of that specific component. We usually do not write the subscript for the matter density contrast δ_m , but simply define

$$\delta = \delta_m = \delta_b + \delta_{dm}. \quad (1.6)$$

Analogously to the density contrast parameter, we can define perturbative measures of the velocity of objects and the gravity pulling on them. We call these the peculiar velocity and gravity. The velocity from the Hubble expansion is subtracted from the total velocity which leaves the peculiar velocity v :

$$v = u - Hr, \quad (1.7)$$

where u is the total physical velocity and Hr is the velocity caused by the expanding universe. The peculiar gravity is defined similarly.

The above equations, together with equations from the dynamic equations of structure formation (which we describe below), have proven to give an accurate description of the universe. The cosmic web that we observe in large galaxy surveys can be modelled using the framework of concordance cosmology. Be that as it may, no model is perfect and as long as there is room in the observational constraints we should explore every possibility left. One avenue of possibility is that of time dependent models of dark energy. These models we will explore in the next section.

1.2 Dark energy

The history of dark energy starts when Einstein first introduces a cosmological constant Λ in his equations². He used it to ‘correct’ for the fact that his model described an expanding or contracting universe, because he believed the universe to be static. When, later on, Hubble showed that in fact the universe is expanding, Λ was discarded, only to return by the end of 20th century.

By this time, it was inferred from observations of SNe type Ia that the universal expansion was in fact accelerating (Riess et al., 1998; Perlmutter et al., 1999). Later observations still yield the same result (Leibundgut, 2001; Amanullah et al., 2010). This

²The term “dark energy” is coined much later. Its first appearance in the literature was in a preprint version of Huterer and Turner (1999).

cosmic behaviour can be explained by assuming a non-zero value for Einstein’s cosmological constant. In analogy to dark matter, the source of this cosmological constant would soon be called “dark energy”³. Recent reviews on dark energy are Frieman et al. (2008) and Caldwell (2009).

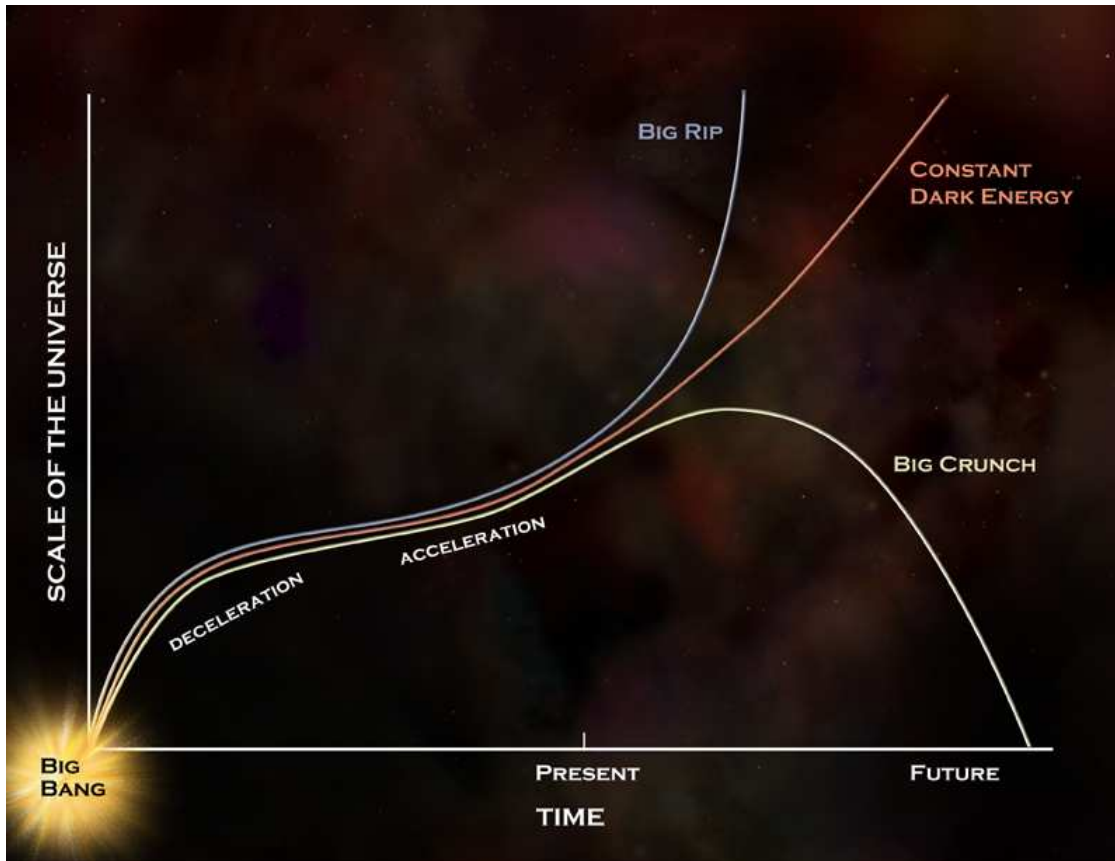


Figure 1.2: Three possible futures for the universe. “If dark energy is constant, as the new Chandra results suggest, the expansion should continue accelerating forever. If dark energy increases, the acceleration may happen so quickly that galaxies, stars, and eventually atoms will be torn apart, in the so-called Big Rip. Dark energy may also lead to a recollapse of the Universe, in the Big Crunch. The illustration also shows the early decelerating expansion of the Universe, followed by the accelerating phase that started about 6 billion years ago.” Image and text from <http://chandra.harvard.edu/photo/2004/darkenergy/more.html>.

In 1.2 we show the expansion of the universe in several cases. A model with a cosmological constant with a constant density of $\Omega_{\Lambda} \approx 0.7$ will undergo accelerated expansion forever. If, however, the amount of dark energy increases or decreases with time, the universe may see a more violent end. In the first case the universal expansion would eventually accelerate so quickly that all matter and even atoms will be torn apart.

³Note that dark energy and the cosmological constant are not the same. Dark energy represents the right-hand side of Einstein’s field equation (the part describing the energy content of the universe), whereas the cosmological constant is on the left-hand side of the equation as part of the description of the curvature of the universe.

In the second case, the universe would undergo the reverse of a Big Bang called a Big Crunch.

The precise nature of dark energy will be a decisive factor in the fate of the universe. Modeling this cosmic component is therefore of the utmost importance. In what follows, we will elaborate on the general theory needed to describe models of dark energy. Furthermore, we shall introduce the models that we have considered in this thesis.

1.2.1 Modeling (time dependent) dark energy

On cosmological (Mpc) scales our universal constituents (matter, radiation, dark energy, etc.) can be described as continuous “cosmological fluids”. On large scales we thus need not concern ourselves with the discreteness of matter and other constituents. Rather we simply describe each constituent j by the general equation of state for a cosmological fluid:

$$P_j = w_j \rho_j, \quad (1.8)$$

where we use natural units of $c = 1$. We typically assume for matter that $w_m = 0$, i.e. all matter in the universe is a pressureless “dust”. Radiation is best described as a relativistic fluid for which $w_r = 1/3$. w_{DE} is constrained by the fact that it must cause an acceleration of the rate of expansion (Kowalski et al., 2008; Hicken et al., 2009; Amanullah et al., 2010). We can see what this means by looking at equation 1.4 for the acceleration of the expansion factor. We can replace P by the expression in equation 1.8 (setting $c = 1$):

$$\frac{\ddot{a}}{a} = -\frac{4\pi G}{3}(\rho + 3w\rho). \quad (1.9)$$

a is positive by definition, so this means that for the acceleration \ddot{a} to be positive, we must have

$$\rho + 3w\rho < 0, \quad (1.10)$$

from which we can conclude that

$$w_{\text{DE}} < -\frac{1}{3}. \quad (1.11)$$

Solutions for $a(t)$ in a universe with dark energy can be found by looking at the most general form of the Friedmann equation in a flat universe ($\sum_j \Omega_j = 1$) containing constituents j :

$$\left(\frac{H}{H_0}\right)^2 = \sum_j \Omega_{0,j} \exp\left(-3 \int_{a_0}^a \frac{1 + w_j(a')}{a'} da'\right), \quad (1.12)$$

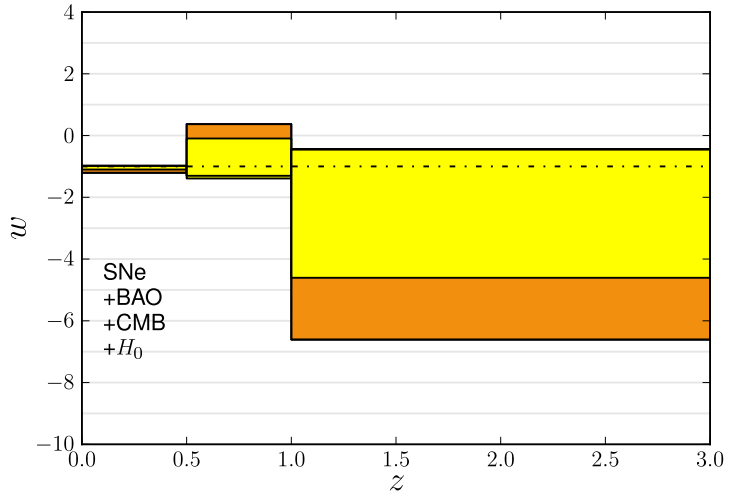
where the equation of state parameter w_j can be time dependent. For a constant w_j we have

$$\left(\frac{H}{H_0}\right)^2 = \sum_j \Omega_{0,j} \exp\left(-3(1 + w_j) \ln \frac{a}{a_0}\right) = \sum_j \Omega_{0,j} \left(\frac{a}{a_0}\right)^{-3(1+w_j)}. \quad (1.13)$$

Focussing on the dark energy component (neglecting the influence of other components) we have

$$\left(\frac{\dot{a}}{a}\right)^2 \propto a^{-3(1+w_{\text{DE}})}, \quad (1.14)$$

Figure 1.3: Constraints on the dark energy equation of state parameter $w(a)$. The value of $w(a)$ is taken to be constant in each bin. Image from Amanullah et al. (2010), composed using all of the most recent data (from SNe and the WMAP seven year data) from Hicken et al. (2009); Holtzman et al. (2008) and Komatsu et al. (2010).



which has two solutions of the form

$$a \propto \begin{cases} t^{\frac{2}{3} \frac{1}{1+w_{\text{DE}}}} & \text{if } w \neq -1, \\ e^t & \text{if } w = -1. \end{cases} \quad (1.15)$$

By taking the time derivative of the equation for $w \neq -1$ it is again easily seen that for accelerated expansion to happen, we need $\frac{2}{3} \frac{1}{1+w_{\text{DE}}} - 1 > 0$, from which we see that $w_{\text{DE}} < -\frac{1}{3}$.

In many studies the lower boundary of $w_{\text{DE}} \geq -1$ is also adopted. We call the region below this value the “phantom regime” (Hawking and Ellis, 1973; Linder, 2008). Dark energy in this regime will cause a Big Rip in which the expansion accelerates so rapidly that eventually even the strong atomic forces will not be strong enough to keep atoms together. Interestingly enough, neither theoretically nor observationally (see figure 1.3) can this form of DE be ruled out. Involving superluminal velocities, it may cause problems with causality (Caldwell, 2009). We will therefore not consider models in this regime.

1.2.2 Models of dark energy used in this thesis

We describe below the specific models of dark energy that we have investigated. As explained above, dark energy has its influence on cosmology through the Friedmann equation. Hence, we show how for each model this equation is derived.

Our reference model is a universe containing cold dark matter and a cosmological constant: Λ CDM. We compare this model to four different models of time dependent dark energy. We use two quintessence models, in which the dark energy is described as a scalar field under the influence of a potential. The other two models are extended quintessence models, where the scalar field is coupled to gravity.

In the following we set $a_0 = 1$. We assume a universe with flat geometry, i.e. without curvature. The equations used to determine $w(a)$ are given. The resulting relations for the different models are shown in figure 1.4.

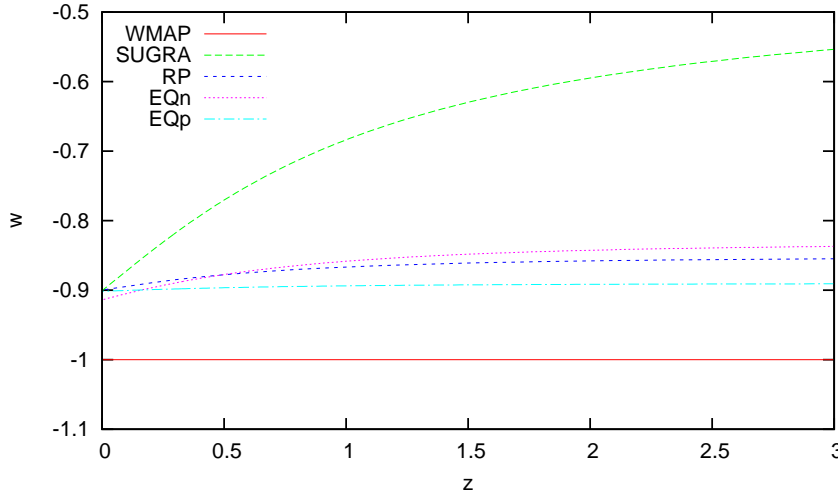


Figure 1.4:
Evolution of the equation of state parameter $w = P/\rho$ of dark energy for different models.

Cosmological constant

Dark energy in a Λ CDM cosmology is modelled by a cosmological constant with $w_\Lambda = -1$. The Friedmann equation for this model in a flat universe is given as

$$\left(\frac{H}{H_0}\right)^2 = \frac{\Omega_{0,m}}{a^3} + \frac{\Omega_{0,r}}{a^4} + \Omega_{0,\Lambda}. \quad (1.16)$$

This situation also applies to concordance cosmology.

Quintessence

We first consider a dynamical model of dark energy as described by a simple non-interacting scalar field ϕ . A scalar field is a basic quantity of field theory that assigns to each point in space a scalar value. The essential point in describing dark energy as a scalar field ϕ is that it gives dark energy a new degree of freedom. We can use this degree of freedom to describe the dynamical properties that we would like the dark energy to have (Frieman et al., 2008). This is done by introducing a potential $V(\phi)$ in the equation of motion of the scalar field (described below). From quantum field theory we learn that the equation of motion of a scalar field is the Klein-Gordon (KG) equation, which is a relativistic version of the Schrödinger equation. We list the KG equations for the specific models of quintessence we have used. The equation of motion and the potential completely describe the dynamics of the model of dark energy.

Dark energy modelled by a scalar field ϕ in a potential $V(\phi)$ is called “quintessence” dark energy (Wetterich, 1988; Ratra and Peebles, 1988). This model has $w = w(a)$ and the Friedmann equation is

$$\left(\frac{H}{H_0}\right)^2 = \frac{\Omega_{0,m}}{a^3} + \frac{\Omega_{0,r}}{a^4} + \Omega_{0,\phi} \exp\left(-3 \int_{a_0}^a \frac{1 + w_\phi(a')}{a'} da'\right), \quad (1.17)$$

where

$$w_\phi = \frac{P_\phi}{\rho_\phi} = \frac{\frac{1}{2}\dot{\phi}^2 - V(\phi)}{\frac{1}{2}\dot{\phi}^2 + V(\phi)}. \quad (1.18)$$

Note that when the kinetic term $\dot{\phi}$ vanishes, we regain the Λ CDM value of $w = -1$. The cosmological constant can thus be seen as a special case of the more general quintessence model of dark energy. We can solve for ϕ using the KG equation:

$$\ddot{\phi} + 3H\dot{\phi} + \frac{\partial V(\phi)}{\partial \phi} = 0. \quad (1.19)$$

The crucial part in this model is the potential $V(\phi)$ which determines the model's properties. If we choose it properly we can use it to overcome both the fine-tuning problem⁴ and the coincidence problem⁵. Another desirable characteristic is that the model can be motivated by particle physical considerations. In practice, this means that the model is derived on a quantum field theoretical basis using the Lagrangian formalism and keeping constraints like Lorentz invariance in mind. Quintessence models fulfill all these desiderata by construction. We refer to Linder (2008) and Copeland et al. (2006) for comprehensive reviews on the general dynamical properties of quintessence models.

We have used an inverse power law potential (Ratra and Peebles, 1988) and a generalised inverse power law potential (Brax and Martin, 2000). The latter potential expands upon the former by including corrections from supergravity (Freedman et al., 1976), the supersymmetric version of general relativity. These models, which we will later refer to as RP and SUGRA respectively, have the following potentials:

$$V_{\text{RP}}(\phi) = \frac{\Lambda^{4+\alpha}}{\phi^\alpha} \quad (1.20)$$

$$V_{\text{SUGRA}}(\phi) = \frac{\Lambda^{4+\alpha}}{\phi^\alpha} \exp(4\pi G\phi^2), \quad (1.21)$$

where $\alpha \geq 0$ and Λ are free parameters.

These are both “tracker” potentials. This means that they have the convenient property that the current day ϕ_0 is independent of its initial conditions. In other words: ϕ will always approach a certain value, meaning that we can use these potentials to solve the coincidence problem. With these potentials, at early epochs the field's density will closely track the radiation density. After matter-radiation equality it will roll down the potential to become the dominant cosmic component it is nowadays. This solution thus also solves the fine-tuning problem. It naturally leads to the right energy scale of dark energy.

Extended Quintessence

Both a cosmological constant and quintessence are represented as free scalar fields. They do not interact with the other species in the universe. We could easily imagine a different case in which a scalar field couples to the rest of the universal components through gravity (Boisseau et al., 2000). Specifically, we consider here the so-called “extended

⁴The natural (Planck) energy scale for dark energy from particle physics is more than 100 orders of magnitude larger than realistic estimates. To remove this large contribution from the models a negative term of almost the same size must be introduced. Fine-tuning is necessary to get exactly the behaviour we need dark energy to have. This problem is called the fine-tuning problem. Quintessence can remove this problem, as it can naturally lead to the right amount of dark energy.

⁵The coincidence problem is that it seems very coincident that accelerated expansion started when it did. If it had started earlier, structure as we know it might never have formed. We leave it to the reader to decide whether this is an actual problem or just one of the coincidences of life.

quintessence" (EQ) models of Perrotta et al. (2000); Baccigalupi et al. (2000); Perrotta and Baccigalupi (2002); Pettorino et al. (2005) and Pettorino and Baccigalupi (2008). The way we represent an interaction in field theory is by adding the so-called interaction term to the action of the field. This term is a (Lorentz invariant) product of the quantities that represent the fields that we want to interact. In our case these are the gravitational field represented by the Ricci scalar R and the extended quintessence field ϕ . The action then becomes (Baccigalupi et al., 2000)

$$S = \int d^4x \sqrt{-g} \left[\frac{1}{2} F(\phi) R - \frac{1}{2} \partial^\mu \phi \partial_\mu \phi - V(\phi) + L' \right], \quad (1.22)$$

where L' contains the terms of the Lagrangian without ϕ . $F(\phi)$ is given by

$$F(\phi) = \frac{1}{8\pi G} + \xi (\phi^2 - \phi_0^2), \quad (1.23)$$

where ξ determines the strength of the interaction and $\phi_0 = \phi(t_0)$.

The two models we consider are those with a positive and a negative value of ξ (referred to as EQp and EQn hence forward). These two models differ slightly in the era of matter dominance (i.e. from $z > 1$ to the radiation dominated era), but are otherwise largely similar (Pettorino and Baccigalupi, 2008).

Of course, interaction works both ways. Were we to implement these models very strictly, we would have to alter our N-body code by making the gravitational constant G time dependent (Pettorino and Baccigalupi, 2008). Luckily, we can make the model approach the limit of GR by making sure that $w_{JBD} \gg 1$, where

$$w_{JBD} \equiv \frac{F(\phi)}{[\partial F(\phi)/\partial \phi]^2} = \frac{\frac{1}{8\pi G} + \xi (\phi^2 - \phi_0^2)}{4\xi^2 \phi^2}. \quad (1.24)$$

Using this relation we can determine the allowed values of ξ . The lower limit for $w_{JBD,0}$ (and thus the upper limit for the interaction term ξ , because $w_{JBD,0} \propto \xi^{-2}$) can be determined by observations. On cosmological scales this limit, as obtained using WMAP1 and 2dF data, is set at $|w_{JBD,0}| > 120$ (Acquaviva et al., 2005). Because we want the interaction to be as strong as possible within observational limits we indeed set ξ using this value; $w_{JBD,0} = 120$ for EQp and $w_{JBD,0} = -120$ for the EQn model. Thus the limit of GR is reached and we need not alter our N-body code.

The value of w for the EQ models is again determined by the density and pressure:

$$\rho_\phi = \frac{1}{2} \dot{\phi}^2 + V(\phi) - 3H\dot{F}(\phi) + 3H^2 \left(\frac{1}{8\pi G} - F(\phi) \right) \quad (1.25)$$

$$P_\phi = \frac{1}{2} \dot{\phi}^2 - V(\phi) + \ddot{F}(\phi) + 2H\dot{F}(\phi) - \left(2\dot{H} + 3H^2 \right) \left(\frac{1}{8\pi G} - F(\phi) \right), \quad (1.26)$$

where the field ϕ evolves according to the KG equation:

$$\ddot{\phi} + 3H\dot{\phi} + \frac{\partial V(\phi)}{\partial \phi} = \frac{1}{2} \frac{\partial F(\phi)}{\partial \phi} R. \quad (1.27)$$

1.2.3 General parameterization

In the literature on quintessence a general parameterization of the time dependence by Linder (2003) is often used:

$$w(a) = w_0 + w_a(1 - a). \quad (1.28)$$

The first obvious advantage of a parameterization is that we can use it as a general framework for comparative purposes. As sketched above, the details of different quintessence models require lots of unrelated parameters, which make comparing different models very difficult. This specific parameterization was shown to fit to a large number of models very well (Linder, 2003). In fact, current observational errors would render further parameterization useless, as the fitting errors are smaller than what can be reached in observations. In other words, parameterization in w_0 - w_a space “faithfully preserves the information to better than the precision level of the data” (Linder, 2010). With only two parameters, it is also a very manageable parameterization.

<i>Model</i>	WMAP3	RP	SUGRA	EQp	EQn
w_a	0.0	0.0564	0.452	0.0117	0.0805

Table 1.1: Fits of dark energy model parameters w_a to the $w(a)$ relations in figure 1.4, determined using a χ^2 fit.

Indeed, the models we have used can also be fit to this parameterization. Using a simple χ^2 fitting procedure with w_a as a free parameter (w_0 are fixed to the values that were chosen for the simulations) we find the best fits as given in table 1.1 (and again in table 2.1).

1.2.4 Probes of dark energy

In the years since its discovery by the use of SNe Ia, the number of probes of dark energy has steadily increased. A few of these probes we list here.

The first probe of the accelerating expansion were the measurements of supernovae type Ia (Riess et al., 1998; Perlmutter et al., 1999). SN Ia are assumed to be excellent standard candles over large distances (Phillips, 1993). This means that by measuring their apparent magnitude we can directly infer their distances, because we know their absolute magnitudes. By comparing the measured distance moduli $m - M$ to the expected values from cosmological models, they found that there was a discrepancy. This discrepancy was shown to prove that the universal expansion must have been accelerating for the last 5 Gyr.

Another important piece of evidence for dark energy was found in the anisotropy of the cosmic microwave background (CMB). The CMB probes the distribution of matter in the very early stages of the universe (about 380000 years after the Big Bang). The angular power spectrum of CMB temperature anisotropies (Amanullah et al., 2010) contains a lot of cosmological information. This can be inferred by modelling the coupling of radiation and matter at those times and predicting the effects this will have. One of these effects is that of gravity producing sound waves in the matter-photon distribution. These waves make their imprint on the CMB power spectrum and this can be used to constrain cosmological parameters. These measurements indicate that the universe is

nearly spatially flat, which means that $\sum_i \Omega_i = 1$. When we combine this measurement with the independent measurements of the large scale structure that tell us that matter only constitutes about a quarter of the total energy of the universe we can conclude that there must be some other cosmic component making up the rest of the energy. Dark energy nicely fills this gap (Frieman et al., 2008).

Other probes of dark energy include gravitational lenses, baryonic acoustic oscillations, x-ray clusters and the ages of the oldest stars as compared to the inferred age of the universe (Frieman et al., 2008). Recently, these different probes have been combined to further pin down dark energy and other cosmological parameters (Amanullah et al., 2010). Through the combination of different measures, degeneracies can be broken and the allowed parameter space can be significantly reduced. For this reason, it is of great importance to find even more probes of dark energy. In the next section we discuss why voids may be a good additional probe. Voids may be able to provide a precision probe of the nature of dark energy, i.e. of its equation of state $w(z)$. The need for good probes of the equation of state is especially pressing. This quantity is very hard to measure; intrinsically due to its relatively small effect as well as due to observational errors (Frieman et al., 2008).

1.3 Voids

Why use voids as a probe of these models of dark energy? To answer this question we must first get a firm grasp on the idea of what a void is. This is a matter of great debate, that has been ongoing since the first mention of voids (Gregory and Thompson, 1978).

Ranging from a few to several tens of megaparsecs, voids are enormous regions that are practically devoid of galaxies. They have been known to be a prominent feature of the galaxy distribution since the first redshift surveys (Chincarini and Rood, 1975; Gregory and Thompson, 1978; Einasto et al., 1980). In the SDSS survey (see figure 1.9) these relatively empty regions are clearly visible. The voids are enclosed by the other features of the cosmic web: “walls”, filaments and the massive clusters at their vertices.

We clearly see the voids in galaxy distributions (see e.g. figure 1.9) and in simulations (e.g. in the center of figure 1.5). An important question is how we should quantify these empty regions. This question has led to a large number of different definitions and void finding algorithms based on those definitions (see figure 1.10, which was taken from Colberg et al. (2008), for a comparison between algorithms). These definitions are not necessarily in agreement on important aspects like void sizes and shapes. It is therefore crucial to know as much as we can on the different methods used.

In order to fully understand the void in whatever shape or form, we need to understand not only what they might look like today, but also how they are formed and how they can evolve. To achieve this, we will delve into the story of large scale structure formation, as seen from the void perspective.

1.3.1 Void evolution

To illustrate the basic tenets of void evolution we review some results on the simplest possible model of a void as an isolated underdensity ($\delta < 0$). This underdensity induces

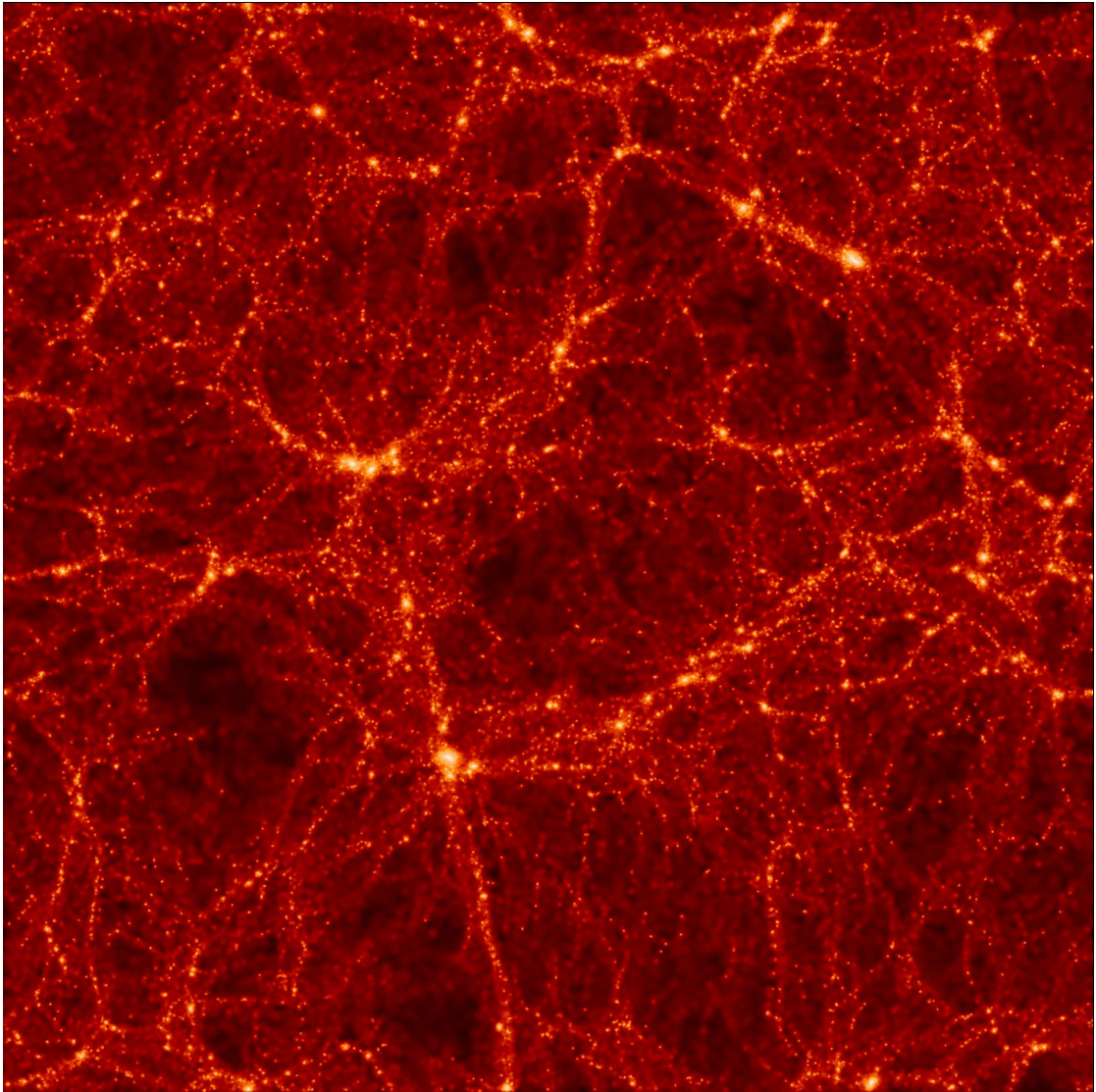


Figure 1.5: Slice of the GIF simulation in which N-body simulations were combined with semi-analytic models to study the formation and evolution of galaxies. A relatively empty region is visible in the center of the box. Although we can clearly distinguish this feature by eye, it is a non-trivial matter to quantify these structures.

an effective outward peculiar gravity that makes the underdensity expand⁶. The initial density profile of the void is an upward slope towards the overdense regions surrounding it. This slope causes matter in the central parts of the void to undergo a larger outward acceleration than the matter on the underdensity’s outskirts. If we assume the underdensity to be an isotropic sphere, we can define shells i with $\delta = \delta_i$, where $\delta_i(r_i) < \delta_j(r_j)$ if $r_i < r_j$. The inner shells will eventually overcome the outer shells due to their large peculiar acceleration. After this shell crossing event, the peculiar gravity will no longer be larger and the shells will merge and expand outwards together (van de Weygaert and Platen, 2009).

This process will cause the void to evolve toward a spherical ‘bucket-shape’ (Icke, 1984; van de Weygaert and van Kampen, 1993). This is illustrated in figure 1.6 where a one-dimensional density profile is shown for different timesteps. The sweeping out of matter in the inner regions leaves behind a very flat density profile with $\delta \approx -0.8$ at the time of shell crossing. Matter accumulates at the edges where it is driven ever outward due to its peculiar velocity and the Hubble flow. The way in which this happens was predicted to cause any asphericity in the initial underdensity to disappear. An initial isolated underdensity will form a spherical void (Icke, 1984).

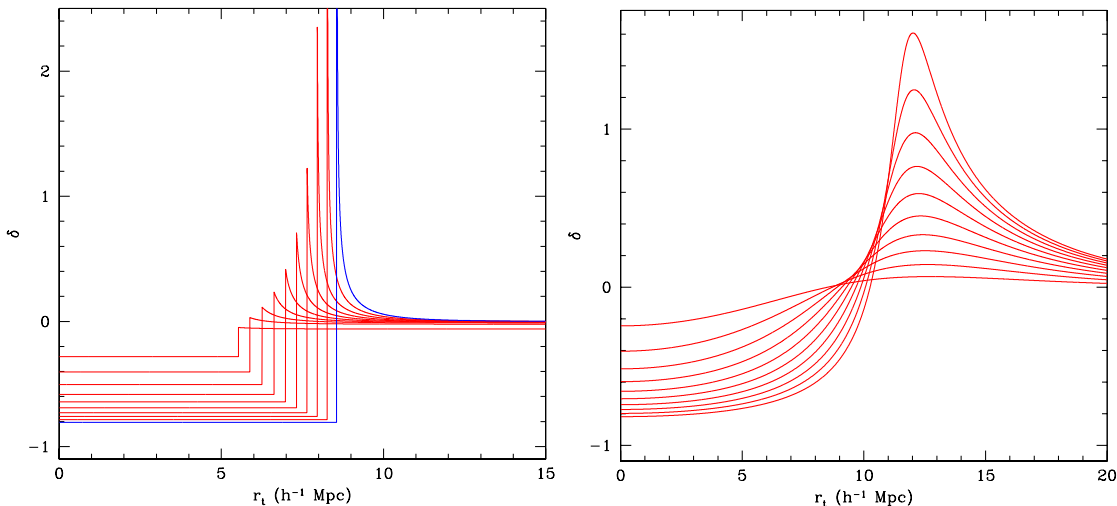


Figure 1.6: “Spherical model for the evolution of voids. Left: a pure (uncompensated) tophat void evolving up to the epoch of shell-crossing. [...] initial (comoving) radius [was] $r_i = 5.0h^{-1}\text{Mpc}$. Right: a void with [the average profile of a void in a CDM cosmology. Same initial density deficit w.r.t. the surroundings and same initial (characteristic) radius.] The tendency of this void to evolve into a tophat configuration by the time of shell crossing is clear. Shell-crossing, and the formation of a ridge, happens only if the initial profile is sufficiently steep” (van de Weygaert and Platen, 2009).

In reality voids will not be isolated. They will soon encounter other voids, clusters, filaments and walls. Icke (1984) proposed that due to the voids evolving towards

⁶The more common way of looking at this process is that the overdense regions around the underdensity start collapsing. Matter leaves the underdense regions to flow towards these ever increasing overdensities where structures like clusters, galaxies and stars will start forming. It is simply a matter of perspective; describing structure formation from both points of view is equivalent and should lead to the same results.

sphericity, they will drive matter outward and squeeze it in between meeting voids. This would form walls from which the matter would eventually be evacuated, leaving only filaments and clusters. However, this model was oversimplified, as it turned out that only the inner parts of voids can be properly described by a spherical profile. Due to the influence of surrounding structures, voids will in general not be spherical (van de Weygaert and van Kampen, 1993).

Two other important factors in the evolution of voids are the merging of voids and the collapse of voids. Voids are not the simple isotropic structures we would like them to be. They contain a lot of substructure and in a lot of cases small voids can be identified within larger ones; there is a hierarchy of voids (Dubinski et al., 1993; Sheth and van de Weygaert, 2004). This “void-in-void” hierarchy evolves through the process of voids meeting up and merging into larger voids. The substructures in these merger voids survive for a long time, but gradually dilute. In contrast, voids that live inside a large overdensity (“voids-in-clouds”) may eventually collapse due to the overdensities’ mutual attraction. In this case collapse will happen fastest in one direction, causing the void to become more and more ellipsoidal, until it totally flattens. The existence of both merging and collapsing voids shows that the simple spherical model will be unlikely to describe the majority of voids. In the next section we will therefore describe a more sophisticated model of the void shape distribution.

1.3.2 Void shapes

First emphasized by Bond et al. (1996) and recently confirmed in N-body simulations by Platen et al. (2008), the shapes of voids are intimately connected to the tidal forces induced by the large scale distribution of matter in the universe. The traceless tidal tensor T_{ij} completely describes the tidal force field. It is defined as the second derivative of the gravitational potential ϕ :

$$T_{ij} = \frac{\partial^2 \phi}{\partial x_i \partial x_j} - \frac{1}{3} \nabla^2 \phi \delta_{ij}. \quad (1.29)$$

According to Park and Lee (2007) the elliptical shape parameters of a void can be directly linked to the local tidal tensor. In what follows, we list only the most important relations; see Park and Lee (2007), Lavaux and Wandelt (2010) and Biswas et al. (2010) for a more extensive derivation of these relations.

The sphericity $s = c/a$ and the oblateness $p = b/a$ can be related directly to the eigenvalues of the tidal tensor $\lambda_1 > \lambda_2 > \lambda_3$:

$$\lambda_1(p, s) = \frac{1 + (\delta_v - 2)s^2 + p^2}{p^2 + s^2 + 1} \quad (1.30)$$

$$\lambda_2(p, s) = \frac{1 + (\delta_v - 2)p^2 + s^2}{p^2 + s^2 + 1}, \quad (1.31)$$

where $\delta_v = \sum_{i=1}^3 \lambda_i$.

Park and Lee (2007) then go on to derive the dependence of the ellipticity distribution of voids on the cosmological model. The probability density distribution \mathcal{P} for the

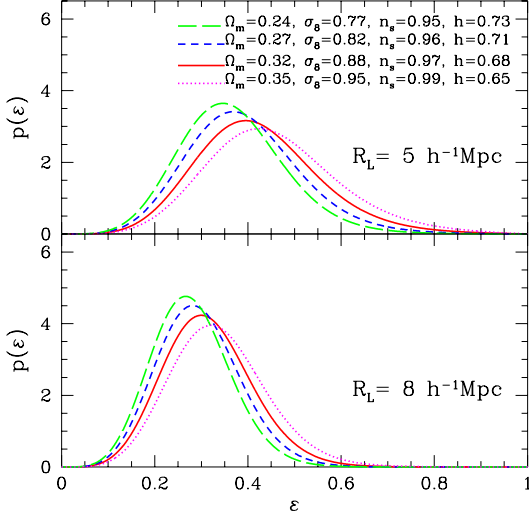


Figure 1.7: “Probability density distributions of the void ellipticity predicted by our analytic model for the four different sets of cosmological parameters at two different smoothing scales: $R_L = 5$ and $8h^1\text{Mpc}$ in the upper and the lower panel, respectively. For each case, the void density contrast is set at $\delta_v = 0.9$.” Image from Park and Lee (2007).

sphericity $s = 1 - \epsilon$ they derive is as follows;

$$\begin{aligned}
 \mathcal{P}(1 - \epsilon; z) &= \mathcal{P}(s; z, R_L) = \int_s^1 \mathcal{P}[p, s | \delta = \delta_v; \sigma(z, R_L)] dp \\
 &= \int_s^1 dp \frac{3375\sqrt{2}}{\sqrt{10\pi}\sigma^5(z, R_L)} \exp\left[\frac{-5\delta_v^2 + 15\delta_v(\lambda_1 + \lambda_2)}{2\sigma^2(z, R_L)}\right] \\
 &\times \exp\left[-\frac{15(\lambda_1^2 + \lambda_1\lambda_2 + \lambda_2^2)}{2\sigma^2(z, R_L)}\right] (2\lambda_1 + \lambda_2 - \delta_v) \\
 &\times (\lambda_1 - \lambda_2)(\lambda_1 + 2\lambda_2 - \delta_v) \frac{4(\delta_v - 3)^2 ps}{(p^2 + v^2 + 1)^3}.
 \end{aligned} \tag{1.32}$$

They show that this distribution is sensitive to changes in the cosmological parameters (see figure 1.7). This dependence comes from the inclusion of $\sigma(z, R_L)$ which is the linear rms fluctuation of the matter density field smoothed on a scale of R_L (which is related to the void size in Lagrangian coordinates) at redshift z , defined as:

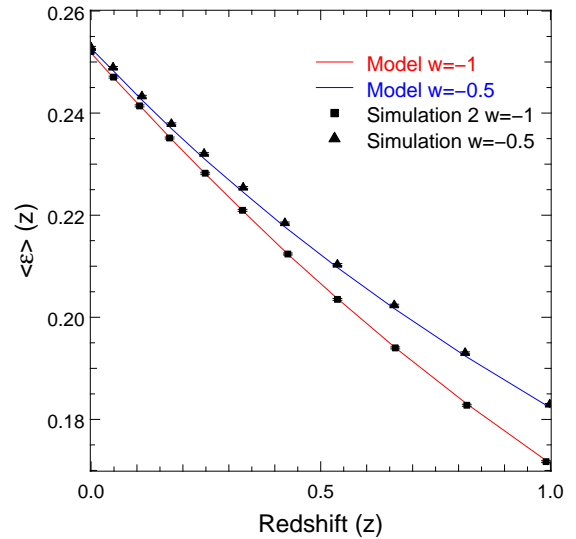
$$\sigma^2(z, R_L) \equiv D^2(z) \int_0^\infty \frac{k^2 dk}{2\pi^2} P(k) W^2(kR_L) d \ln k, \tag{1.33}$$

where $D(z)$ is the linear growth factor, $W(kR_L)$ is a top-hat window function and $P(k)$ is the linear power spectrum.

In general they claim that equation 1.32 implies that the mean ellipticity of voids decreases with redshift z . More importantly, they show that the model’s rate of ellipticity decrease is sensitive to changes in the cosmological parameters. According to this model, the redshift dependence of the mean ellipticity can be used to discriminate between different values of w_a (Lee and Park, 2009). Similar results were later found by Lavaux and Wandelt (2010). This is illustrated in figure 1.8, where a clear distinction can be made between the ellipticity evolution of the two models.

These results give the strong impression that voids are a promising probe of the nature of dark energy. One of the central tests of our project is to see whether indeed we can use this probe in our simulations.

Figure 1.8: Differences in the mean ellipticity evolution between models with $w = -1$ and $w = -0.5$. Both the results from theory (the red and blue lines) and the results from the corresponding N-body simulations (triangles and squares) are shown. Figure from Lavaux and Wandelt (2010).



1.3.3 Observing voids

One important aspect remains to be addressed. We want to probe the nature of dark energy using voids, but how does one observe the near empty regions of voids? Obviously this is a crucial question, one that many have tried to answer, but no single answer seems to be perfect. When redshift surveys were still small and manageable one could try analysing all the data. At the time this worked well (Kirshner et al., 1981). With the advent of wide and deep surveys (like the SDSS, see figure 1.9) we need to find more efficient ways of working through the data.

There are actually two questions that need to be asked. At the heart of the problem lies the simple fact that we cannot observe the voids itself. On the other hand, we can observe the galaxies in walls, filaments and clusters around the voids. The first question then is: how do we establish the locations, shapes and sizes of voids from a sample of galactic observations like in figure 1.9?

This question is answered by a large and diverse number of void finding algorithms that have been developed over the past decade. To give the reader a taste, we describe three basic classes of these algorithms. Each class has a number of implementations that may differ in details. For a complete overview of these algorithms see Colberg et al. (2008) and Lavaux and Wandelt (2010). The basic three classes of void finders are the following:

- Void finders that identify regions free of any galaxies. Most of these algorithms do this by trying to find the largest empty spheres in the galaxy distribution. Examples are found in Hoyle and Vogeley (2002); Müller et al. (2000) and Foster and Nelson (2009).
- Other void finders try to identify geometrical structures in the dark matter density field. The Watershed Void Finder by Platen et al. (2007), which we used in this thesis, is an example of this class. The main difference between these voids and those in the above class is that they allow for a more flexible treatment of the shape of voids. Other examples include ZOBOV (Neyrinck, 2008) and the void finders in Plionis and Basilakos (2002); Colberg et al. (2005) and Shandarin et al. (2006).

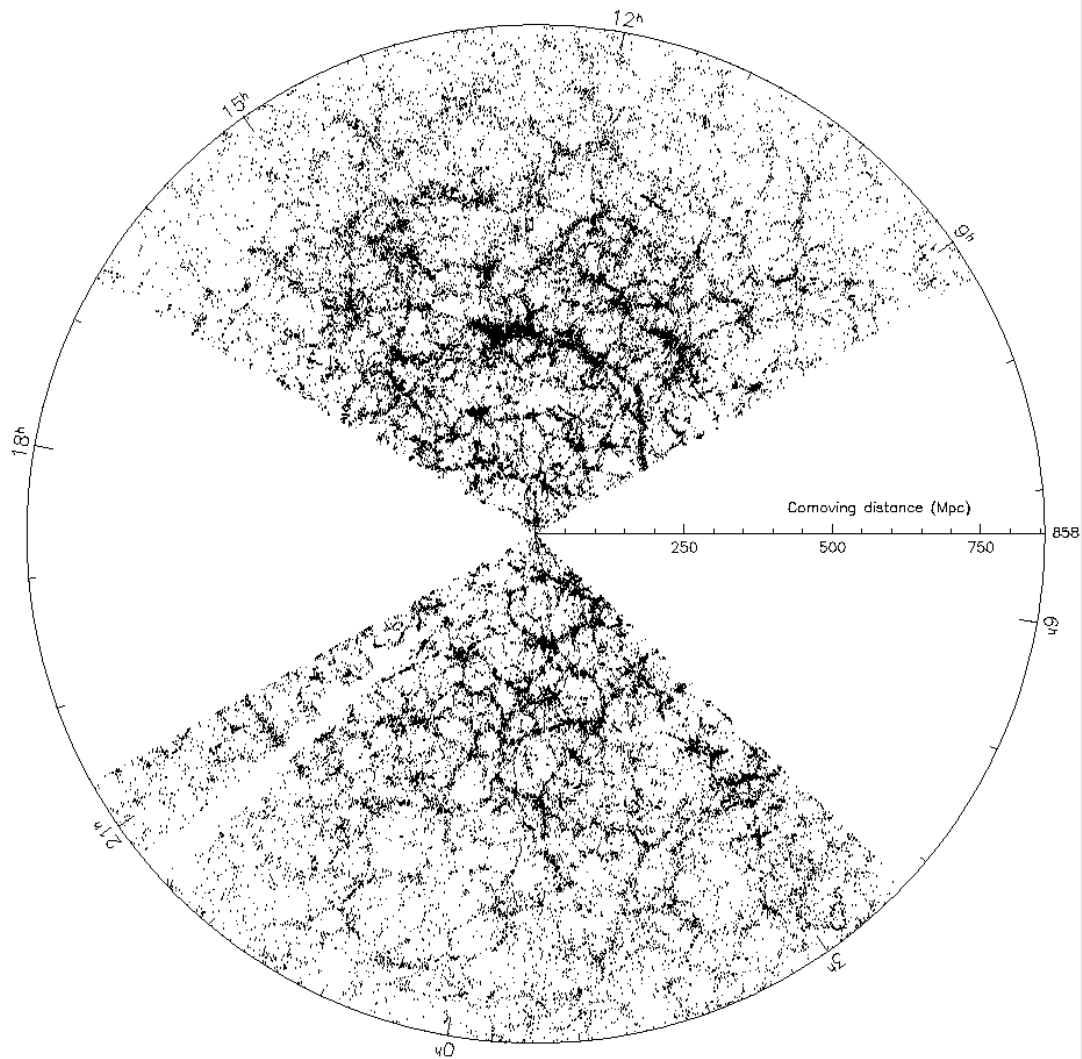


Figure 1.9: Slice out of the galaxy distribution of the Sloan Digital Sky Survey. The pattern of the cosmic web is clearly visible. High density regions (walls and filaments of galaxies) surround the relatively empty regions that we call voids.

- The third class of void finders incorporates dynamical aspects by checking for gravitationally unstable points in the dark matter distribution. Examples of these include the finders by Hahn et al. (2007) and Lavaux and Wandelt (2010).

Most of these algorithms are compared in Colberg et al. (2008). They find that the shapes and sizes of voids from different finders can differ significantly (see figure 1.10). It is thus of vital importance to make the right choice of void finder for the task at hand. We will use the Watershed Void Finder (more on this in section 3.2).

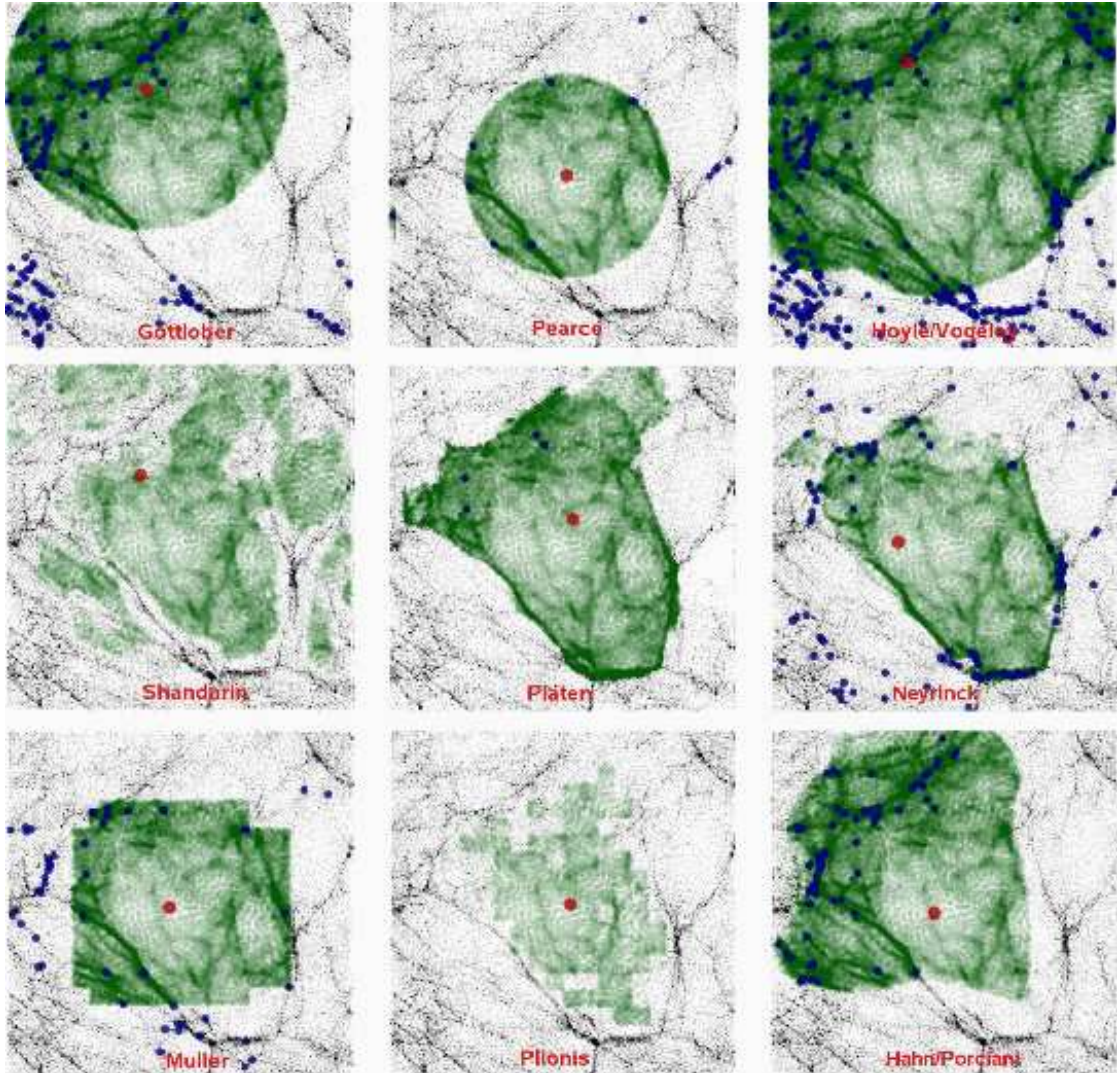


Figure 1.10: “A compilation of void finders. The 9 frames illustrate the performance of different void finders with respect to a central voids in the milli-Millennium simulation. The N-body dark matter particles are depicted as black points. The blue dots locate (semi-analytically modelled) galaxies within the central void region. For each void finder, the identified void region is coloured green with the void centre marked by a red point.” Image from Colberg et al. (2008), text from van de Weygaert et al. (2009).

The second problem with observing voids that needs to be addressed is that of redshift distortions. Being the only distance estimator for the bulk of our data, the redshift is

a major complication, but also a vital asset, to many of our analyses⁷. Because of its dependence on the velocity in the radial direction, a large scatter is introduced into our distance coordinate.

For voids this has serious implications that need to be taken into account. Because of the outflow of matter from voids, we will mainly see galaxies moving out of the voids. This means that the galaxies at the front and back of the void (i.e. the sides closest to and farthest from us) will have redshifts that make the void seem larger. At the side closest to us, the galaxies will move towards us with respect to the Hubble flow, thus seeming less far as approximated through the redshift. Those galaxies at the farthest side will move away from us even faster. Voids will in effect seem stretched out in the line of sight. In fact, this was proposed by Ryden and Melott (1996) as a way to use voids to infer cosmological information. Recent studies confirm this idea (Percival and White, 2009; Jennings et al., 2010).

In effect, voids will seem larger than they truly are. We should not expect the shape distribution of voids to change. Because the voids are randomly oriented towards us, there will be cases in which the void seems stretched along its major axis and so seem more elliptical. There will be an equal amount of cases in which the void seems stretched along a minor axis which will make it seem less elliptical. On average there should then be little effect on the shape distribution. This is confirmed by Hoyle and Vogeley (2002). Some other redshift distortion effects, like the “fingers of god”, may cause noise that could pose a problem.

⁷In that it is not unlike alcohol; “the cause of, and solution to, all of life’s problems,” H.J. Simpson.

Our analysis is based on numerical N-body simulations of dark matter (DM) particles in several cosmological backgrounds, most of which include evolving dark energy. In this section we outline the basics of producing such simulations with the `GADGET-3` code. We describe the actual datasets used in our analysis and we elaborate on the necessary preprocessing.

2.1 Producing simulations with GADGET

For our numerical experiments we have used a version of the `GADGET` N-body simulation code (Springel, 2005). It uses a combination of hierarchical tree and particle-mesh algorithms for calculating respectively the short and long range gravitational forces. Particle-mesh methods are the fastest schemes for computing the gravitational field, but on the scale of one or two mesh cells it is inaccurate, leading to errors for high density regions (Springel, 2005). Tree algorithms are slower in most cases, but are scale invariant and therefore solve the high-resolution problem at small scales. In `GADGET-2`, tree-forces are used for (sub-)mesh cell scales. These are summed with the particle-mesh forces that are truncated at small scales using an exponential factor:

$$\phi_k = \phi_k^{\text{short}} + \phi_k^{\text{long}} \quad (2.1)$$

$$\phi_k^{\text{long}} = \phi_k \exp(-k^2 r_s^2) \quad (2.2)$$

$$\phi_k^{\text{short}} = \phi_k (1 - \exp(-k^2 r_s^2)), \quad (2.3)$$

where the ϕ_k 's are the Fourier transforms of the gravitational potentials and r_s is the spatial scale of the split between long and short range forces. In practice, a certain radius is chosen at which the short scale (tree) force is not calculated anymore to limit computational costs. Because of the exponential drop-off with high k (low spatial scales), the contribution of the short scale potential to the force drops to about 1% at $r \approx 4.5r_s$. The total force on a particle is thus more accurate than when using a particle-mesh only. This is at the expense of some extra computational costs for building and walking the tree up to a certain radius. For a more detailed description of these algorithms read Springel (2005), Xu (1995) and Bagla and Ray (2003).

GADGET uses smoothed particle hydrodynamics (SPH) for approximating hydrodynamical behaviour. This means that it treats particles as smoothed spheres with a certain radius. Effectively, this causes viscosity when particles start overlapping. As we have only used non-collisional DM-particles in our simulations, we have made no use of the SPH functionality of the code.

The version of the **GADGET** code that we used (**P-GADGET-3**) still uses the above techniques, but adds one feature crucial to our research: the ability to specify the mode of evolution of dark energy. This is done through an extended dark energy implementation, described in Dolag et al. (2004). In the comoving coordinate space simulation of **GADGET** the only thing that needs to be altered for evolving dark energy models to be properly included is the Hubble parameter, which must be written in its full expansion factor dependent form (the square root of equation 1.12):

$$H(a) = H_0 \sqrt{\frac{\Omega_m}{a^3} + \frac{1 - \Omega_m - \Omega_\phi}{a^2} + \Omega_\phi \exp\left(-3 \int_a^1 \frac{1 + w(a')}{a'} da'\right)}. \quad (2.4)$$

The extended **GADGET-3** implementation expects the integral over a' to be tabulated in advance so it can be read in during the simulations.

2.2 Dark matter particles

The basic data for our analyses are the several cosmological simulation boxes with periodic boundary conditions, containing DM particles only. The initial conditions were set up by displacing particles from a regular N by N by N grid to their positions at $z = 60.0$ using the Zel'dovich approximation of the linear phase of structure formation (Zel'Dovich, 1970). The approximated particle positions \vec{x} and velocities \vec{v} are:

$$\vec{x}(\vec{q}) = \vec{q} + D(z)\vec{\psi}(\vec{q}) \quad (2.5)$$

$$\vec{v}(\vec{q}) = aD(z)Hf(\Omega)\vec{\psi}(\vec{q}), \quad (2.6)$$

where \vec{q} is the initial (grid) particle position, $D(z)$ is the linear perturbation growth factor, $f(\Omega)$ is the dimensionless linear velocity growth factor and $\vec{\psi}$ is the displacement field that is derived from the initial random Gaussian potential $\phi(x)$. $D(z)$ and $f(\Omega)$ are given as:

$$D(z) = \frac{5\Omega_{m,0}H_0^2}{2}H(z) \int_z^\infty \frac{1+z'}{H^3(z')} dz' \quad (2.7)$$

$$f(\Omega) \equiv \frac{a}{D} \frac{dD}{da}. \quad (2.8)$$

We have used low and high resolution datasets, both for separate purposes. Both datasets are snapshots of **P-GADGET-3** simulations of DM particles in universes with different modes of dark energy. We further describe these two sets below.

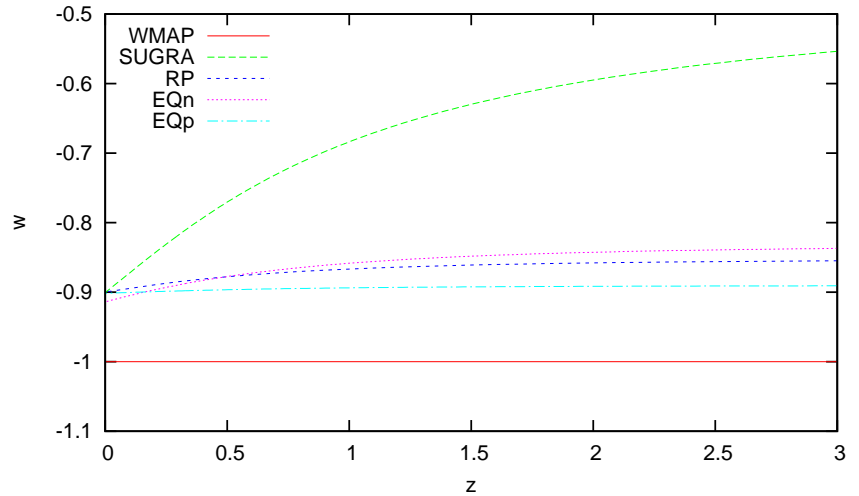


Figure 2.1:
Evolution of the equation of state parameter $w = P/\rho$ of dark energy for different models.

2.2.1 High resolution

Quantitative description

The high resolution particle boxes used for this project were kindly provided by Klaus Dolag and Volker Springel¹. This set consists of five cosmological N-body simulations of 768^3 dark matter particles in which different models of dark energy were used on the same initial conditions. The models are described in section 1.2.2.

The general cosmological parameters adopted for the simulations are the WMAP 3-year data values: $\Omega_m = 0.268$, $\Omega_\Lambda = 0.732$, $\Omega_b = 0.044$, $h = 0.704$, $\sigma_8 = 0.776$ and $n = 0.947$.²

<i>Model</i>	α	w_{JBD}	w_0	w_a	σ_8
WMAP3 (Λ CDM)	–	–	–1.0	0.0	0.776
RP	0.635	–	–0.9	0.0564	0.746
SUGRA	0.635	–	–0.9	0.452	0.686
EQp	0.635	120	–0.9	0.0117	0.794
EQn	–0.229	–120	–0.9	0.0805	0.729

Table 2.1: Dark energy model parameters used in the simulations. For a description of the models see section 1.2.2. σ_8 is normalized at the CMB (see text). w_a is determined using a χ^2 fit (see section 1.2.3).

The specific DE model parameters are summarized in table 2.1. The physical linear size of a box is $300h^{-1}\text{Mpc}$ and the particles have masses of $0.443 \times 10^{10}h^{-1}M_\odot$. These parameters are consistent with current observational constraints (Acquaviva et al., 2005; Amanullah et al., 2010; Komatsu et al., 2010). The tables of $w(a)$, needed for the extended DE implementation, were calculated for the different models by Klaus Dolag

¹Respectively of the Max-Planck-Institut für Astrophysik, Garching and Zentrum für Astronomie der Universität Heidelberg.

²Respectively the density of matter, the density of Dark Energy, the density of baryonic matter, the hubble parameter ($h = H_0/100$), the normalization parameter of the power spectrum with a top-hat filter radius of $8h^{-1}\text{Mpc}$ and the index of the primordial power spectrum.

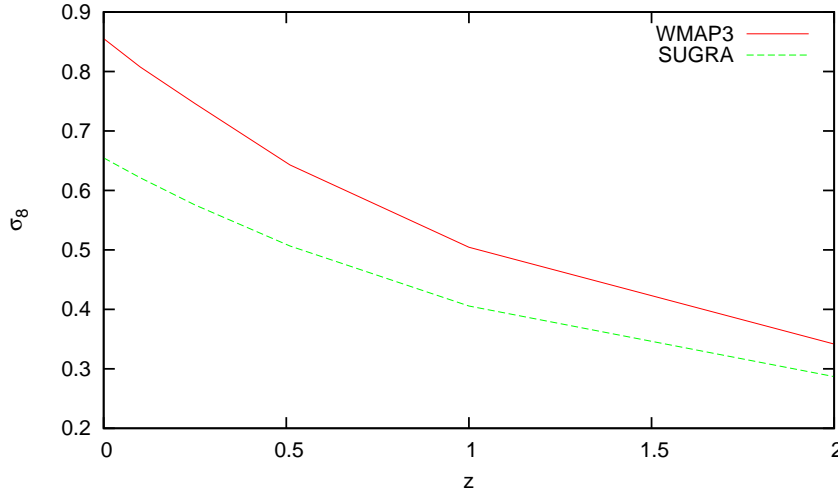


Figure 2.2:
Evolution of structure as measured through σ_8 for the WMAP3 and SUGRA models.

(see figure 2.1). For the WMAP3 model we have snapshots at $z = 0.1$, $z = 0.25$, $z = 0.51$, $z = 1.00$ and $z = 2.04$, while for the other models we only have a snapshot at $z = 0$.

The DE models were normalized at the CMB using the relation

$$\sigma_{8,DE} = \sigma_8 \frac{D_{\Lambda\text{CDM}}(z_{\text{CMB}})}{D_{\text{DE}}(z_{\text{CMB}})}, \quad (2.9)$$

where we assume $z_{\text{CMB}} = 1089$ and D is the linear growth factor, which is dependent on the DE model through H (equation 2.7). This rescaling will cause differences in the amount of clustering, characterized by the normalization parameter σ_8 . σ_8 probes the power spectrum at a scale of $8h^{-1}$ Mpc, whereas the CMB probes higher scales. In figure 2.2 we show the resulting values of σ_8 for two different models (taken from our own low resolution data, see below). It is clear that this will influence structure formation. In section 4.5 we will see that its impact is significant.

Qualitative description

In figure 2.3 we show DTFE density slices (see section 4.2 for a description of this density estimator) with a thickness of about $1h^{-1}$ Mpc, taken from the center of the boxes of the WMAP3 simulation at several redshifts. Generally, the evolution of structure from a more homogeneous state to a more pronounced cosmic web is clearly visible. We can, however, zoom in on two specific processes, and that is the evolution of the supercluster just below the center and the evolution of a void-region to the left of it; a zoomed in version of this part of the image is shown in figure 2.4.

In figure 2.4 on the right of the panels we see the evolution of what we may call a supercluster. What begins at $z = 2$ as a slightly overpronounced web of filaments, already containing small separate groups or clusters, quickly transforms into one elongated massive structure with a length of about $40h^{-1}$ Mpc. In the center we see a massive cluster evolving as a merger of the smaller clusters and groups at lower redshifts. The hierarchical clustering paradigm is thus nicely illustrated.

On the other hand we have the left hand side of the panels where we can see the evolution of several voids (black regions in the upper panels, dark blueish in the lower ones). We roughly define these as regions with relative densities of $\rho/\rho_0 < 0.2$ (van de Weygaert and van Kampen, 1993; van de Weygaert and Platen, 2009). Overall we see

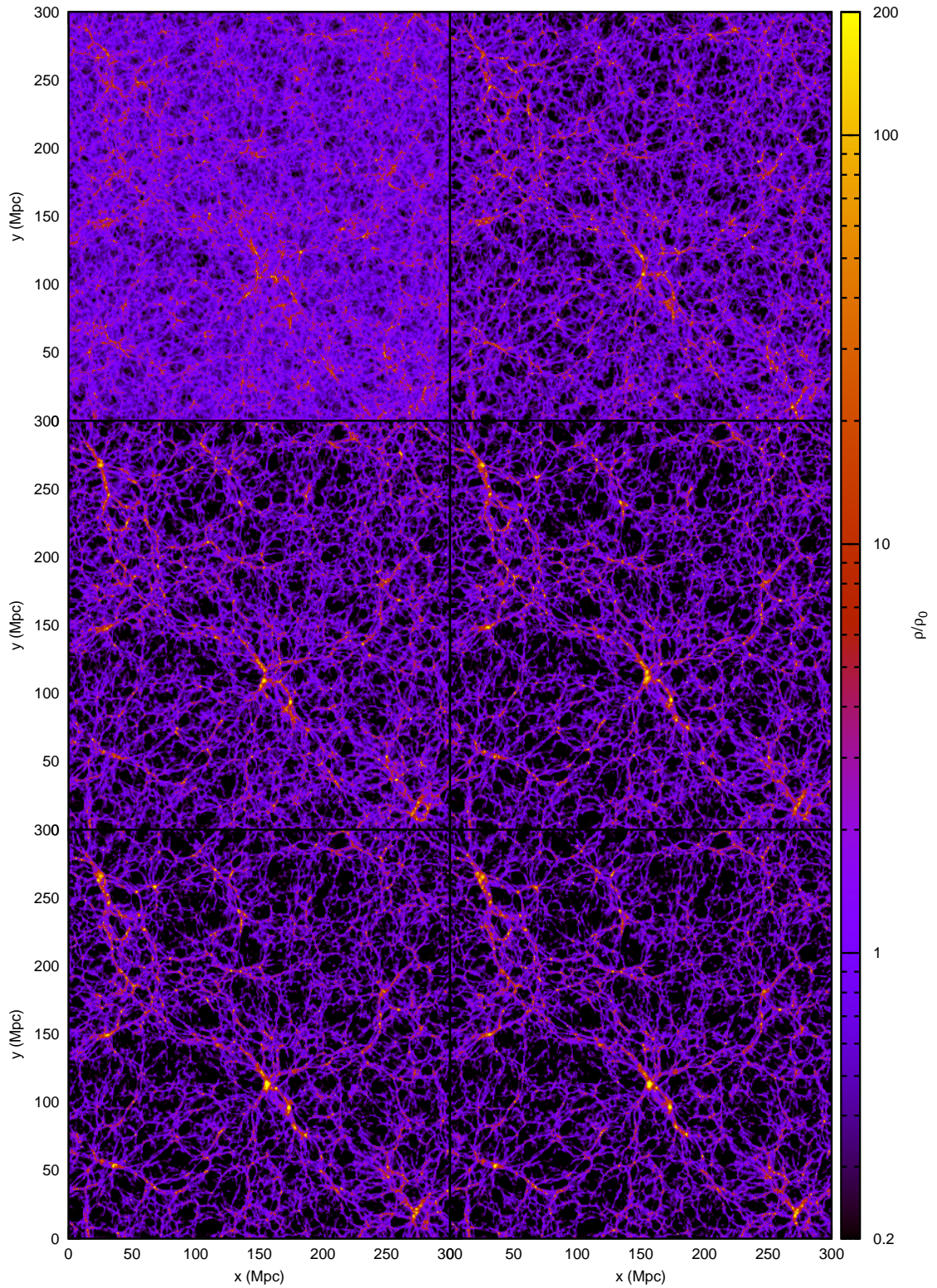


Figure 2.3: Density slices of the simulation boxes of the WMAP3 model at different redshifts. Downwards and from left to right: $z = 2.04$, $z = 1.00$, $z = 0.51$, $z = 0.25$, $z = 0.1$ and $z = 0$. The colors have been chosen such that clusters are yellow ($\rho/\rho_0 \gtrsim 200$) and voids are black ($\rho/\rho_0 \lesssim 0.2$).

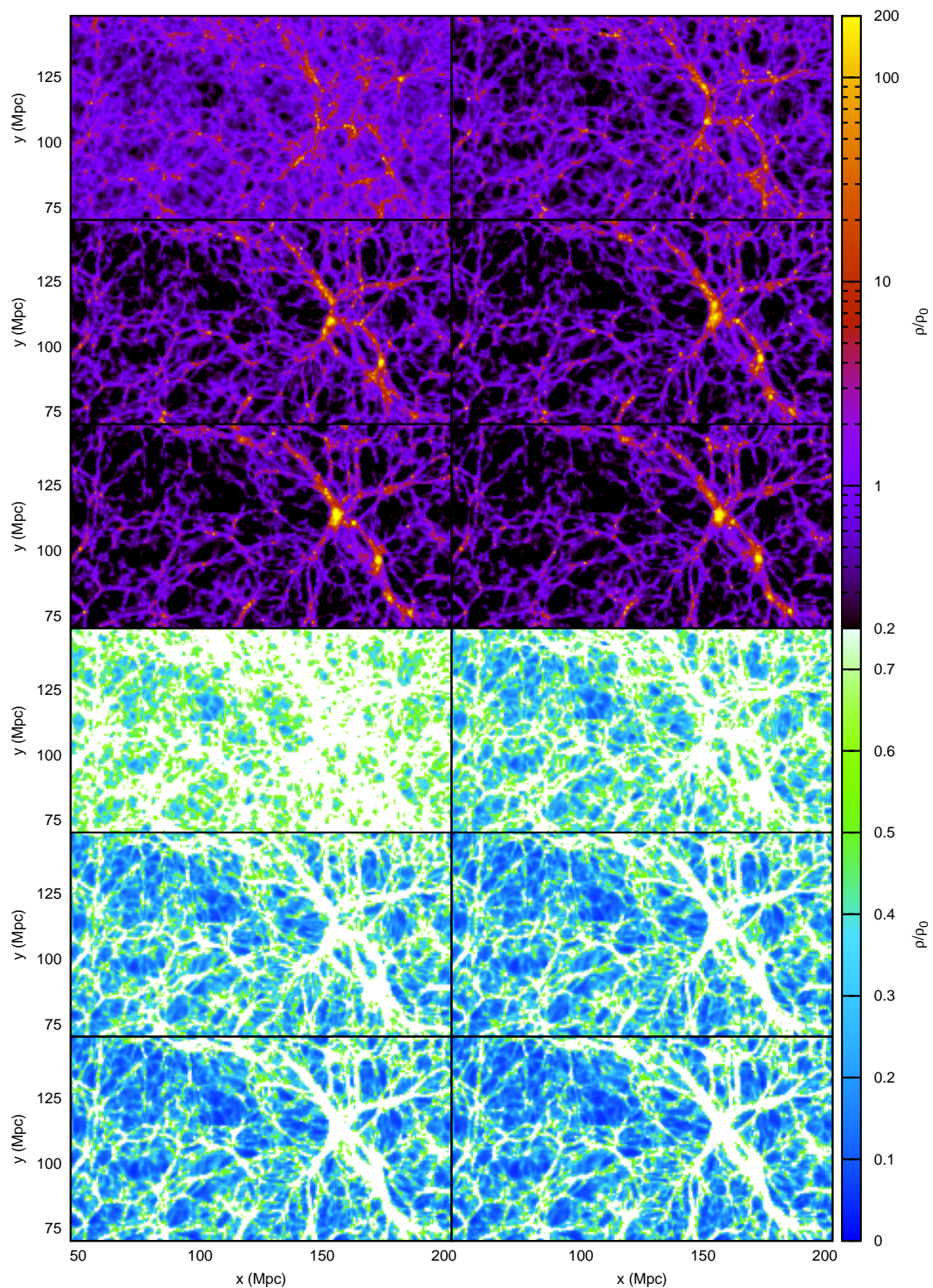


Figure 2.4: A zoom-in of the images in figure 2.3. The colors have been chosen such that clusters are yellow ($\rho/\rho_0 \gtrsim 200$) and voids are black ($\rho/\rho_0 \lesssim 0.2$).

that most of the evolution of voids takes place between redshifts 2 and 0.5. This is fortunate given our goal of probing dark energy, because as Huterer and Turner (2001) showed the redshift range $0.2 \lesssim z \lesssim 2$ is the most promising for probing $w(z)$. The voids quickly grow from initial seeds with radii of about $1h^{-1}$ Mpc, to voids ranging in size from 2 to $30h^{-1}$ Mpc. We also see that in this process the number of voids actually decreases due to voids merging. At the later timesteps we can still discern a lot of substructure in voids that is caused by this process. Especially when we take a look at the bottom panels we can still clearly discern walls in the larger voids that survived the merging process that took place billions of years before (Sheth and van de Weygaert, 2004).

We can compare these modes of evolution to those in different cosmological models. We show in figure 2.5 two density slices at $z = 0$ of the WMAP3 and SUGRA simulations. There are some clear differences between these simulations. The size and depth of voids are smaller in the SUGRA case. Filaments are still more diffuse and clusters are less pronounced and clumpier. As seen from hierarchical clustering theory, they are less evolved than in the WMAP3 model.

The evolution of the equation of state parameter hence seems to have a significant impact on structure formation: a higher value of w (i.e. closer to zero, as it is negative) slows down structure formation. This makes sense when we remember from above that the evolution of voids takes place around $z = 1$, and at this time $w(z)$ differs a lot for the two models (see figure 2.1); from a difference of 0.2 at $z = 0.5$ to a difference of 0.4 at $z = 2$. From the σ_8 measurements in figure 2.2 we expected this as well.

In chapter 4 we try to quantify these structural differences.

As can be seen in figure 2.1, the other DE models differ less dramatically from the WMAP3 model. We can clearly see in figure 2.6 that this leads to a larger degree of similarity in the shapes and sizes of the structures present in the simulations.

More information on these data can be found in Dolag et al. (2010, in preparation).

2.2.2 Low resolution

For testing purposes we ran a few additional simulations of 256^3 DM particles. The physical parameters used for the initial conditions of these sets are exactly the same as those of the high resolution simulations. We used these simulations to investigate the influence of mass resolution on the statistics used in our analyses and to rule out possible effects of cosmic variance by using several randomly generated initial conditions.

2.3 Redshift space

The GADGET particle boxes contain velocities and positions of all particles, which enables us to calculate the redshift of particles as seen from a certain position. Using the original x, y, z coordinates and the redshifts we transform the particles to what we will call *redshift space*. This transformation is done as follows.

First, we place the observer at some point in the box. Because of the boxes' periodicity, we can then wrap around the particles that are further out than half the boxsize in one of the x, y, z directions. This will place the observer in the center of the box (this latter step can be omitted at the cost of the aesthetics of symmetry).

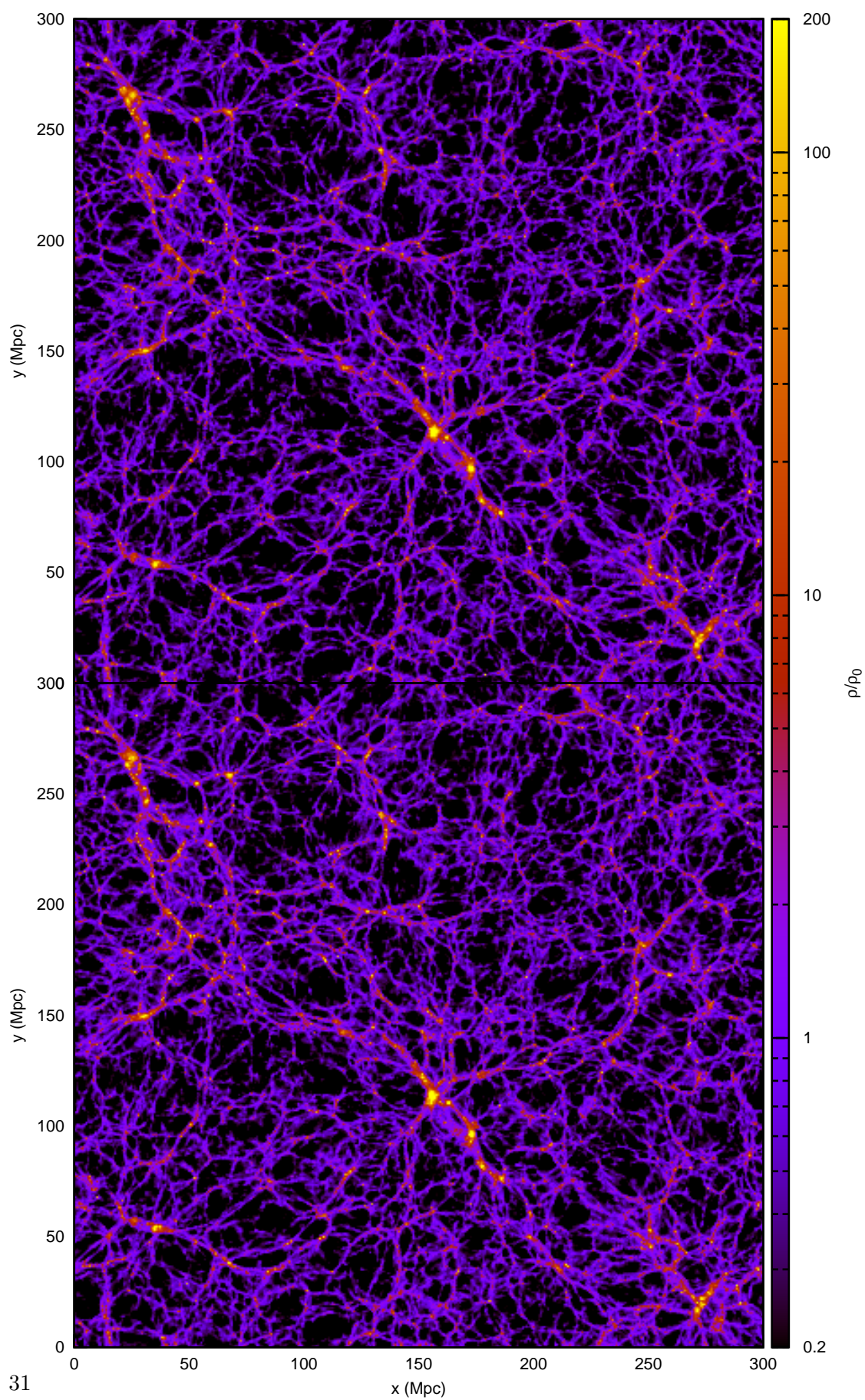


Figure 2.5: Density slices of the simulation boxes of the WMAP3 (top) and SUGRA (bottom) models at $z = 0$.

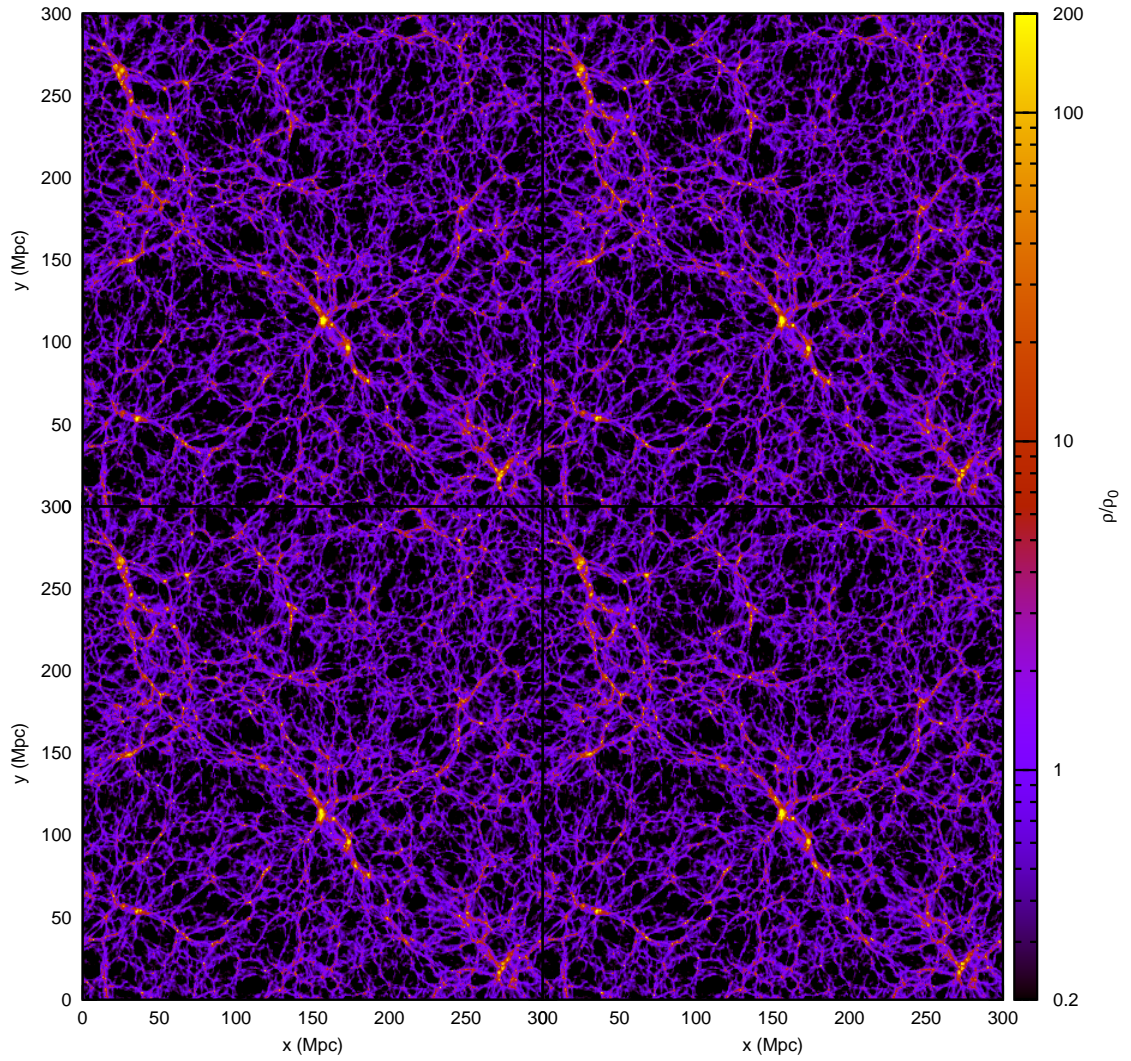


Figure 2.6: Density slices of the simulation boxes of the WMAP3 (top left), RP (top right), EQn (bottom left) and EQp (bottom right) models at $z = 0$.

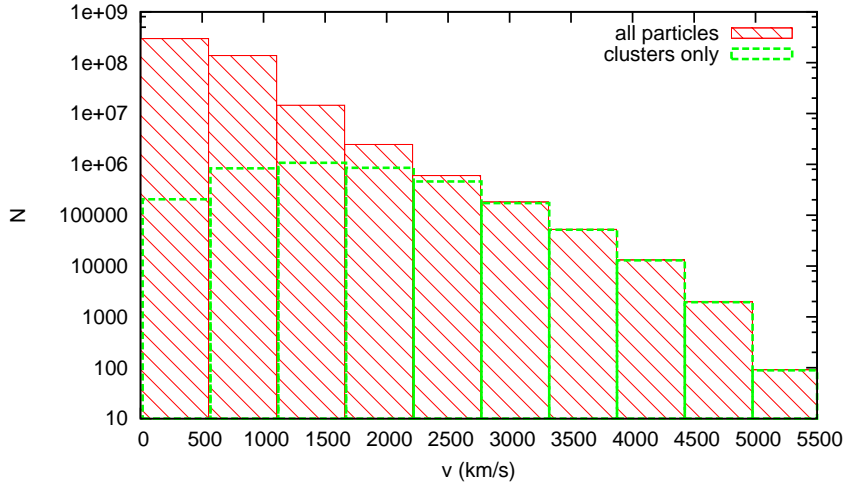


Figure 2.7: Velocity distributions. In red the distribution of all particles in the WMAP3 simulation, in green that of only the clusters, loosely defined as overdensities of $\delta > 200$.

Next, we transform to spherical coordinates r, θ, ϕ and calculate the radial component of the velocity

$$v_r = \vec{v}_{\text{pec}} \cdot \hat{r} \quad (2.10)$$

for each particle. We use these to calculate the redshift as seen by the observer in the center of the box:

$$z = z_r + z_{\text{cos}} = \sqrt{\frac{1 + v_r/c}{1 - v_r/c}} - 1 + \frac{rH}{c} \approx \frac{v_r}{c} + \frac{rH}{c}, \quad (2.11)$$

where z_r is the Doppler redshift caused by the particle's radial peculiar velocity v_r and z_{cos} is the cosmological redshift due to expansion of the universe. The approximation is valid when $v_r \ll c$. We have thus obtained two spatial coordinates and a redshift, all of which can actually be measured in observations. The redshift can be transformed back to a radial distance in redshift space, i.e. an approximation of the distance that will contain an intrinsic error due to particle velocities in the line of sight:

$$r_{z\text{-space}} = zc/H. \quad (2.12)$$

The results of this transformation for the WMAP3 and SUGRA boxes are shown in figure 2.8. Large clusters in real space are transformed into the well known *fingers of god*, whereas voids seem a bit larger and emptier in redshift space. The “fingers” seem rather dramatic, but the effect is readily explained by figure 2.7. The high velocity end of the distribution is completely due to the high velocities in clusters³. These high velocity dispersions cause the redshift distortions we see in the figure. Differences between the two models are similar to those in real space, with the added difference in the fingers, i.e. the clusters, which in the SUGRA box are shorter, meaning that their internal velocity dispersions are lower. This is likely due to their lower masses, caused by slower evolution.

³For this plot we used a very simple, but effective definition of clusters as overdensities of $\delta > 200$.

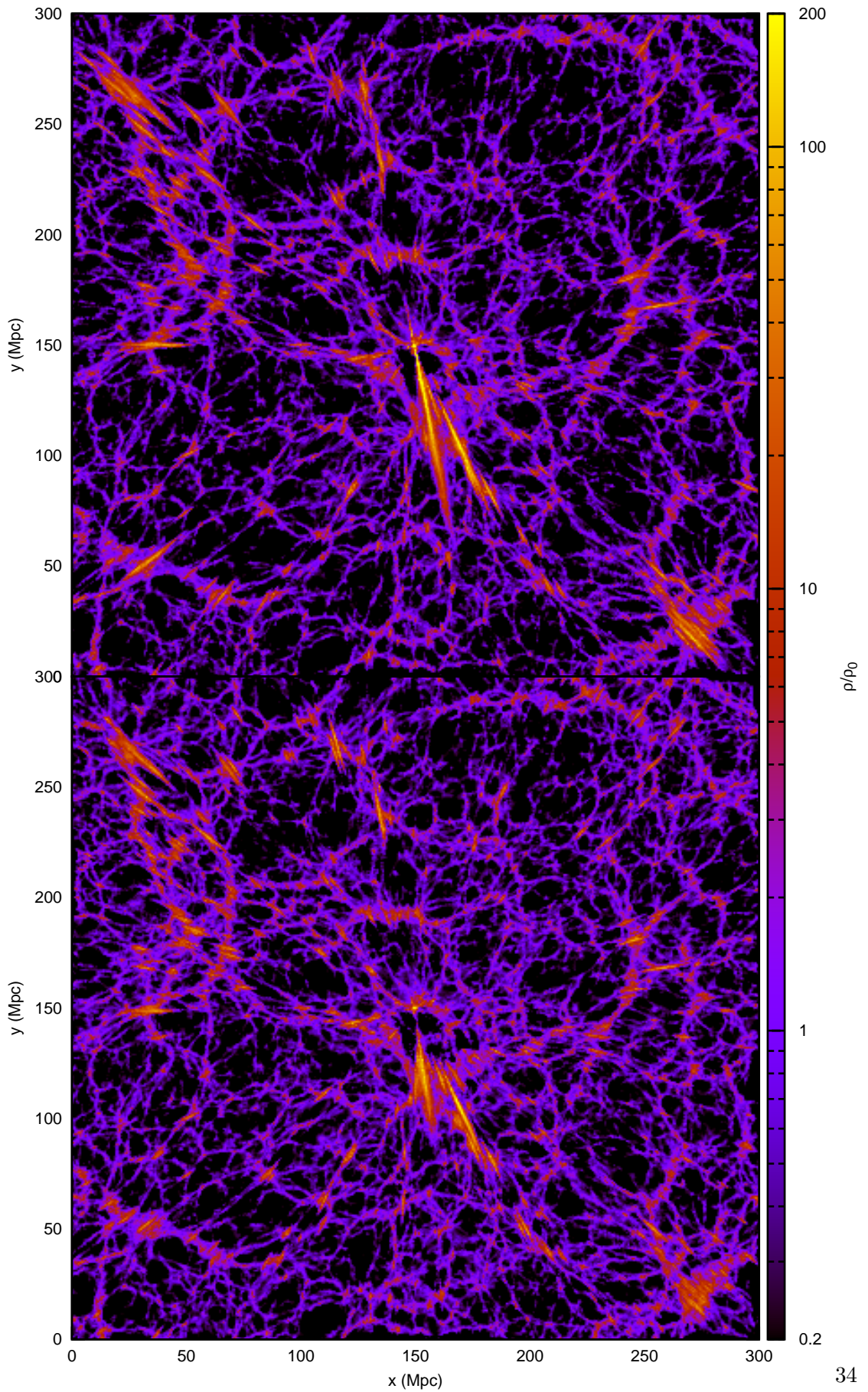


Figure 2.8: Redshift space density slices of the simulation boxes of the WMAP3 and SUGRA models at $z = 0$.

N-body simulations produce at least $6N$ data points (positions and velocities). Redshift surveys of N galaxies contain at least $3N$ data points (right ascension, declination and redshift), not to mention the information in spectra. Our simulations contain about half a billion individual particles. The reduction of these data to insightful quantitative measures thus poses a great challenge. We need intelligent algorithms to reduce this information to an amount we can deal with.

For this we use algorithms that identify the underlying large scale structures present in the particle distributions. In section 1.3 we briefly touched upon the concept of void finders. Our research concerns the shapes and sizes of voids, making this tool invaluable. We will elaborate on it below. Before that, we focus on halo finders which allow us to make predictions on the feasibility of our methods in real galaxy surveys.

3.1 Haloes

For every simulation box at all redshifts the `SUBFIND` algorithm of Springel et al. (2001) was used to find the gravitationally bound haloes (groups of adjacent particles, representing concentrated clumps of dark matter) that can colloquially be identified as galaxy haloes. `SUBFIND` first defines a catalogue of halo-like structures using a Friends-of-Friends (FoF) algorithm. `SUBFIND` then searches the resulting FoF particle groups for self-bound substructures. This two-stage process has the advantage that a structural hierarchy is automatically created, with the FoF-groups in some cases containing on the order of 100 bound “subhaloes”. It is these subhaloes that we are interested in; the FoF-groups are generally too large and structurally incoherent, whereas the subhaloes have sizes and masses comparable to those of galaxy haloes. In the remainder of this text we will therefore define “haloes” as these `SUBFIND` subhaloes.

A nice overview of halo finders and properties in N-body simulations can be found in Aragón Calvo (2007). Below we describe in more detail these two algorithms used for finding the haloes and the resulting halo catalogues used in our analysis.

3.1.1 Friends-of-Friends group finder

First used in Press and Davis (1982) and Davis et al. (1985), the Friends-of-Friends (FoF) group finding algorithm is a simple but effective way of discerning structure in particle distributions. It groups particles together when their distance is less than a certain fraction b of the mean interparticle distance. The resulting set of groups thus depends on b only; the algorithm makes no further assumptions about shapes or sizes of groups. For relatively large b (≈ 0.5), groups tend to be somewhat oversized and structurally ill defined, while for $b \lesssim 0.25$ FoF-groups are more centrally concentrated and regularly shaped.

As we are interested in finding haloes, which we roughly define as concentrated clumps of dark matter, we follow Springel et al. (2001) in using $b = 0.2$ to determine FoF-groups which we use as input for the SUBFIND halo finder. Only groups with at least 10 particles are included in the group catalogue. In figure 3.1 we show the distribution of the centers of these groups overlaid on the density field. Clearly the groups trace the general structures present in the field; clusters, filaments and walls are all covered, whereas voids remain largely empty. It must be noted though that a lot of substructure is lost in the group distribution and will thus be lost in the halo distribution as well.

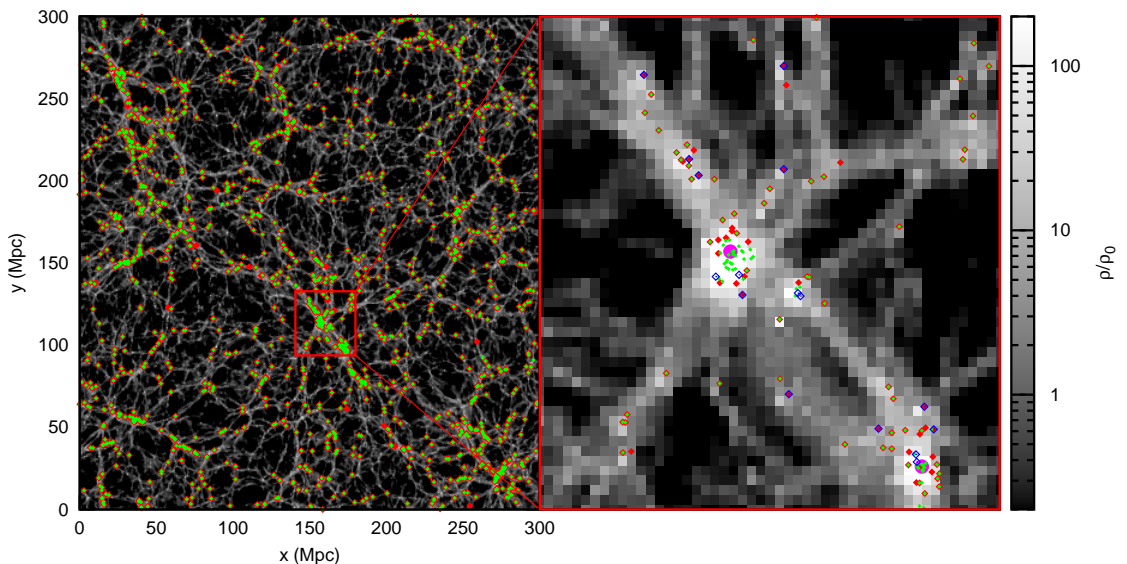
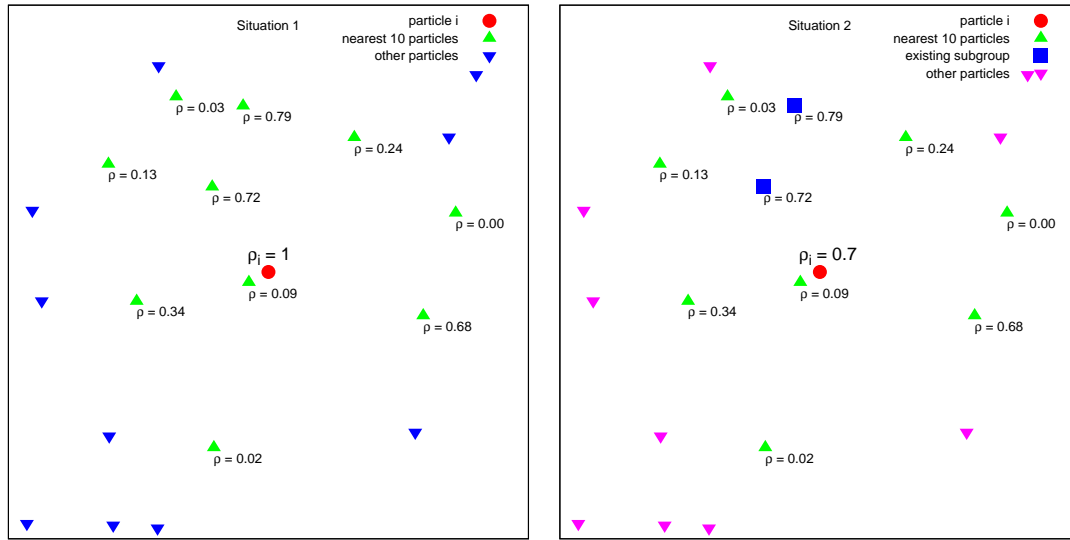


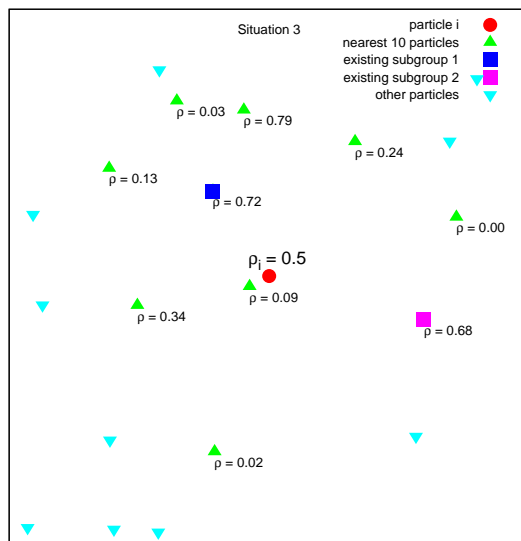
Figure 3.1: In the left panel we show the distribution of haloes (green) and FoF-groups (red) in the same slice as in figures 2.3 through 2.8. In the right zoom-in panel we additionally split the haloes by mass; green dots have $M < 10^{12} M_{\odot}$, blue open diamonds have $10^{12} M_{\odot} < M < 10^{13} M_{\odot}$ and the two magenta filled circles are even more massive; the left one has a mass of $2.4 \cdot 10^{13} M_{\odot}$, the lower right one has $3.1 \cdot 10^{14} M_{\odot}$.

3.1.2 SUBFIND halo finder

The SUBFIND algorithm by Springel et al. (2001) was mainly developed to identify substructure in the FoF-groups. It uses the physical criterion of gravitational boundedness to filter out some FoF-groups entirely and to find the subhaloes that make up the large clusters and which are assumed to be the sites where galaxies form (Springel et al., 2001).



(a) Particle i will start a new (sub)group, because there are no particles with $\rho > \rho_i$ amongst the 10 nearest neighbours. (b) Particle i will join the group of the two particles that have already formed a group.



(c) Particle i is a 'saddlepoint'. The two subgroups and particle i will form a new (sub)group.

Figure 3.2: The three situations the SUBFIND halo finder can encounter in its determination of (sub)groups. See text for further explanation.

The algorithm first approximates the density field and assigns a density to each particle. It then orders all particles by density and starts the algorithm with the highest density particle; call the particle under consideration i . We search its neighbourhood for the N_{ngb} nearest particles, which is a free parameter; $N_{\text{ngb}} = 10$ in Springel et al. (2001). We then determine the subset of these N_{ngb} particles that has $\rho > \rho_i$ (obviously for the first particle this means that the subset is empty) and of this subset we select the two closest to i . We distinguish three possible situations (illustrated in figure 3.1.2):

1. There are no particles with $\rho > \rho_i$. Then i is a local maximum and we start growing a (sub)group around it.
2. The subset consists of one or two particles that are already in a (sub)group. In this case particle i joins them.
3. We get two particles in different subgroups. We then call particle i a ‘saddlepoint of the density field’ and the two subgroups will be marked as ‘subhalo candidates’. At the end of the algorithm these candidates will be checked for self-boundedness. Particle i will be added to the two subgroups, which together will form a new (sub)group.

After all particles have been processed in this way we have produced a subhalo candidate list. Before checking for boundedness, we need to take care of the fact that some particles can be part of multiple subhalo candidates. This may occur when the new subgroup of the above third situation again merges with another subgroup. This is accomplished by simply checking for boundedness in order of decreasing subgroup size, i.e. in the reverse order in which the subhalo candidates have been found. The subhalo identifier is overwritten after every boundedness check, so the particles will only carry the identifier of the last subhalo it belongs to, which is the smallest one. Thus the algorithm identifies the smallest possible subhaloes. After these have been taken out, the larger haloes need another test of self-boundedness, because the deletion of the particles from the small subhaloes usually causes a portion of the remaining particles to become unbound. After this we then have a complete set of all the smallest possible, gravitationally bound haloes in the dataset.

3.1.3 Halo data

For our void shape analysis we were provided with halo catalogues of all the DE simulations at redshifts of $z = 0$, $z = 0.1$, $z = 0.25$, $z = 0.51$, $z = 1.00$, $z = 2.04$, $z = 2.98$ and $z = 3.80$ (at higher redshifts of $z = 5.20$ and $z = 8.43$ the halo finder finds significantly less haloes than at lower redshifts, thus making these halo sets unsuitable for comparison with the low redshift haloes). The halo data include positions, velocities and masses, as well as a host of other parameters we will not use. The halo position is simply defined as the mean position of its particles:

$$x = \frac{1}{N} \sum_i^N x_i, \quad (3.1)$$

where x_i are the particle positions of the halo and N is the number of particles in the halo. The velocity is calculated analogously. Halo mass is simply the sum of the particle masses.

We plot halo positions in figure 3.1. We see in the left panel that indeed some FoF-groups end up without a corresponding self-bound halo (the red dots without a green one on top). In the right panel a zoom-in of the massive cluster reveals that indeed large FoF-groups contain a lot of self-bound substructures. In fact this image clearly illustrates the need for a substructure finding algorithm; whereas the two largest haloes (the magenta circles) clearly reside in the cluster centers and may have shown up in real clusters as a cD galaxy, the FoF-groups of the cluster in the center of the image do not coincide with its central halo at all. They simply add up all the cluster matter into a few large, but fairly random groups, possibly discarding highly relevant substructure. Furthermore, the large number of smaller haloes in the cluster illustrates that a lot of information is gained in using SUBFIND haloes instead of FoF-groups.

In table 3.1 we list some further characteristics of the halo catalogues. Interestingly, these numbers imply the same conclusions as figures 2.5 and 2.6 did. We see at every redshift that the haloes in the SUGRA model are less massive than those of the other models, implying that evolution of structure in the SUGRA universe is slower. Also, the fact that at more recent times there are slightly more haloes than in other models hints at a lower rate of halo mergers, the main driving force behind hierarchical structure evolution.

3.2 Voids

A large fraction of the total volume of the universe consists of what we call voids; relatively empty regions of space, captured in between the walls, filaments and clusters of the cosmic web. Depending on your definition, voids can make up from 13 to 100% of the total volume (Colberg et al., 2008); evidently the implementation of these different definitions in void finding algorithms yields vastly different results. If we are to do statistics on voids we therefore need a plausible definition and a corresponding void finder. Based on Colberg et al. (2008) we chose to use the Watershed Void Finder (WVF) (Platen et al., 2007). This void finder seem to do the best job in reproducing what we would identify by eye as voids. It works by “growing” voids from the minima of the dark matter density field.

Below we elaborate on this void finding algorithm. For a great general overview on void properties and to see the WVF in action, see Platen (2009).

3.2.1 Watershed Void Finder

The basic principle behind the WVF algorithm is perhaps best illustrated by its analogy with flooding an area of hills and valleys with water, see figure 3.3 and its caption. The valleys can be identified with voids and the ridges can be identified with walls and filaments.

From Platen et al. (2007), the basic steps taken in the algorithm are the following:

1. Create a *density field* from the particle distribution (e.g. using the DTFE (Schaap, 2007; Schaap and van de Weygaert, 2000)).
2. For practical processing purposes the field must be *sampled on a regular grid*. It is subsequently *smoothed* by a Gaussian kernel, the density values are *discretized* and

z	<i>Model</i>	N_{haloes}	m_{mean}	σ_m	m_{max}
0.00	WMAP3	567119	$1.1 \cdot 10^2$	$7.0 \cdot 10^2$	$1.7 \cdot 10^5$
	SUGRA	582882	$9.5 \cdot 10^1$	$4.9 \cdot 10^2$	$8.9 \cdot 10^4$
	RP	575618	$1.0 \cdot 10^2$	$6.0 \cdot 10^2$	$9.6 \cdot 10^4$
	EQn	577526	$1.0 \cdot 10^2$	$5.6 \cdot 10^2$	$9.4 \cdot 10^4$
	EQp	572176	$1.0 \cdot 10^2$	$6.0 \cdot 10^2$	$9.7 \cdot 10^4$
0.10	WMAP3	561496	$1.0 \cdot 10^2$	$5.9 \cdot 10^2$	$9.5 \cdot 10^4$
	SUGRA	573099	$9.0 \cdot 10^1$	$4.3 \cdot 10^2$	$7.3 \cdot 10^4$
	RP	569134	$9.8 \cdot 10^1$	$5.3 \cdot 10^2$	$9.5 \cdot 10^4$
	EQn	569398	$9.5 \cdot 10^1$	$4.9 \cdot 10^2$	$8.6 \cdot 10^4$
	EQp	565901	$9.7 \cdot 10^1$	$5.3 \cdot 10^2$	$9.6 \cdot 10^4$
0.25	WMAP3	551935	$9.4 \cdot 10^1$	$4.9 \cdot 10^2$	$8.8 \cdot 10^4$
	SUGRA	558191	$8.3 \cdot 10^1$	$3.6 \cdot 10^2$	$5.1 \cdot 10^4$
	RP	556933	$9.0 \cdot 10^1$	$4.4 \cdot 10^2$	$7.8 \cdot 10^4$
	EQn	556652	$8.8 \cdot 10^1$	$4.1 \cdot 10^2$	$6.5 \cdot 10^4$
	EQp	554948	$9.0 \cdot 10^1$	$4.5 \cdot 10^2$	$7.8 \cdot 10^4$
0.51	WMAP3	530669	$8.3 \cdot 10^1$	$3.6 \cdot 10^2$	$5.1 \cdot 10^4$
	SUGRA	525572	$7.4 \cdot 10^1$	$2.7 \cdot 10^2$	$3.9 \cdot 10^4$
	RP	531403	$8.0 \cdot 10^1$	$3.3 \cdot 10^2$	$4.5 \cdot 10^4$
	EQn	527737	$7.8 \cdot 10^1$	$3.1 \cdot 10^2$	$4.3 \cdot 10^4$
	EQp	529353	$8.0 \cdot 10^1$	$3.3 \cdot 10^2$	$4.5 \cdot 10^4$
1.00	WMAP3	469725	$6.7 \cdot 10^1$	$2.1 \cdot 10^2$	$1.9 \cdot 10^4$
	SUGRA	446675	$6.0 \cdot 10^1$	$1.7 \cdot 10^2$	$1.6 \cdot 10^4$
	RP	464471	$6.5 \cdot 10^1$	$2.0 \cdot 10^2$	$1.8 \cdot 10^4$
	EQn	455982	$6.3 \cdot 10^1$	$1.9 \cdot 10^2$	$1.7 \cdot 10^4$
	EQp	463068	$6.5 \cdot 10^1$	$2.0 \cdot 10^2$	$1.8 \cdot 10^4$
2.04	WMAP3	289375	$4.6 \cdot 10^1$	$8.5 \cdot 10^1$	$6.3 \cdot 10^3$
	SUGRA	248194	$4.2 \cdot 10^1$	$6.9 \cdot 10^1$	$3.4 \cdot 10^3$
	RP	278477	$4.5 \cdot 10^1$	$8.0 \cdot 10^1$	$5.2 \cdot 10^3$
	EQn	264882	$4.4 \cdot 10^1$	$7.6 \cdot 10^1$	$3.7 \cdot 10^3$
	EQp	275137	$4.5 \cdot 10^1$	$7.8 \cdot 10^1$	$4.2 \cdot 10^3$
2.98	WMAP3	144188	$3.6 \cdot 10^1$	$4.5 \cdot 10^1$	$1.9 \cdot 10^3$
	SUGRA	113083	$3.3 \cdot 10^1$	$3.8 \cdot 10^1$	$1.5 \cdot 10^3$
	RP	135668	$3.5 \cdot 10^1$	$4.3 \cdot 10^1$	$1.9 \cdot 10^3$
	EQn	125526	$3.4 \cdot 10^1$	$4.1 \cdot 10^1$	$1.7 \cdot 10^3$
	EQp	131470	$3.5 \cdot 10^1$	$4.2 \cdot 10^1$	$1.7 \cdot 10^3$
3.80	WMAP3	63392	$3.0 \cdot 10^1$	$2.8 \cdot 10^1$	$1.1 \cdot 10^3$
	SUGRA	45273	$2.8 \cdot 10^1$	$2.4 \cdot 10^1$	$9.1 \cdot 10^2$
	RP	58349	$3.0 \cdot 10^1$	$2.7 \cdot 10^1$	$1.0 \cdot 10^3$
	EQn	52012	$2.9 \cdot 10^1$	$2.6 \cdot 10^1$	$9.5 \cdot 10^2$
	EQp	55148	$2.9 \cdot 10^1$	$2.6 \cdot 10^1$	$9.9 \cdot 10^2$

Table 3.1: Characteristics of the halo catalogues obtained from the DE simulations, provided by Klaus Dolag. Masses are in units of $10^{10} M_{\odot}$.

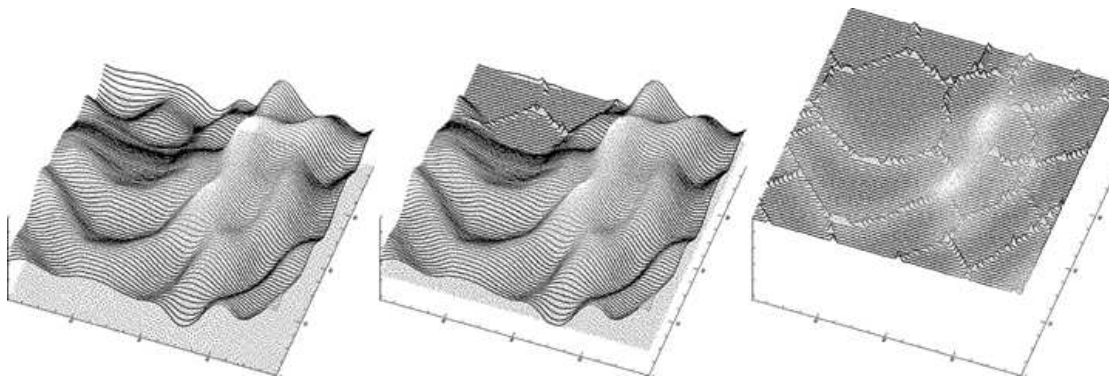


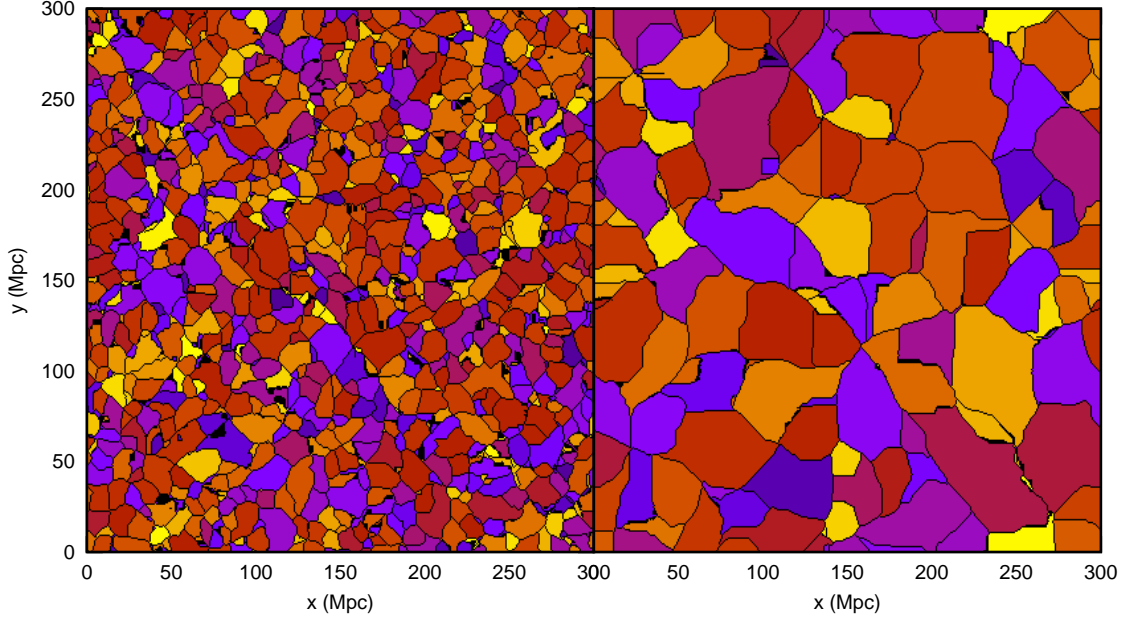
Figure 3.3: “Three frames illustrating the principle of the WST” (Watershed Transform, the mathematical formalism behind the WVF). “The left-hand frame shows the surface to be segmented. Starting from the local minima the surrounding basins of the surface start to flood as the water level continues to rise (dotted plane initially below the surface). Where two basins meet up near a ridge of the density surface, a ‘dam’ is erected (central frame). Ultimately, the entire surface is flooded, leaving a network of dams that defines a segmented volume and delineates the corresponding cosmic web (right-hand frame).” From Platen et al. (2007).

the map is *cleaned* of pixel noise using operations from mathematical morphology (a field concerned with image analysis).

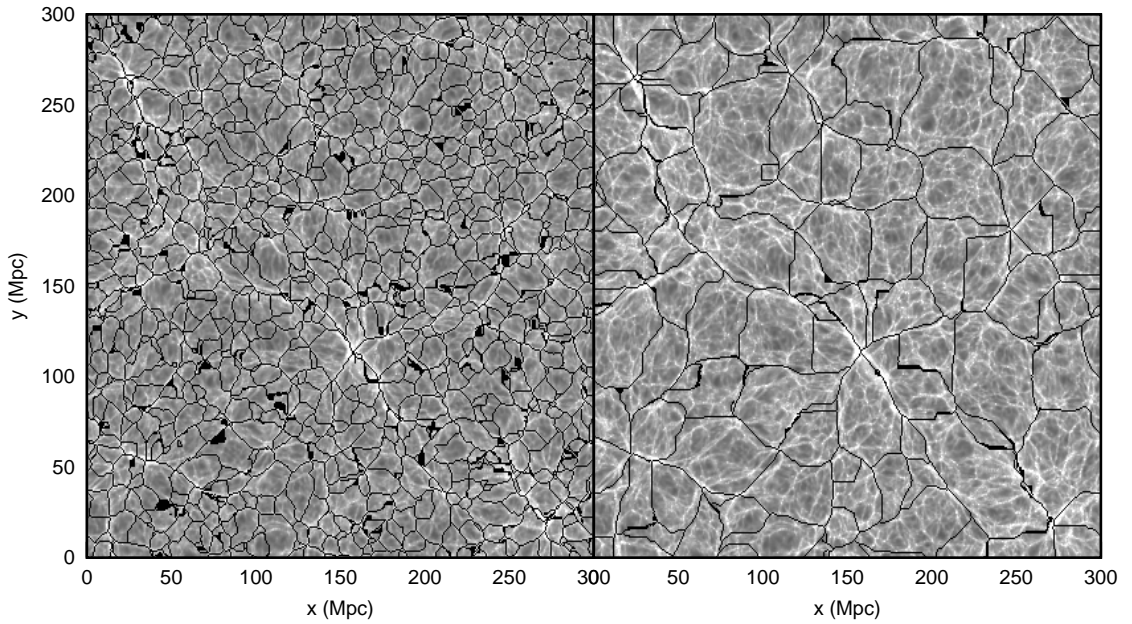
3. *Field minima* are determined; these are pixels that are surrounded by higher density pixels only.
4. The field is then *flooded*, starting at the positions of the minima and adding to its basin the adjacent pixels that are subsequently flooded when the flooding threshold becomes higher than the adjacent pixel’s value (this is illustrated in figure 3.3).
5. Once a pixel is reached by two basins, i.e. the level of flooding makes the two basins join, this pixel is identified as a segmentation *boundary*. The flooding continues until all pixels have either been identified as part of a segment, or void, or as a boundary.
6. A final correction is made to deal with the effects of the intrinsic hierarchical nature of the void distribution: boundaries with underdensities lower than a certain threshold (say $\delta < -0.8$, the characteristic mature void density of a (highly simplified, top-hat spherically expanding) void model (Neyrinck, 2008; Sheth and van de Weygaert, 2004)) are removed. This step can be omitted at the cost of having to deal with some noise effects and the small scale irregularities in the void density profiles.

The result of this procedure on the WMAP3 dataset is shown in figure 3.4 for two different smoothing radii. In both cases the void boundaries follow the filamentary structures quite precisely. In the $r_f = 6.0h^{-1}\text{Mpc}$ image it is immediately apparent that a lot of void substructure is lost, which may lead one to believe that smoothing is a bad thing. Nonetheless, without smoothing of pixel-to-pixel noise, a lot of false identifications will occur. For practical reasons we can not go below the pixel size of

$0.78125h^{-1}\text{Mpc}^1$. Because we also use some density fields with even higher pixel sizes and we want our methods to be consistent between datasets we chose $1.5h^{-1}\text{Mpc}$ as our minimum filtering radius.



(a) Void distribution only; random colors.



(b) Void borders (black lines) overlaid on the density field.

Figure 3.4: The distribution of voids in the same slice of the WMAP3 simulation as in previous images. For the left panels we used a Gaussian filter radius $r_{f,G} = 1.5h^{-1}\text{Mpc}$, for the right panels $r_{f,G} = 6.0h^{-1}\text{Mpc}$.

Two notable features of the WVF are that it is essentially parameter free (the only

¹The discrete Fourier transformations used in the algorithm would produce effects of aliasing.

parameters used are for filtering out discreteness noise) and that it does not make any geometric assumptions so voids can take any shape. This latter feature is especially important, since we need an unbiased shape determination to investigate void shape statistics. We see in figure 3.4 that indeed the irregular shapes of the voids are perfectly conserved.

3.2.2 Void properties

Having determined our void distribution we can calculate a few properties of each of the voids, including some fits of shape parameters. We define the geometric center of a void as the volume averaged center of the void’s grid cell positions. Its volume we can determine by simply counting the number of cells.

The shape of a void can be fitted by an ellipse in the following way. We can calculate the void’s inertia tensor I_{ij} :

$$I_{ij} = \sum_k (\delta_{ij} \vec{x}_k^2 - x_{ki} x_{kj}) , \quad (3.2)$$

where we sum over all cells k belonging to the void, where \vec{x}_k is the distance vector of the k -th void cell to the void’s center and where δ_{ij} is the Kronecker delta. We can use a sum instead of a full integral because of the discrete nature of the grid on which the voids are defined. Like Shandarin et al. (2006), we assume the density of the void to be uniform (thus focussing on the geometrical properties of the void only and avoiding possible complications introduced by the overdense regions in and around the void).

Following Shandarin et al. (2006) we can now fit an ellipsoid to the void by deriving the properties of an ellipsoid having the same (diagonalized) inertia tensor as the void. For an ellipsoid we can derive the following relationships between the ellipsoid semi-axes a , b and c (for which $a \geq b \geq c$) and the eigenvalues of the inertia tensor I_{xx} , I_{yy} and I_{zz} :

$$a^2 = \frac{5}{2} (I_{yy} + I_{zz} - I_{xx}) \quad (3.3)$$

$$b^2 = \frac{5}{2} (I_{zz} + I_{xx} - I_{yy}) \quad (3.4)$$

$$c^2 = \frac{5}{2} (I_{xx} + I_{yy} - I_{zz}) . \quad (3.5)$$

Using these values from the diagonalized void inertia tensor we can define its shape parameters: the ellipticity² $\epsilon = 1 - c/a$ or conversely the sphericity $s = c/a$, the oblateness (flattening) $p = b/a$ and the prolateness $q = c/b$ (Aragón Calvo, 2007, p. 136). We can also calculate the ellipse’s volume $V = \frac{4}{3}\pi abc$.

We compare the void distribution to their fitted ellipses in figure 3.5. On first glance the ellipses seem to approximate the void shapes very well. Of course the fits are never perfect due to the porosity of void interiors and irregularity of the void edges. This causes the ellipse volumes to differ from the actual void volumes (determined by counting the

²For consistency, we follow Park and Lee (2007) in using the term ellipticity for this quantity. This term may not be the most adequate, as its semantics imply a general description of the shape of an ellipsoid, whereas the total shape of an ellipsoid needs at least two parameters. “Asphericity” may therefore have been a better term.

void grid cells from the WVF output) by an average factor of 1.08. This slight error in the void size estimate has no influence on the shape parameters of the voids.

One more important feature of the WVF is that, as Platen et al. (2008) showed, the orientation of the void ellipsoid of a WVF void is intimately coupled to the tidal field. This is especially important for our project, as the coupling of the tidal tensor to void shapes is exactly what the theory from Park and Lee (2007) is based on.

We will use these approximate shape parameters in our analysis in chapter 4.

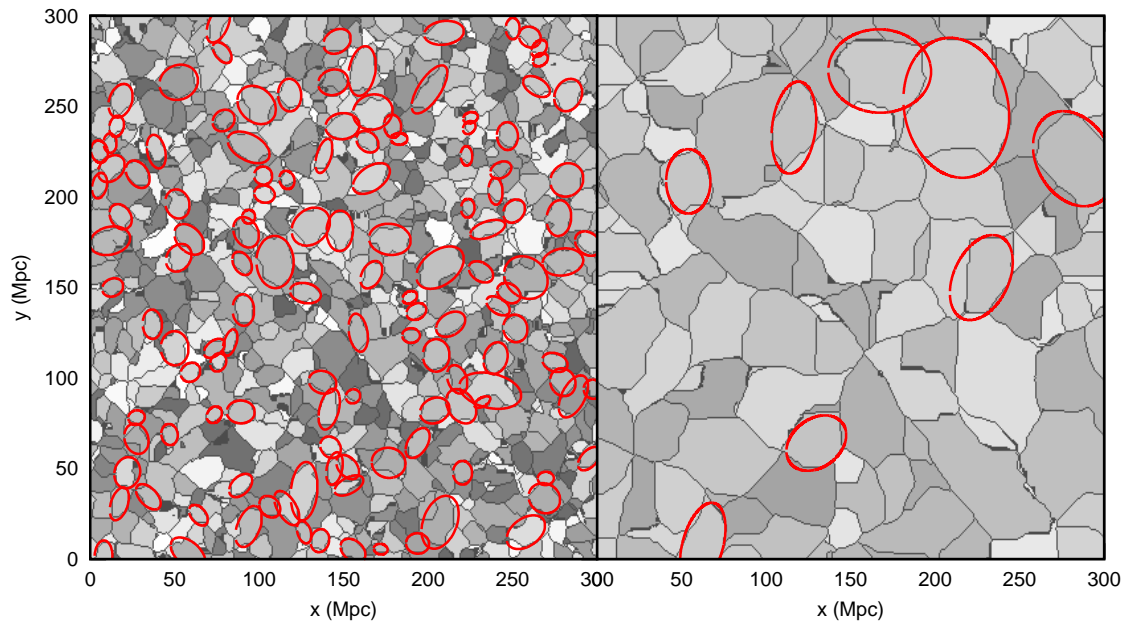


Figure 3.5: The void distributions from figure 3.4 overlaid with some fitted ellipses.

4.1 Introduction

In this section we will study in detail the contents of our datasets. Our main objective is to ascertain the viability of the use of voids as a probe of the nature of dark energy. To this end we use a variety of statistical tools. We introduce the techniques used and present the statistics obtained.

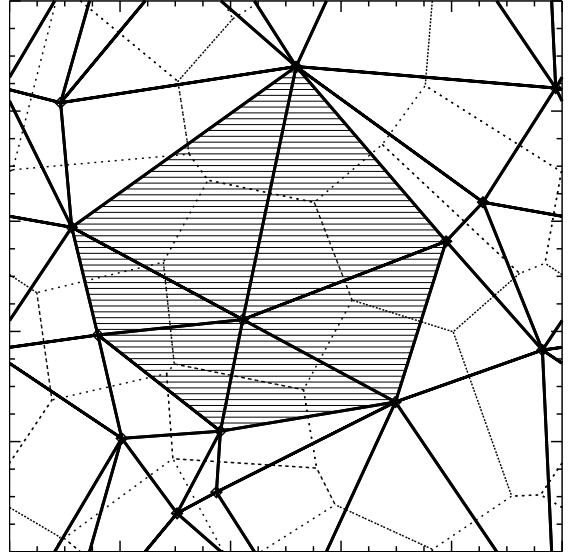
At the core of many of the methods for structural analysis in astronomy lies the need for a careful determination of the (dark matter) density field. We chose to work with the Delaunay tessellation Field Estimator (Schaap and van de Weygaert, 2000; Schaap, 2007; Platen et al., 2007). When intricate structures, like those in the cosmic web, are involved, this method has significant advantages over e.g. TSC and SPH. This concerns its ability to resolve the substructure in high-density regions, its sensitivity to shape so that it can follow filaments and flattened sheets, and the successful interpolation through low-density regions.

To further quantify the distribution of matter in our simulations we have obtained one-point distribution functions. This statistical measure is the first order characterization of the density field. We apply this measure over a range of scales. The first measure of clustering is the two-point correlation function, which we have also determined.

The main part of our analysis consists of the determination and dissection of void statistics. To ascertain the level of “voidiness” we apply the extensively studied (Lachièze-Rey and Maurogordato, 1987; Einasto et al., 1991; Sheth, 1996) void probability function (VPF) by White (1979). The VPF has some shortcomings when dealing with high resolution simulations. To overcome these, we developed a modified version of the VPF (mVPF). We analyse the results and assess the viability of these functions as probes of the nature of dark energy. We show that redshift space distortions will significantly obscure the signal we are looking for.

In order to account for detailed size and shape distributions of our void samples we need a void finding algorithm that takes these properties into account. To this end we will use the Watershed Void Finder described in section 3.2.1. We compare our findings to those of Lee and Park (2009) and Lavaux and Wandelt (2010). We find that the claims from these previous works may be based on a formerly hidden degeneracy with

Figure 4.1: Delaunay tessellation of a 2D distribution of points (the vertices of the fat lines). The Delaunay tessellation is the dual graph of the Voronoi tessellation (dotted lines). Voronoi tessellation borders are drawn at the sites of equal distance to the two nearest points. A Voronoi cell containing point p is thus made up of all the space that is closer to p than to any other point in the distribution. The Delaunay tessellation can be defined in terms of the Voronoi tessellation. Its lines connect points p and q only if they have adjacent Voronoi cells.



σ_8 . This was a surprising result; it sheds new light on the premises of the hypothesis from Park and Lee (2007) that void shapes depend on mean ellipticity.

4.2 Density field

We used the Delaunay tessellation Field Estimator (DTFE) by Schaap and van de Weygaert (2000); Schaap (2007) to estimate the 3D matter density fields in our simulations. Density fields are an invaluable tool in the field of structural analysis. One can build highly efficient algorithms that bypass the need for processing all the points in the full particle set. One example is the WVF algorithm, which uses density fields as input. Another advantage is that discreteness effects caused by the limited mass-resolution of N-body simulations are avoided. Density field estimators usually take care that these effects are smoothed out.

The DTFE uses the volumes of Delaunay tessellation cells to estimate densities. First, it builds a Delaunay tessellation out of a set of points (see figure 4.1). It then calculates a density for each point using the volume of its so-called “contiguous Voronoi cell” $W_{\text{Vor},i}$ (the shaded cell in figure 4.1). These quantities relate like

$$\rho \propto W_{\text{Vor},i}. \quad (4.1)$$

Finally, it interpolates between the points at which the densities were determined. The interpolated values are determined for a regular 3D grid.

Our simulation boxes have periodic boundary conditions. To accommodate for this, the DTFE adds a particle layer around the box to avoid tessellation errors at the edges. The particles that are added to one side are taken from the opposite side. This creates the illusion of a periodic box in the relevant central area. As long as all relevant particles are surrounded by a thick enough layer, there will be no errors in the density estimation. This is because the tessellation is stable as long as all its surrounding particles are there. If there are too little particles, i.e. the neighbours of the relevant particles change, the tessellation will be different and periodic boundary conditions will not be satisfied. The

thickness of the extra particle layers should be determined by the particle density at the edges.

We used the DTFE because it is especially well suited for cosmological particle distributions. The tessellations preserve the great amount of detail in clusters and filaments. Furthermore, it is highly sensitive to the shape of the matter distribution and it can successfully interpolate through low-density regions. The latter two properties make it especially well suited to our purposes of probing the shapes of the lowest-density regions.

Other density estimators like the triangular shaped cloud (TSC) algorithm have intrinsic scale assumptions (the pixel scale in the case of TSC). In figure 4.2 these estimators are compared. The TSC densities in the right panel are more diffuse in high density regions. The DTFE preserves substructure in clusters and filaments. The TSC algorithm behaves even worse in low density regions like the voids. Noisy artefacts are clearly visible in the larger voids, whereas the DTFE voids are far smoother. This especially makes the DTFE far better suited for our void analyses than the TSC method. Comparisons in Schaap (2007) of the kernels of DTFE, TSC and SPH (smoothed particle hydrodynamics) methods and in Pelupessy et al. (2003) of the DTFE to SPH density estimation both favored the DTFE on similar premises.

The price to pay is that the DTFE is quite a memory and cpu intensive algorithm. The computation of the tessellation needs about 25 gigabytes for 256^3 particles. To deal with the large numbers in our high resolution datasets of 768^3 particles, we needed a special parallel algorithm¹.

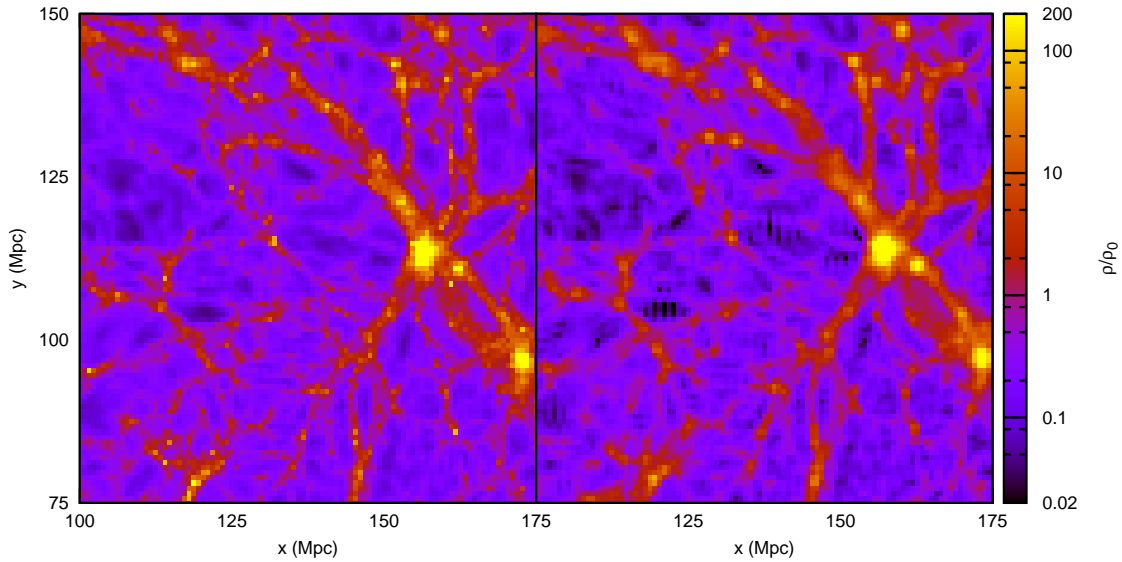


Figure 4.2: DTFE (left) vs TSC (right) density fields.

¹Erwin Platen kindly provided us with this parallel version of the DTFE that splits the total cube in smaller cubes. The density field in a sub-cube can then be calculated independently of the other sub-cubes. The boundary conditions are similar. At the edges where the sub-cube touches other sub-cubes a layer of particles is taken from the neighbouring sub-cube.

4.3 Point distribution statistics

Both redshift surveys and N-body simulations provide us with a set of object coordinates in three-dimensional space. They can represent stars, galaxies or discretizations of a continuous dark matter density field. Whatever their origin, they share the fact that we can use spatial statistics to characterize their clustering. The field of spatial statistics deals with random point sets. It delivers a handhold for the characterization of any point distribution. For a comprehensive overview on these statistics in cosmology and the study of large scale structure we refer to Martinez and Saar (2002, ch. 3).

We focus on the lower order statistics as higher orders are hard to interpret, are difficult to determine reliably due to propagation of errors and are not the focus of our analysis². We obtain one-point probability density functions and two-point correlation functions. The first will serve as a direct measure of the density distribution and the second will inform us on the “average degree of irregularity as a function of characteristic length scale” (Peebles, 1973), i.e. the amount of clustering on different scales.

4.3.1 One-point probability density function

The one-point probability density function (pdf) gives a direct measure of the distribution of matter. Its usefulness stems from the simplicity to which it reduces the complex richness of the full density distribution. It is a natural first measure of the density distribution.

Definition and estimation

The one-point pdf $f_1(\rho)$ is defined through the probability $P(\rho)$ of a location in a density distribution having density ρ :

$$P(\rho) = f_1(\rho)d\rho. \quad (4.2)$$

This function can be estimated in several ways. We could simply estimate the density field on a grid (e.g. using the DTFE) and count the number of times a density ρ is found. Divide this by the total number of density cells and we have an estimate of $f_1(\rho)$. This method has a drawback: it is not a direct measure of the particle distribution due to the step of averaging to a grid. Information will inevitably be lost in this step and this introduces a systematic error.

A more advanced method was developed by Szapudi (1998). He treats the discrete particle distribution as a function space in which the particles act as discrete step-functions. This is a mathematically exact method. This would seem the best method, but its implementation is non-trivial.

The method we used is based on *counts in cells* and for this we have three main reasons:

- We wanted a direct measure of the particle distribution, independent of density field estimators.

²“Since the two-point correlation function and its Fourier counterpart, the power spectrum, do not contain phase information, higher order statistics are needed for full description of the (highly non-Gaussian) galaxy density field,” (Szapudi, 1998). Clearly, we will not need this. As Peebles (1973) put it: “One observes that analysis in extragalactic astronomy almost always is beclouded with difficulties of interpretation. It is hoped that by concentrating on a statistical measure that does admit of direct and simple interpretation one may be able to deal more directly with ambiguities of the phenomena.”

- The method should be easy to implement and should not be too computationally intensive.
- It would be nice if the results would be reusable for other statistics.

These reasons led us to conclude that counts in cells were the way to go. Counts in cells are simply the number of particles in randomly placed cells with volume V . They can do more than merely provide an approximation of $f_1(\rho)$. Their wide range of uses includes estimation of the void probability function of section 4.4, the estimation of N -th order correlation functions (White, 1979; Martinez and Saar, 2002) and the estimation of basic cosmological parameters like σ_8 .

By counting the number of particles in randomly placed cells of volume V we can estimate $f_1(\rho)$ on a linear scale of $\sim V^{1/3}$. Our method of estimation is as follows. We throw N_{sph} spheres of radius R at random positions in our particle distribution. We then count the number of particles $N_{\text{sph},i}$ in each sphere. This number is proportional to the density in the sphere:

$$\rho = \frac{N_{\text{sph},i}}{N_R}, \quad (4.3)$$

where

$$N_R = \frac{V_{\text{sph}}}{V_{\text{box}}} N_{\text{tot}} \quad (4.4)$$

is the average number of particles in a sphere of radius R . We repeat this procedure for a range of radii. We used an efficient algorithm based on a “grid search” method. This divides the particles in grid cells with a linear size that is optimized for the scale at which the statistical measure is taken.

The distribution that follows from this is not strictly equal to $f_1(\rho)$. What we really measure is the probability $P(N, V)$ that a randomly placed sphere of volume V contains N particles. This function is explicitly dependent on V and $f_1(\rho)$ would not be uniquely defined by our counts in cells approximation. However, due to the discrete nature of matter, a density ρ must always be defined on a certain smoothing scale. We can thus state that indeed

$$f_1(\rho(V)) = P(\rho, V), \quad (4.5)$$

where we replaced $P(N, V)$ by $P(\rho, V)$ using equation 4.3. By taking the counts in cells of different volumes we can thus easily determine the one-point pdf on different scales, which is an added bonus of our method.

Results

The above procedure results in the scale dependent pdfs of figures 4.3 and 4.4.

In figure 4.3 the dependence on the scale of approximation is immediately apparent. The distribution at $1h^{-1}$ Mpc is wider than that at $4h^{-1}$ Mpc. The density variations on this scale are hence larger than at larger scales. This is an effect of the cosmological principle that on large scales the universe becomes more and more homogeneous. Another interesting fact that can be learned from these plots is that it seems that there are far more empty regions on a $1h^{-1}$ Mpc scale than on a $4h^{-1}$ Mpc scale. From the different lines we can learn about the evolution of density perturbations. At high redshift, the pdf is nicely centered around $\delta = 0$ and the deviations from this value become

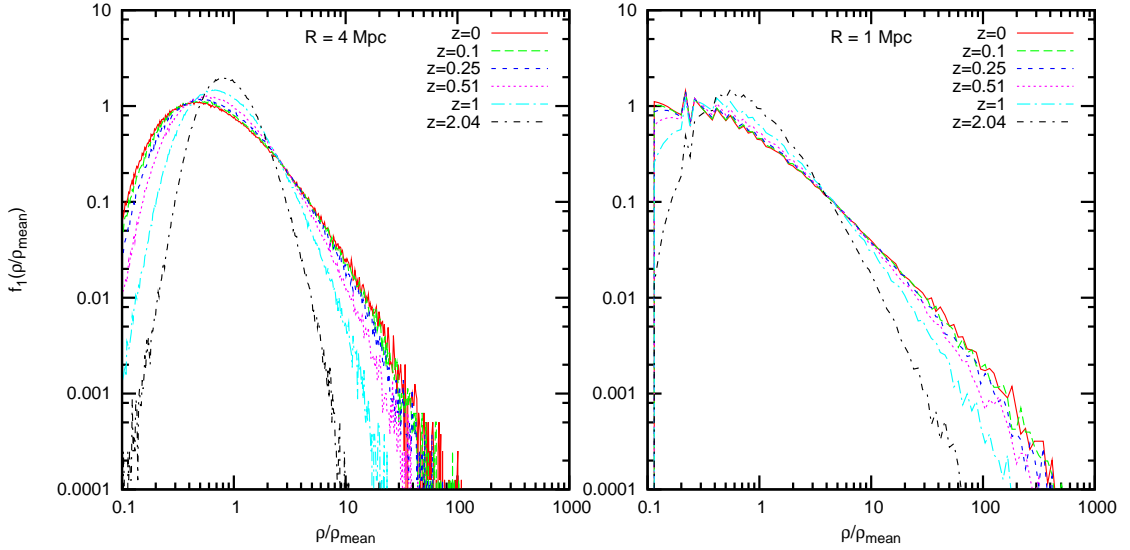


Figure 4.3: The one-point pdf $f_1(\rho)$ (density normalized to the average density) approximated at two different scales (1 and $4h^{-1}$ Mpc). The different lines represent different redshifts of the WMAP3 simulation.

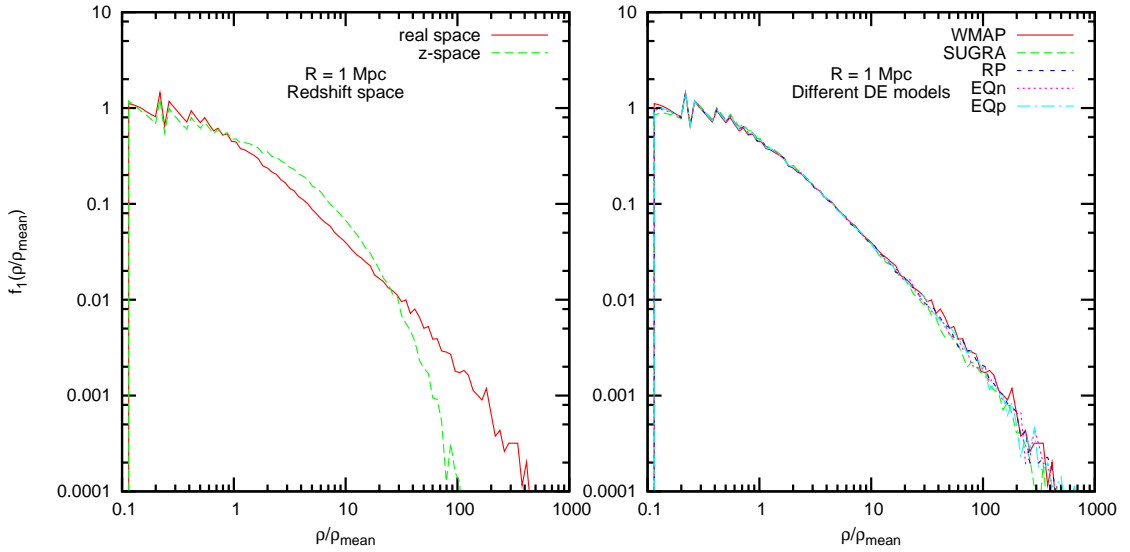


Figure 4.4: The one-point pdf $f_1(\rho)$ (density normalized to the average density) approximated at a scale of $1h^{-1}$ Mpc. The left panel shows $f_1(\rho)$ the WMAP3 simulation in real and in redshift space. The right panel shows the five different DE models at $z = 0$.

more normally distributed as the redshift goes up. This is a probe of the evolution from a homogeneous initial state to the current situation in which structure dominates.

From figure 4.4 we learn two important facts. We can see that redshift space distortions may cause some complications in our further measurements. The significant change in the shape of $f_1(\rho)$ when transforming to redshift space (left panel) is contrasted with the very slight changes due to the different models of DE (right panel). Useful as it may be, it is clear that both the intrinsic scatter in the DE model pdfs and the redshift space

distortions make this statistic unsuited for discriminating between models of DE.

4.3.2 Two-point correlation function

Our approximation of the one-point pdf can show density statistics on any scale. Where we to try this, we would need to calculate a new pdf for every scale we are interested in. The two-point correlation function is built specifically for the purpose of showing the amount of clustering on any scale. It encapsulates scale dependent clustering information in one function. It was extensively used and studied in the 70's (Peebles, 1973; Peebles and Groth, 1976; Groth and Peebles, 1977; White, 1979) and in later years (Davis and Peebles, 1983; Landy and Szalay, 1993; Hamilton, 1993). Through the use of this statistic we could potentially probe the influence of different DE models on the manner of clustering.

Definition and estimation

The two-point correlation function $\xi(r = |x_1 - x_2|)$ is defined in its relation with the joint probability dP_{12} that two infinitesimally small spheres centered on x_1 and x_2 with volumes dV_1 and dV_2 each contain a point of the distribution:

$$dP_{12} = \bar{n}^2 [1 + \xi(r)] dV_1 dV_2, \quad (4.6)$$

where \bar{n} is the mean number density of particles in the distribution. In general, $\xi(x_1, x_2)$ is dependent on both positions, but for a homogeneous point field (which is a fair assumption on large scales) we can simplify to

$$\xi(x_1, x_2) = \xi(|x_1 - x_2|) = \xi(r). \quad (4.7)$$

It will only depend on the distance r between the two volumes, because there is no direction dependence in a homogeneous distribution.

In order to estimate $\xi(r)$ we thus need to estimate the probability of two particles being a distance r apart. Many methods have been developed and forwarded to accomplish this (Davis and Peebles, 1983; Rivolo, 1986; Landy and Szalay, 1993; Hamilton, 1993). A number of popular methods use a Monte Carlo estimation of the total volume in which the particle distribution is defined. This is a very useful way to deal with the complicated shapes of galaxy distributions from surveys. There are, however, a number of statistical issues that need to be overcome. This can greatly increase the complexity of the algorithm.

Our particle distributions live in the highly regular environment of a periodic box. Because of this we do not need the flexibility of Monte Carlo approximations. One of the simplest estimators is the one by Rivolo (1986). The Rivolo estimator's results hardly differ from those of other, more complicated estimators (see figure 3.7 of Martinez and Saar (2002)). This simple approach will thus more than suffice.

The Rivolo estimator is given by the following equation:

$$\hat{\xi}_{\text{RIV}}(r) = \frac{V(W)}{N^2} \sum_{i=1}^N \frac{n_i(r)}{V_i(r)} - 1, \quad (4.8)$$

where $V(W)$ is the total volume of the box, N is the total number of particles in the sample used for the estimation, the sum is over all particles, $n_i(r)$ is the number of

neighbours of particle i in the distance interval $[r, r + dr]$ and $V_i(r)$ is the volume of the shell centered on particle i with radius r and thickness dr .

Results

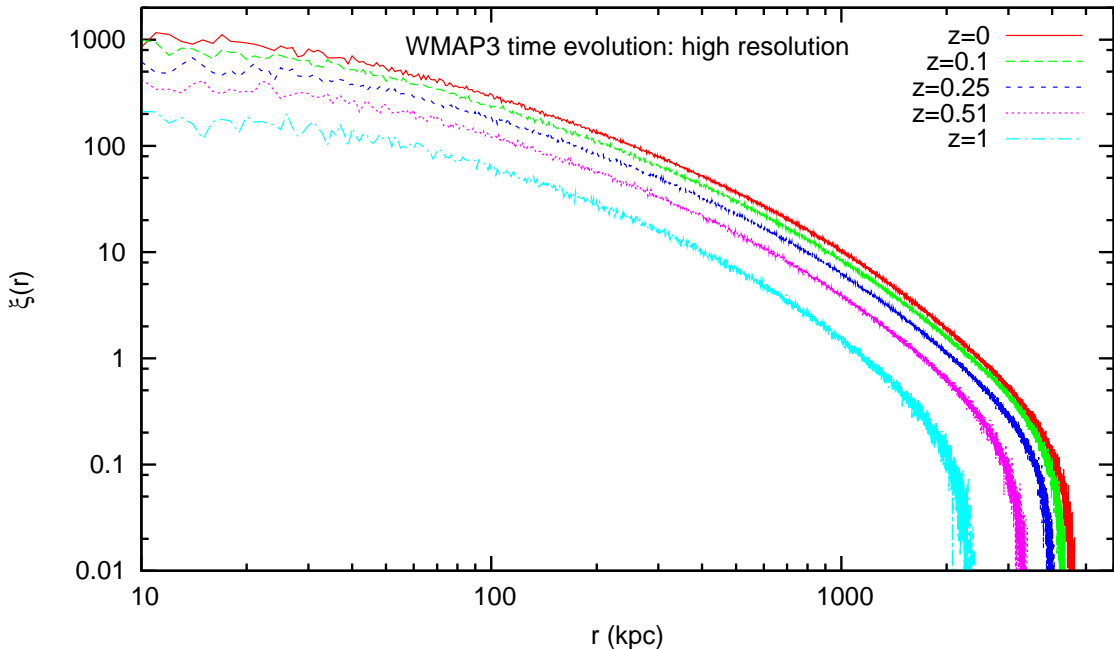


Figure 4.5: Two-point correlation functions for several timesteps of the WMAP3 simulation.

In figures 4.5 and 4.6 we show two sets of resulting two-point correlation functions. The one thing that strikes the eye is that there are no features to distinguish the different models and timesteps with. The only thing that seems to change from DE model to DE model and from redshift to redshift is the height of the entire function. For the redshift evolution this can be easily understood. The distribution becomes more homogeneous. This causes small scale correlations to drop, because the high odds of finding a neighbour at small distances at low redshifts is caused by the growth of dense structures. However, we would expect the models of dark energy to show at least some clearly distinguishing features. The two-point correlation function show no such features. This suggests that the only way to distinguish between models of dark energy is by the amount of clustering they have produced by $z = 0$. This agrees with what we saw in figures 2.5, 2.6 and 2.2.

4.4 Void Probability Functions

4.4.1 Void probability function

Context and definition

The void probability function (VPF) was first defined by White (1979). In section 4.3.1 we discussed the counts in cells probability $P(N, V)$ that a cell of volume V contains N particles. The VPF is a special case of this function for $N = 0$. The resulting function

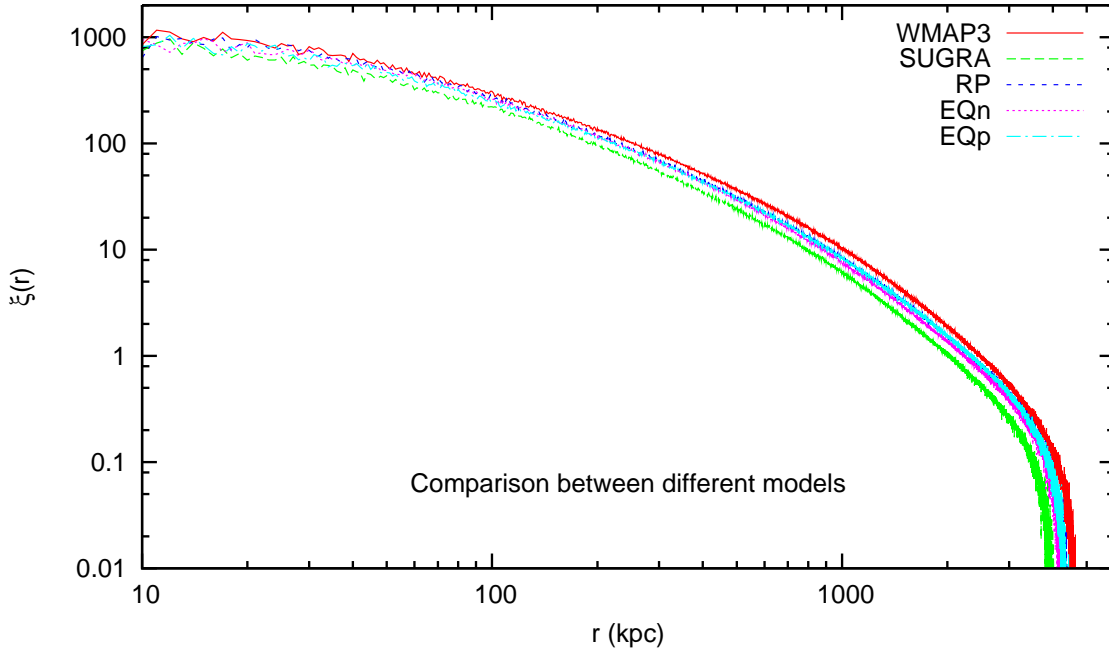


Figure 4.6: Two-point correlation functions for the different DE model simulations at $z = 0$.

$P_0(V)$ is defined as the probability that a randomly placed region of volume V is empty of particles. In spatial statistics this quantity is known as the emptiness probability (Martinez and Saar, 2002).

In the years preceding the VPF’s discovery, a lot of work was done on clustering statistics. Because of this, the main focus of White (1979) was the hierarchy of N-point correlation functions and their interconnectedness. Specifically, the relative influence of lower- versus higher-order correlations was investigated. In this context the VPF was shown to be fundamental to all the other N-point correlation functions. It is in fact directly related to all N-point correlation functions $\xi_i(x_1, x_2, \dots, x_i)$ (Maurogordato, 2006; White, 1979):

$$P_0(V) = \exp \left(\sum_{i=1}^{\infty} \frac{(-n)^i}{i!} \int \dots \int \xi_i(x_1, x_2, \dots, x_i) dV_1 \dots dV_i \right). \quad (4.9)$$

The VPF is easily calculated. This, together with the above relationship makes it extremely useful for probing higher order correlations. The higher order correlations are hard to calculate themselves, but because the VPF contains all of them you can subtract the contributions of lower order (two- and three-point) correlations to obtain the sum of the higher order correlations. As Betancort-Rijo et al. (2009) notes, this does not mean that the VPF determines uniquely all these correlations. The VPF contains an integral, which means that the contributions from different correlations cannot be distinguished. “Two samples could have the same VPF and still differ in some aspect of the clustering,” (Betancort-Rijo et al., 2009). Nevertheless, the VPF can be considered as an interesting clustering measure, complementary to the lower order clustering measures (White, 1979)

As White himself briefly mentions, “it is also of intrinsic interest in view of the large ‘holes’ in the galaxy distribution which are apparent in some recent complete redshift surveys (Gregory and Thompson, 1978).” This is our main focus. The VPF is likely the simplest and easiest to interpret statistic of the (spherical) void volume distribution in a particle box. It will give us insight on the typical sizes of empty regions in the particle distributions. If the evolution of void sizes is affected by models of dark energy, this should clearly show in the VPFs.

Determination

We can easily determine an estimate of the VPF by using the counts in cells we determined earlier (section 4.3.1). We count the spheres with zero particles in them at all radii and divide by the total number of spheres with that radius. Given a sufficient number of spheres this gives a decent approximation of the chance for a sphere of a certain radius to have zero particles in it. We used a million spheres, which is more than enough at most radii. The function already converges when using only 100000 spheres. At higher radii where the VPF drops to zero (there are no more empty regions with those radii) noise levels will rise, but this is inevitable.

Note that some authors (e.g. Vogeley et al. (1991)) use the reduced VPF. This derived statistic measures the deviation of the VPF from a random distribution. It can be used to measure the degree of hierarchical scaling in the galaxy distribution. Under the assumption of a hierarchical galaxy distribution, the N-point correlation functions can be greatly simplified. The reduced VPF can be used to test this assumption, because its behaviour in a hierarchical scenario can be predicted as well, due to its dependence on the N-point correlation functions. We will not use the reduced VPF. The reduced VPF, though useful in its own right, contains no extra information that is relevant to this study.

Results

In figure 4.7 we show a number of VPFs for our particle sets. To the left we show VPFs of the high resolution data. The first panel shows the evolution of the VPF in the WMAP3 model. Below that is a comparison of the five different DE model VPFs in real space. In the third panel we plot the VPFs of the WMAP3 and SUGRA models both in real space and in redshift space. The fourth panel again shows redshift space VPFs of these models, but with four different observer locations, resulting in four different redshift space samplings. This was done to take into account environmental effects like the “fingers of god”.

The two right panels show the VPFs for our halo distributions. The top right panel shows the evolution of the WMAP3 model in the halo distribution. The bottom right panel contains a comparison of the different DE model halo VPFs. Both of these panels contain a zoom-in on a part of the function.

Except for the two time evolution panels, all the VPFs are determined at $z = 0$.

Discussion

The DM distribution VPFs seem rather potent on first glance. In the upper two left panels we can see that indeed in principle the differences in the void distribution are

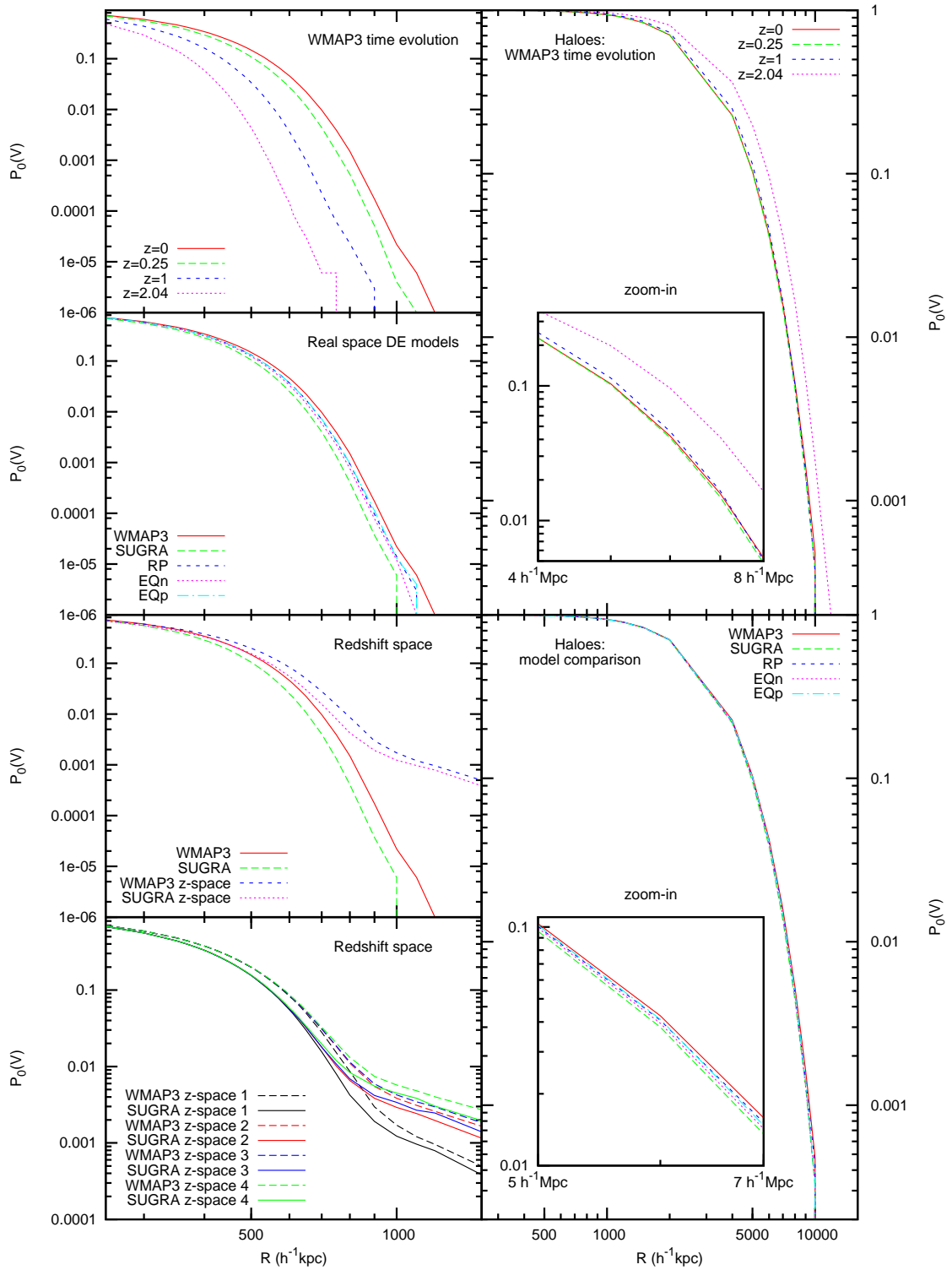


Figure 4.7: Void probability functions. The left panels show VPFs of the complete DM particle sets. The right panels show VPFs for the derived halo distributions.

measurable using VPFs. The fact remains that they are rather small, especially the differences between models. The largest difference is between the WMAP3 and SUGRA models.

The WMAP3 time evolution panel shows us the expected result that voids grow in time. Note that the plots are logarithmic and so the growth is actually quite large. The odds of finding empty regions at the higher scales increases by several orders of magnitude through time.

In the third panel we compare the SUGRA and WMAP3 models in redshift space. Although both VPFs shift upwards significantly, meaning that voids become larger as indeed we saw before in figure 2.8, the relative difference between the models' VPFs is preserved.

The lower panel shows that the specific way of transformation to redshift space has its impact on the VPF. We transformed the two DM particle boxes to redshift spaces in four different ways, by placing the observer at four different locations. In every redshift space realization we see that still the relative difference between model VPFs is preserved. Also, at small radii the VPFs are stable under different redshift space transformations. However, at large radii the VPFs of different redshift spaces diverge. Redshift space distortions have a clear impact on the large scale part of the VPFs.

For our purpose, this makes the VPF useless at these radii. The differences between models are smaller than the scatter caused by the redshift space transformation. At low radii the VPF may still be useful though.

Looking at the VPFs of the halo distributions we find even stronger distortions. We see in the upper plot that the effects of VPF density dependence start to dominate. The density of halo particles at $z = 2.04$ is half that at $z = 0$ (see table 3.1). Because, at this density, spheres are twice as likely to be empty the $z = 2$ VPF is shifted to the right of the lower redshift ones, even though it is not twice as far, meaning that indeed it should in fact be to the left like in the DM distributions plot (top left panel). In the zoom-in box we show that the $z = 0.25$ data indeed still lies to the left of the $z = 0$ data; the halo density difference between those redshifts is far lower. In general though it is clear that the lower number density of the halo distributions has a negative impact on the measurability of the VPF differences.

The same conclusion can be drawn from the bottom right panel, showing the halo distribution VPFs of different models at $z = 0$. The order seen in the second highest panel to the left is still there; the void size information is not lost completely. Nevertheless, the differences are very small, certainly smaller than the scatter introduced by a redshift space transformation.

We can conclude that the VPF is unsuited for probing different models of DE. Redshift distortions are too large for the differences to be measurable in halo samples. As these are meant to represent galaxies, we can disqualify the VPF for use in galaxy surveys as a measurement of the nature of DE.

4.4.2 Modified void probability function

Motivation and definition

The VPF was originally devised as a mathematically useful measure of clustering; its application to voids was secondary. In recent years, however, voids themselves have become the objects of study. The need for specific void statistics is more pressing. This

led us to take the VPF as our starting point for defining a slightly more appropriate measure of the void distribution.

Voids are never truly and absolutely empty (Sheth and van de Weygaert, 2004). This fact lead us to define a modified void probability function (MVPF) based on a certain density threshold instead of pure emptiness³. We define the MVPF $P_\delta(V)$ as the probability that a void i has an overdensity δ_i of $\delta_i \leq \delta$.

Like the VPF, we can use the counts in cells to determine this function. First determine the expected mean number of particles N_R in a sphere of radius R :

$$N_R = \frac{V_{\text{sph}}}{V_{\text{box}}} N_{\text{tot}}. \quad (4.10)$$

We divide all the counts in cells by N_R and subtract by 1. In this way we convert the count in a cell i to an overdensity δ_i in that cell:

$$\delta_i = \frac{N_i}{N_R} - 1. \quad (4.11)$$

$P_\delta(V)$ is then the number of cells i having $\delta_i < \delta$, divided by the total number of cells.

This measure has an important advantage over the normal VPF: a higher particle density does not quench the MVPF at higher radii as it does the normal VPF. The higher the mass resolution (more particles, which is usually a good thing), the less likely it will be to find a totally empty sphere. For very high mass resolution simulations this would actually mean that you will stop probing actual voids, but rather start probing the interparticle separation only. The MVPF takes into account the fact that voids are never truly empty; neither in theory (Sheth and van de Weygaert, 2004) nor in observations (Kirshner et al., 1981), as recent findings of void galaxies show (Stanonik et al., 2009a,b).

Sensitivity of the MVPF to DE models

One thing that needs to be determined is the sensitivity of the range of MVPFs as function of δ to the differences in the DE models considered. We did this by simply trying out a range of δ values on all the models and computing the differences. The higher the difference, the higher the sensitivity of that MVPF to the differences between DE models.

The results are shown in figure 4.8. We clearly see that for all model comparisons, the largest differences are obtained when using the $\delta = -0.8$ MVPF. Note that the value of $\delta = -0.8$ is the predicted value for the density of voids from simple spherical models (Icke, 1984; Sheth and van de Weygaert, 2004). The $\text{MVPF}_{-0.8}$ is most sensitive around $R = 1.0 \pm 0.2h^{-1}$ Mpc.

A point of concern is that the differences do not exceed 0.08 and on average lie around 0.03. On a scale of 0 to 1 these are rather small values. We thus need the MVPF to be more stable than the VPF under redshift space transformations to be useful for our purpose.

Results

In figure 4.9 we show the $P_{-0.8}(V)$'s for several simulations. The panels contain the same models at the same positions as in figure 4.7. Left are again the high resolution

³After finishing our development and analysis of the mVPF we found that a similar method had been developed for 2D particle distributions by Ryden and Melott (1996).

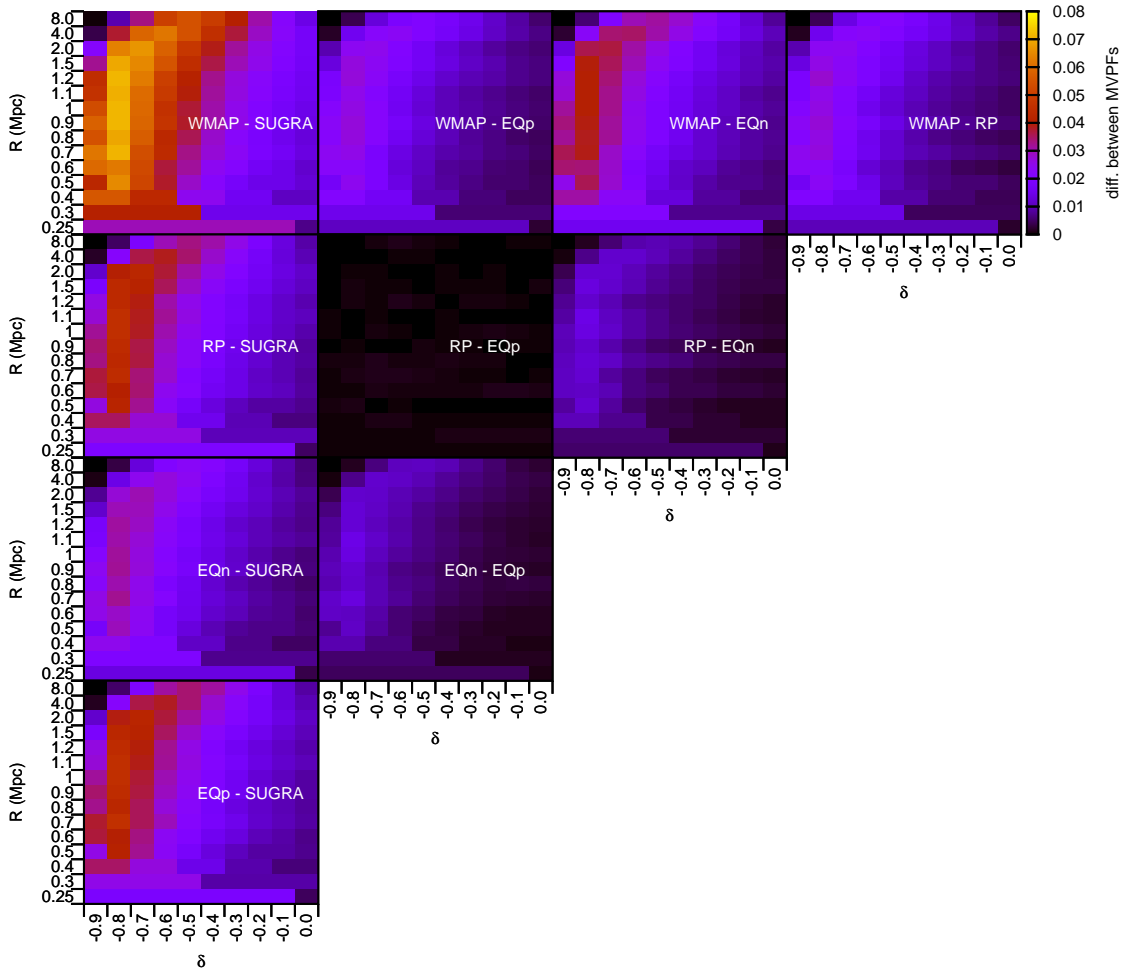


Figure 4.8: Differences in the MVPFs of different DE models. This shows the sensitivity of different MVPF configurations to the differences between DE models. The higher the difference, the higher the sensitivity at that scale.

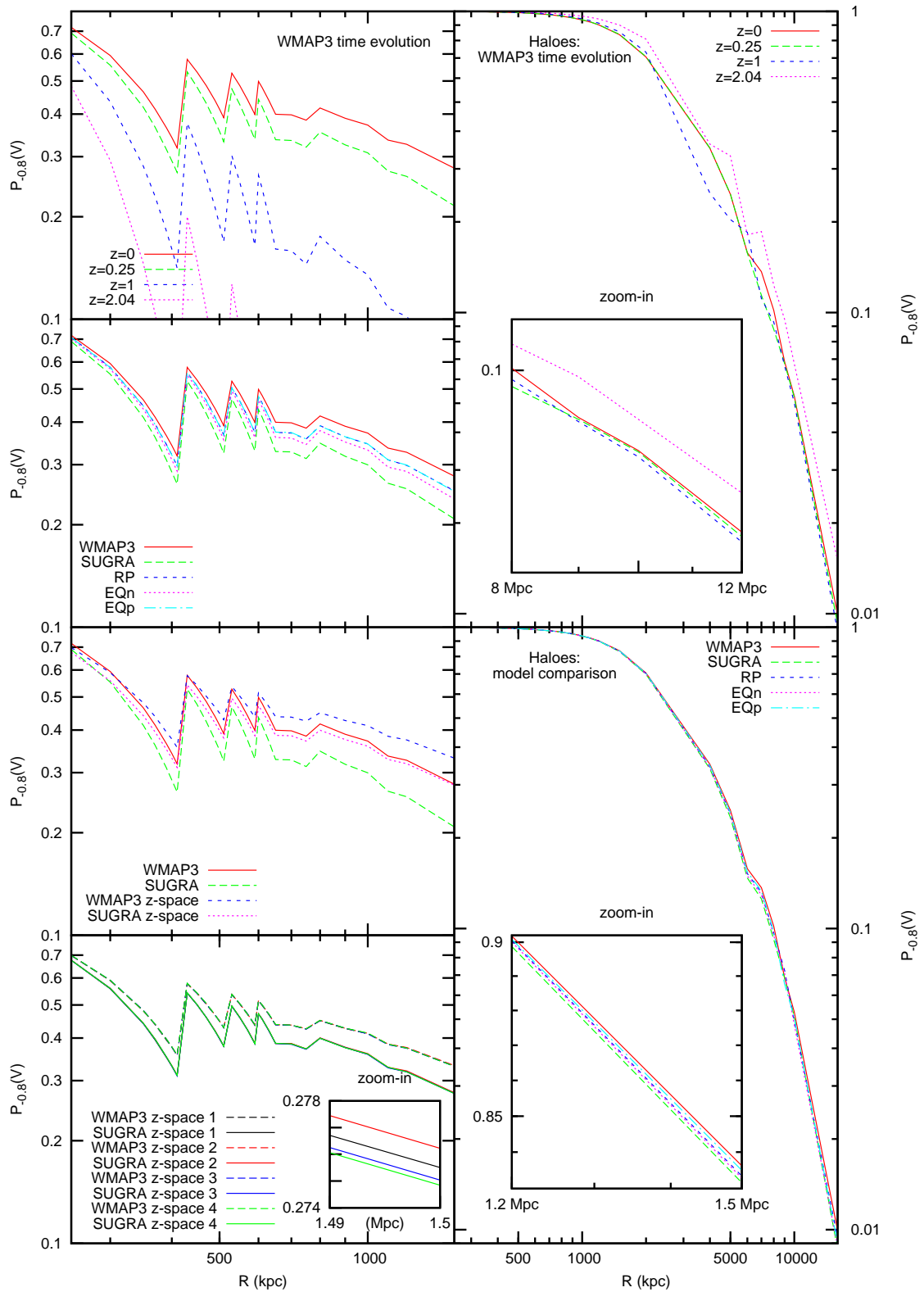


Figure 4.9: Modified void probability functions with $\delta = -0.8$. Again, the left panels show MVPFs of the complete DM particle sets and the right panels show MVPFs for the derived halo distributions.

data results (time evolution, model comparisons and redshift space comparisons) and right we show the results for the halo distribution.

Discreteness effects

The most obvious feature in the left panels is the sawtooth pattern that emerges in all simulations at all redshifts. There are two strong indications that this feature is caused by the mean interparticle distance (MIPD), i.e. the discreteness of the particle distribution. The pattern starts at about the MIPD of $300/768 = 0.39h^{-1}$ Mpc. However, the radius R of a sphere of volume V corresponds to an underdense sphere of diameter $2R$. If the MIPD causes the first sawtooth the MIPD in voids should hence be about $2R = 0.8h^{-1}$ Mpc.

In figure 4.10 we see that indeed this is the case with an MIPD of about $1h^{-1}$ Mpc. The two other peaks are at about $\sqrt{2}(2R)$ and $\sqrt{3}(2R)$, possibly corresponding to the stretched out artefacts of the diagonal distances in respectively the sides and the cubes of the initial condition particle grid cells.

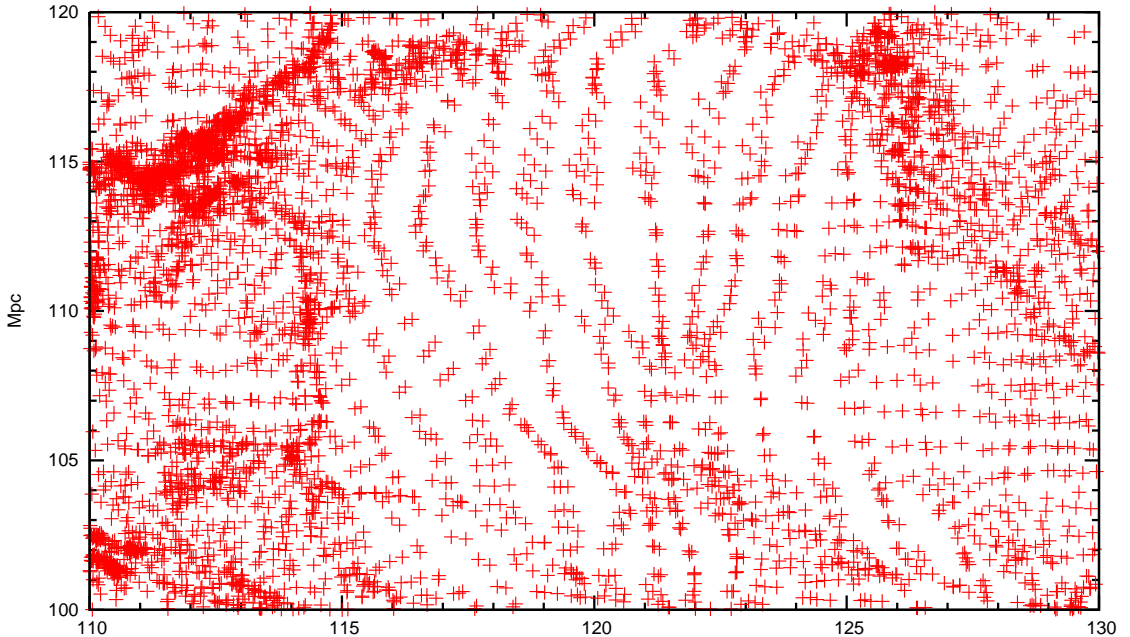


Figure 4.10: Zoom-in of an underdense region in a slice through the particle box in the WMAP3 simulation.

The second indication that the MIPD causes the sawtooth pattern is presented in figure 4.11. The MVPFs of two low resolution simulations are compared to the high resolution one. The sawtooth pattern is shifted by a factor of 3 in radius compared to the high resolution simulation. This corresponds exactly to the factor 3 increase of the MIPD; from $300/768 = 0.39$ to $300/256 = 1.17h^{-1}$ Mpc⁴.

Either we can correct for this pattern using the MIPD in voids (thereby shifting the corrected MVPF down a bit) or by taking the MVPF on a density field instead of on

⁴We see that the high resolution and “low res 3” simulation MVPFs nicely converge at higher radii. This was to be expected; the initial conditions were exactly the same, except for the number of particles. One of the disadvantages of the VPF, its density dependence, is indeed no longer present in the MVPF.

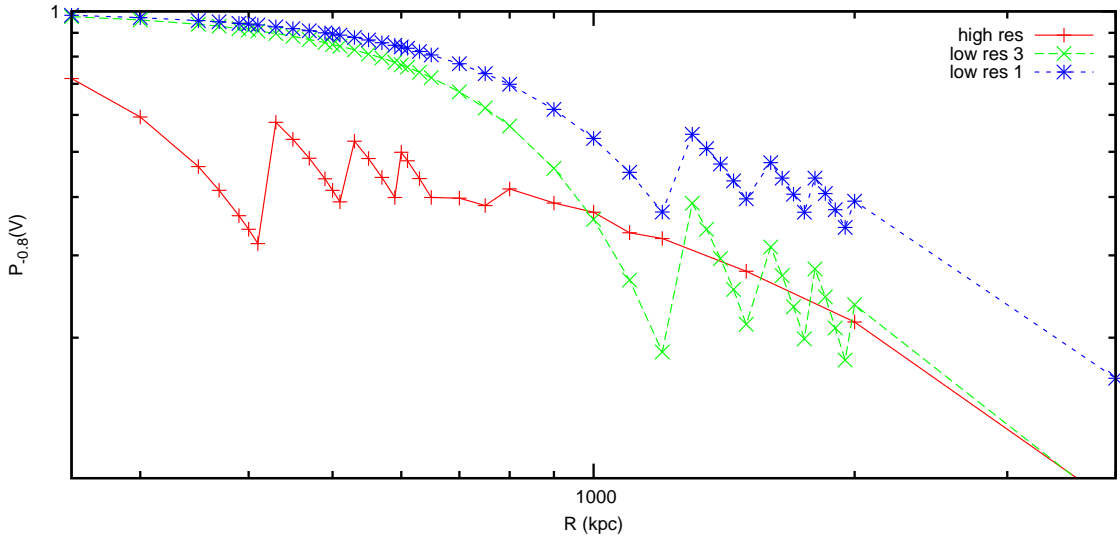


Figure 4.11: Modified void probability functions with $\delta = -0.8$. Comparison of low resolution (256^3 particles) to high resolution (768^3 particles) dataset MVPFs. “Low res 3” is a simulation with the same cosmological input parameters as the high resolution simulation. “Low res 1” uses a different power spectrum.

the particle distribution itself or we must discard the data at and below these scales. Assuming that it is possible to correct (the density method seems especially promising, seeing as the MVPF is defined in terms of δ anyway) we now take a look at what we can actually do with these diagrams.

Discussion

In the left panels of figure 4.9 we see that the MVPF gives us a larger usable range in radii. Whereas the VPF drops off to zero at radii of about $1h^{-1}$ Mpc, the MVPF seems to go on far beyond that. The differences between models and different redshifts are very well measurable. The redshift space panels show us that again the model differences are invariant to redshift space transformations from different locations.

One important difference with the VPF is shown in the bottom left panel. The MVPF is far more stable under different redshift space transformations than the VPF. This must be due to the smaller uncertainties at these radii in the MVPF compared to the VPF (which at those radii starts to become very small). In the zoom-in panel we see that the scatter introduced by different redshift transformations is on the order of 0.002.

The halo panels on the right side of figure 4.9 show us two things. First, the top panel shows us that the uncertainty introduced by the small number of haloes at high redshift causes the MVPF to behave quite irrationally. In the lower panel we see that the MVPFs of different models are still ranked in height in the same order as in the second left panel. The information on different models can still be extracted from the halo distribution using the MVPF.

In the zoom-in box we see that the differences are on the order of 0.005. This would mean that by using the MVPF on halo distributions in redshift space we can at least discard a few models. If the measured MVPF at e.g. $R = 1.5h^{-1}$ Mpc would be lower

than the predicted WMAP3 value by 0.003, then we can be quite sure that the MVPF is not of a SUGRA model, because the scatter that could have been introduced by the redshift transformation can not bring the difference up to the required 0.005. It will, however, be nearly impossible to use the MVPF to actually pinpoint a DE model. The redshift space transformation scatter is still too large and this will ever remain a fundamental observational error⁵.

4.5 Void Morphology Parameters

In this section we investigate void sizes and shapes. This allows us to test the claims of Lee and Park (2009) and Lavaux and Wandelt (2010) on the redshift dependence of mean void ellipticities. The claim is that the average ellipticity $\bar{\epsilon}$ drops as a function of redshift. Moreover, the exact rate of decrease is predicted to depend strongly on the value of w_a , i.e. on the redshift evolution of the equation of state parameter w of dark energy.

Our main aim in this is to explore the possibility of discerning models through their shape parameter distributions. We examine several void morphology parameters as determined by the WVF algorithm (section 3.2). We do this on six different length scales using six different smoothing radii. We can thus compare the sensitivity of different void sizes to the DE models.

4.5.1 Volume and shape distributions

Introduction: definitions and description

In figures 4.12, 4.13 and 4.14 we show estimated void (effective) radii r^6 , ellipticities ϵ , oblatenesses p and prolatenesses q . Given the estimated void ellipse semi-axes $a > b > c$ (see section 3.2) these quantities are defined as:

$$r = \sqrt{abc}, \quad \epsilon = 1 - \frac{c}{a}, \quad p = \frac{b}{a} \quad \text{and} \quad q = \frac{c}{b}. \quad (4.12)$$

The figures show plots of the probability density distributions⁷ $p(x)$ of the shape parameters, i.e. $\int_{-\infty}^{\infty} p(x)dx = 1$ where x is V , ϵ , p or q .

Figure 4.12 shows the probability density distributions of the five different high resolution DE model simulations at $z = 0$. Each column shows a different parameter. The first column contains the distributions of effective radii in $h^{-1}\text{Mpc}$. The other columns show respectively the distributions of ellipticities ϵ , oblatenesses p and prolatenesses q . In the six rows we distinguish between distributions of WVF runs with different Gaussian smoothing radii R_f . We show these distributions at different smoothing scales to compare the sensitivities of different void scales to DE model differences.

In figure 4.13 the same parameters are shown for the redshift space results of the WMAP3 and SUGRA models. In this figure we only show the results at a smoothing radius of $R_f = 1.5h^{-1}\text{Mpc}$. As we discuss below, this is the most sensitive scale to differences in the simulations. The same holds for figure 4.14 where we show the shape parameter distributions at different timesteps in the WMAP3 model simulation.

⁵At least until we invent better ways to determine distances.

⁶The effective radius r equals the radius r_{sph} of a sphere of the same volume as the ellipse, i.e. $V = \frac{4}{3}\pi r_{\text{sph}}^3 = \frac{4}{3}\pi abc = \frac{4}{3}\pi r^3$.

⁷This is why there are no tics on the y-axis; only relative values are relevant.

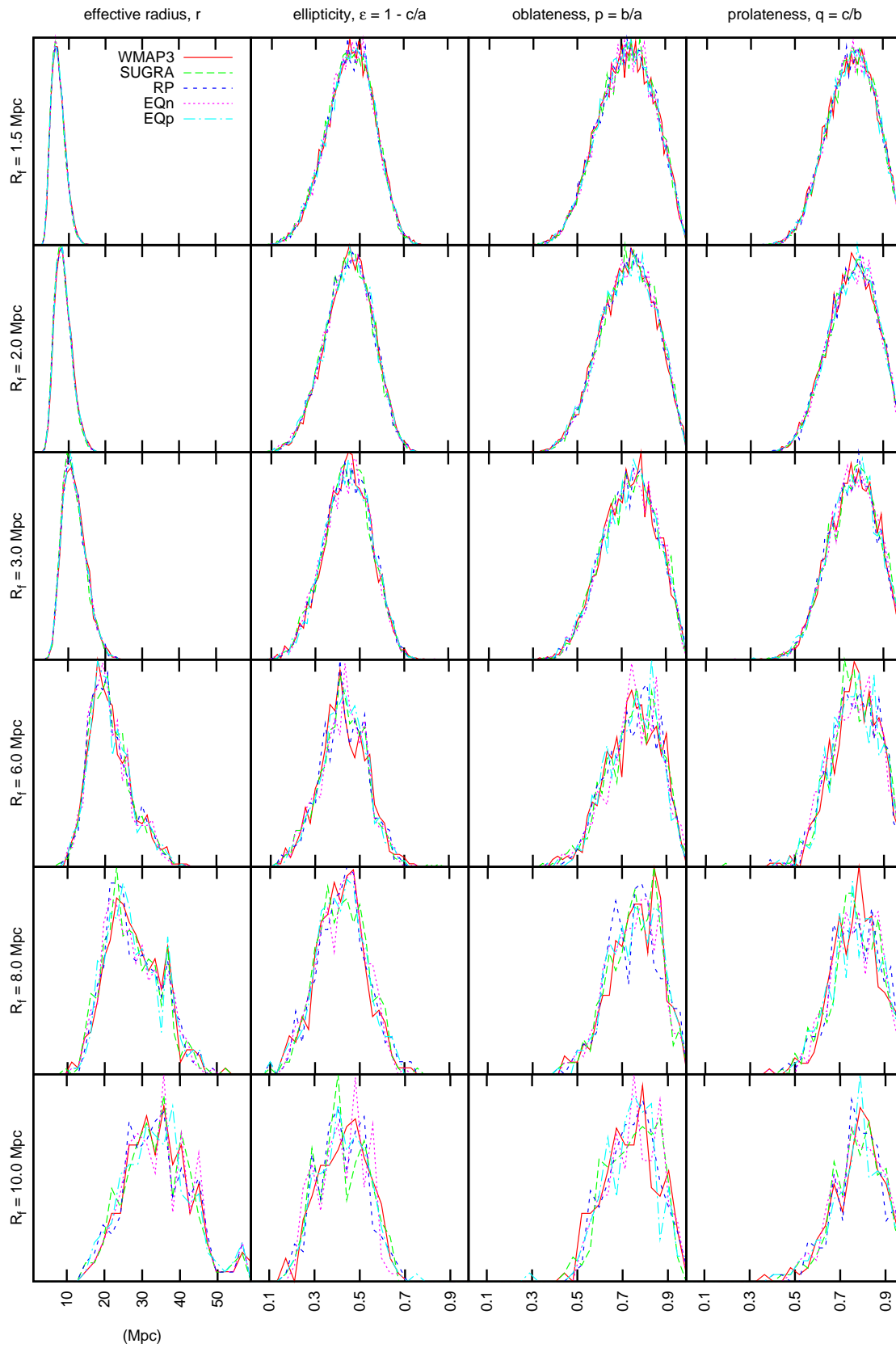


Figure 4.12: Probability density plots of the volume and shape distributions of voids in the different model simulations at $z = 0$. Each column contains a different shape parameter and each row shows the shape parameter distribution of a void population obtained using a different smoothing radius in the WVF.

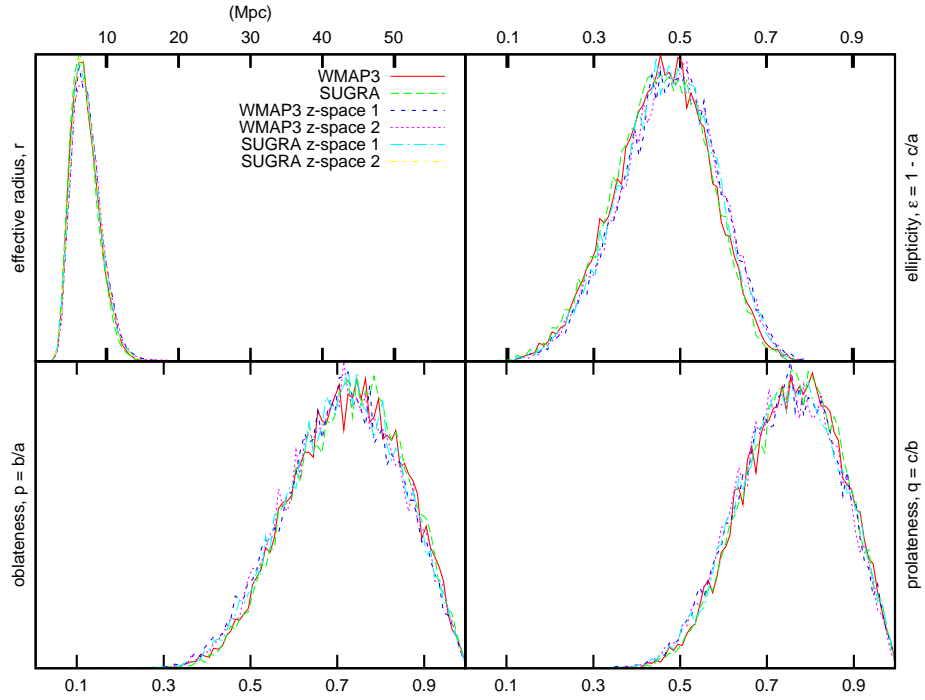


Figure 4.13: Probability density plots of the volume and shape distributions of voids (smoothing radius of $R_f = 1.5h^{-1}$ Mpc) in the WMAP3 and SUGRA simulations and two of their redshift space counterparts, all at $z = 0$.

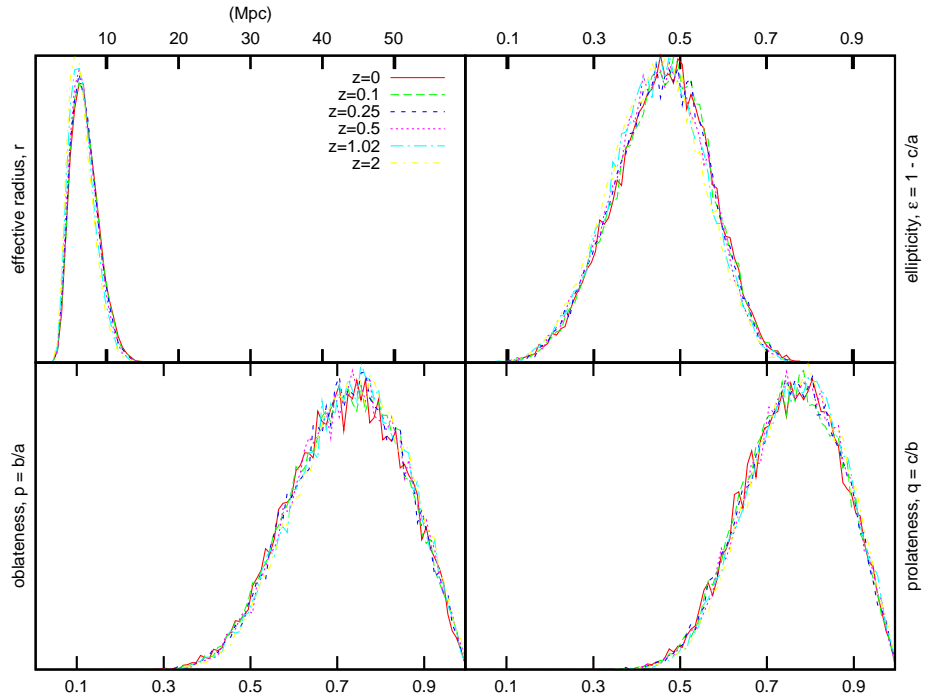


Figure 4.14: Probability density plots of the volume and shape distributions of voids (smoothing radius of $R_f = 1.5h^{-1}$ Mpc) in the WMAP3 simulation at several redshifts.

Discussion

It is evident that for larger smoothing radii, the volume of detected voids rises. This is because the small scale void boundaries will be smoothed out. We can clearly see this effect in figure 4.12. The shape of the volume distribution perfectly matches the predictions of Sheth and van de Weygaert (2004). The locations of the peaks are shifted upwards, which again must be partly due to the smoothing scales and partly to the finite resolution of an N-body simulation as compared to the ‘infinite’ resolution of the theoretical results of Sheth and van de Weygaert (2004).

On the other hand, the effect of the smoothing radius on the shape distributions is surprisingly small. This implies that the void shape distribution is a scale invariant property of void populations. This is an interesting result by itself. It tells us that we can safely ignore the larger scale void distributions and focus on the $R_f = 1.5h^{-1}$ Mpc voids only. These should contain all the information we can get out of the simulations using void shapes, because larger scale distributions will inherently introduce larger errors due to smaller numbers. If the shape distribution is scale invariant then the voids on the smallest scales will always contain more exact information than the larger scales.

An alternative option we shortly looked into was to add together the information on all scales. This did not yield any extra precision or information. This eventually led us to focus on $R_f = 1.5h^{-1}$ Mpc voids. Smoothing radii smaller than this value of $1.5h^{-1}$ Mpc are not feasible. We need some smoothing to filter out the remaining shot noise in the void regions. At smoothing radii below $1.5h^{-1}$ Mpc these will quickly start to play a significant role.

4.5.2 Shape versus redshift

High resolution data

Looking at figures 4.13 and 4.14 we see that again the redshift space transformation introduces a significant amount of scatter. The differences in the panels of figure 4.13 seem larger than those in figure 4.14. According to Lee and Park (2009) we can discern DE models by looking at the time evolution of the mean ellipticity $\bar{\epsilon}$. This should drop as a function of redshift. If we look very carefully at the ellipticity panel of figure 4.14 we can indeed see a slight downward evolution of the ellipticity with redshift. In figure 4.15 we see that given a high resolution map of the mass distribution we can indeed reproduce the general trend of Lee and Park (2009) (cf. figure 4.16).

<i>Simulation</i>	WMAP3			SUGRA		
<i>Space</i>	real	z-space 1	z-space 2	real	z-space 1	z-space 2
$\bar{\epsilon}$	0.45837	0.47323	0.47190	0.45447	0.46791	0.46606

Table 4.1: Mean ellipticities of real and redshift space voids. Full distributions are plotted in figure 4.13. The “z-spaces” again represent two observers at different positions, giving different redshift spaces.

The question remains, though, whether the amount of scatter in figure 4.13 is of comparable size to the amount of decrease of $\bar{\epsilon}$ with time. The mean ellipticities in this plot are given in table 4.1. The difference between DE models again seems rather stable under the redshift space transformation, but there is some scatter in the precise

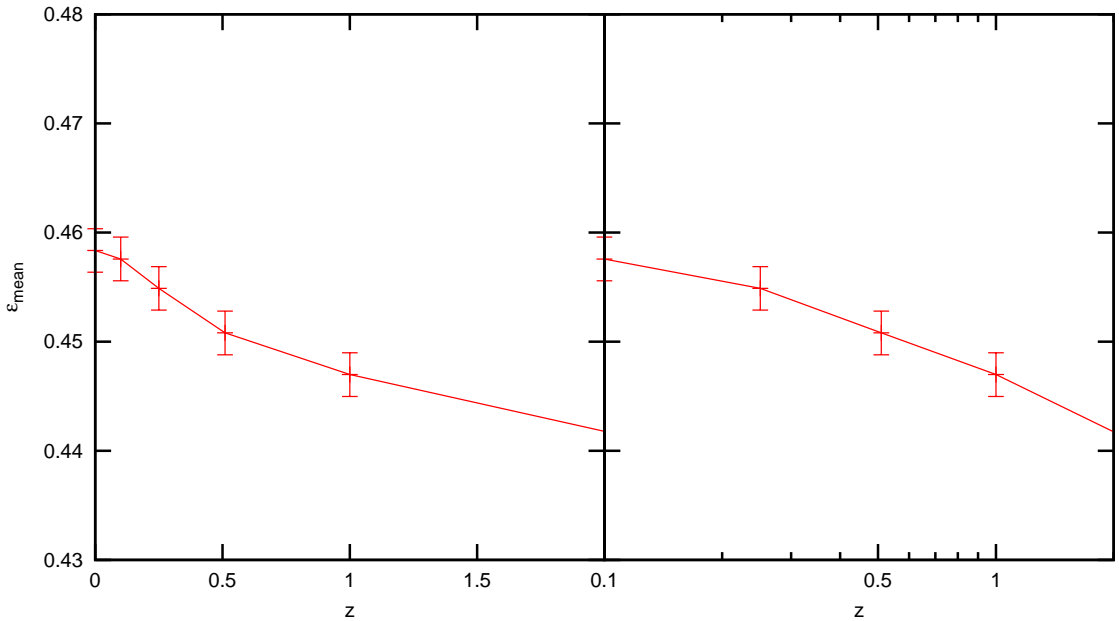


Figure 4.15: Mean ellipticity versus redshift for the high resolution WMAP3 model. Errorbars show the possible scatter caused by redshift distortions.

outcome of $\bar{\epsilon}$. We can expect redshift space errors in the mean ellipticity on the order of 0.002 based on these numbers. We took this error into account in the errorbars of figure 4.15. We thus find that the trend persists after taking redshift space transformation uncertainties into account. The slope of Lee and Park (2009) is steeper, but overall the results are consistent with our high resolution DM simulations.

Halo

We have also tested the claims of Lee and Park (2009) and Lavaux and Wandelt (2010) on our halo samples⁸, but were unable to detect the decrease in ellipticity. Rather, the distribution of halo void ellipticities stays remarkably constant, up to at least $z = 1$, and rises steeply at higher redshifts (see figure 4.17). The latter may be caused by the decreasing number of haloes with higher redshift (and therefore poorer probing of the full density field). Seeing as the ellipticity distributions of different models are predicted to be the same at $z = 0$, which is indeed what we see, it seems that it is impossible to discriminate different DE models on the basis of these approximated void shape parameters.

The discrepancy between the “halo voids” and the “high-resolution DM simulation voids” must be caused by either the halo sample itself, i.e. by the number of haloes (which is significantly lower than the number of DM particles) or its spatial distribution, or by the incapability of the combination of DTFE and WVF to deal with halo distributions. We investigate the former possibility below⁹.

⁸The haloes were weighted by their mass. The DTFE algorithm incorporates these masses in its determination of the density field. Later on we also use the unweighted halo distribution to probe only the morphology of the distribution.

⁹The influence of other void finders is also being investigated. Communication is ongoing with the people involved with other void finders like ZOBOV (Neyrinck, 2008) and the void finder by Hoyle and

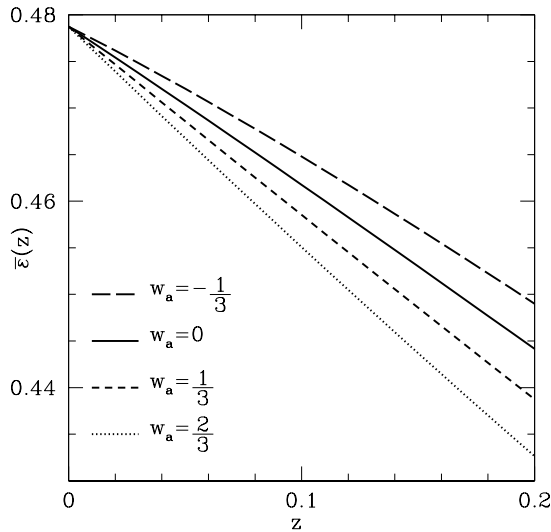


Figure 4.16: Theoretical mean ellipticities versus redshift for several values of w_a . Image from Lee and Park (2009).

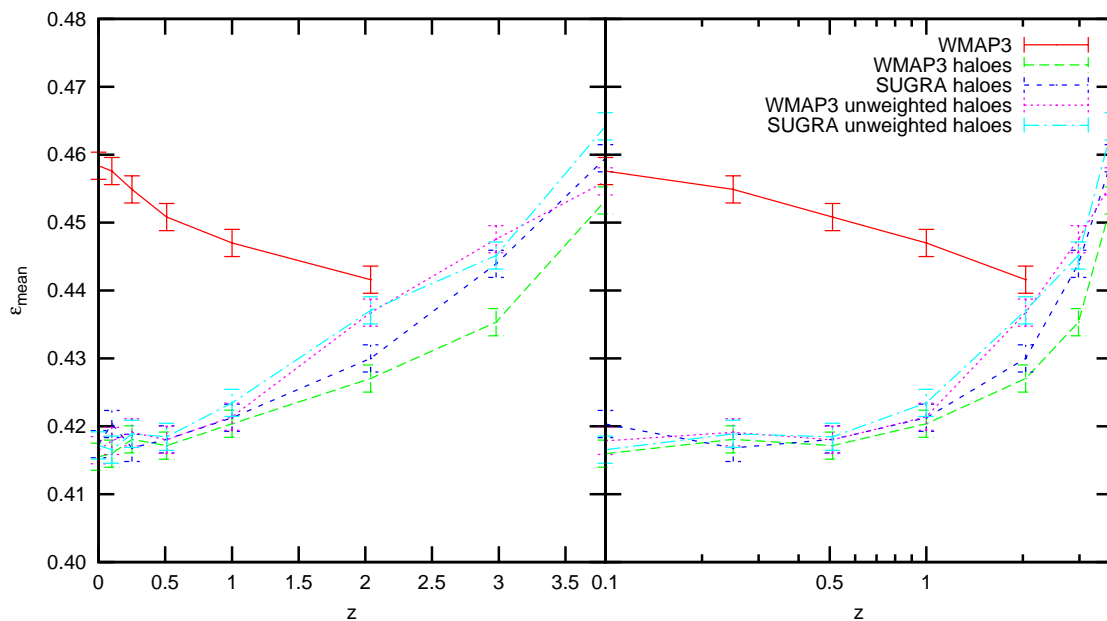


Figure 4.17: Mean ellipticities versus redshift for the halo distributions of the WMAP3 and SUGRA simulations. For the plain ‘haloes’ plots the individual halo masses were taken into account in the calculation of the density field. The ‘unweighted haloes’ plots did not take halo masses into account and thus represent only the spatial distribution of the haloes.

Within the “DTFE plus WVF framework” we can compare the halo distribution to a random subset of the full DM particle distribution with the same number of particles as the halo set. If these “subset voids” have a shape-redshift dependence similar to that of the halo voids then it is plausible that indeed the number of halo particles is too low. If they still differ, then the spatial distribution of haloes (or the DTFE/WVF method) must be to blame.

We thus took three random subsets of the high-res DM data, with at each redshift the same number of particles as there were identified haloes in our halo datasets. We determined the maximum, minimum and median at every redshift and plotted all of these to also get an impression of the spread caused by low particle numbers. In figure 4.18 we can see that indeed the subset voids seem to correspond well to the halo voids, implying that a main cause of the deviation of halo void shapes from high-resolution void shapes is the sparsity of haloes. In the $R_f = 3h^{-1}$ Mpc panels, we see a significant difference between the two halo void ellipticity lines and the subset void ellipticity lines. This may well indicate that also the spatial distribution of haloes plays a role.

As a final test we measured the void shape distribution in an unweighted halo density field, i.e. in a density field where only the halo positions have been used and the halo masses were all set to equal values. We did this test, because for the random subset densities we also had equal particle masses, so by comparing to unweighted halo density field voids we only compare unbiased spatial distributions of the particles. These “unweighted halo voids” indeed differ slightly more from the subset voids than the “weighted halo voids” (see figure 4.17). This leads us to conclude that the spatial distribution of haloes indeed also plays a role.

From this we can conclude that haloes¹⁰ are definitely unsuited for the purpose of discerning DE models. We found that there are at least two reasons for this: one having to do with the number density of the halo sample and the other being a biasing problem.

The number density of the halo distribution is too low to probe the voids in the underlying matter density. This poses a significant problem. Our halo density is about $0.019h^3\text{Mpc}^{-3}$. The SDSS DR6 luminosity function fits (Montero-Dorta and Prada, 2009) give densities of the same order of magnitude, although volume limited samples will have even lower densities. Given these similar values, it will not be possible to measure any signal of DE in current observations. This makes the application of our statistics to real data useless. Significantly more data would be needed to circumvent this problem.

The second reason for haloes being a poor probe of the underlying density field seems to be their spatial distribution. This may be the most important finding of this thesis. It might implicate that no matter how many haloes, or galaxies, you would observe, their spatial distribution simply does not probe the underlying mass distribution sufficiently well for void shape statistics to be usable for discriminating between models of DE. We will further discuss this biasing problem in section 5.

Ellipticity versus redshift: a probe of the nature of dark energy?

The last question we wish to address, is whether different DE models differ in a $\bar{\epsilon}$ versus redshift plot at all. Seeing as we had only $z = 0$ data for the high resolution simulations,

Vogeley (2002).

¹⁰Or at least those found by the SUBFIND halo finder.

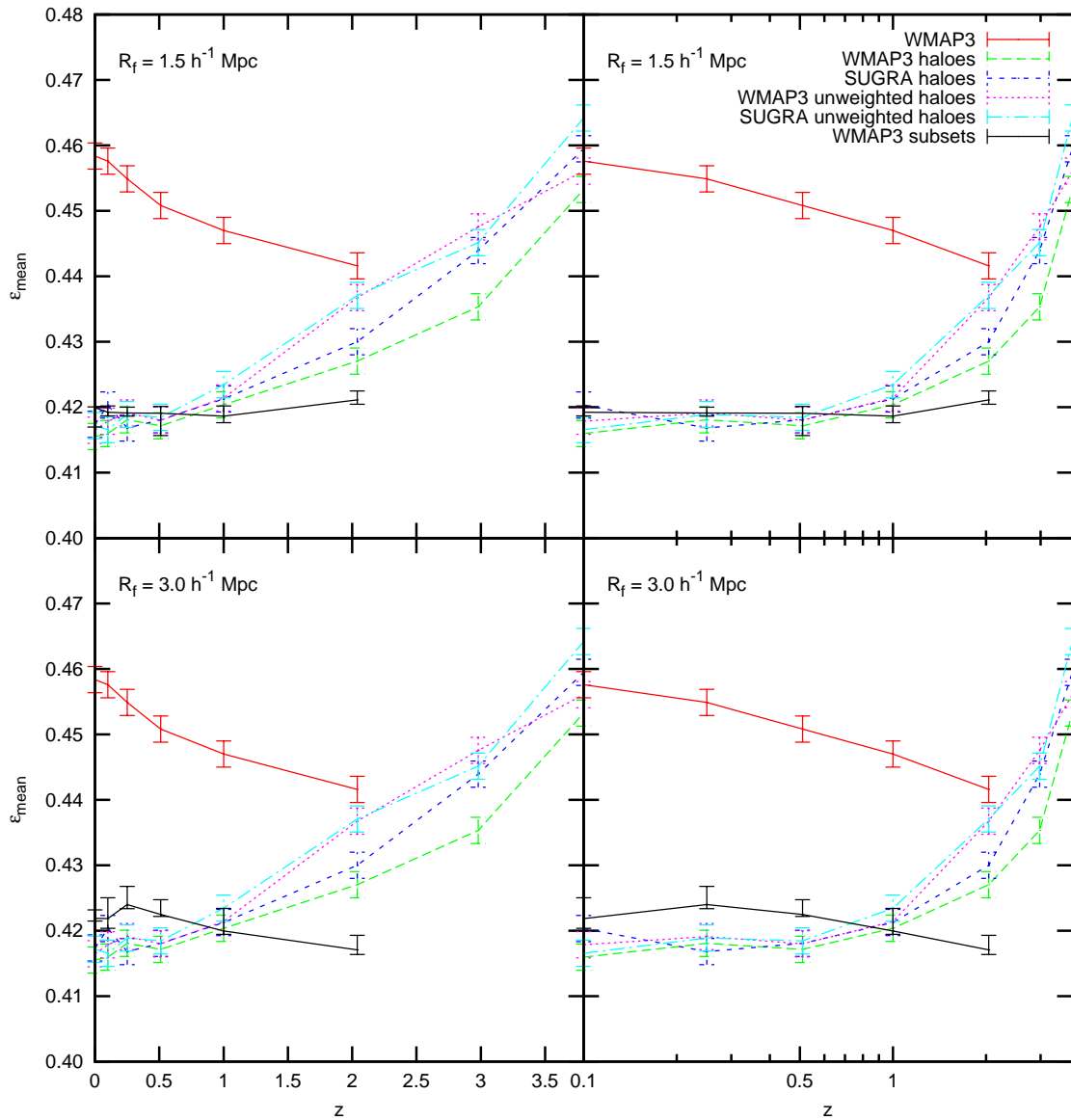


Figure 4.18: The same plots as in figure 4.17, with the addition of the mean ellipticity versus redshift of the WMAP3 random subsets. Also, in this case, the $R_f = 3.0 h^{-1} \text{ Mpc}$ results are shown.

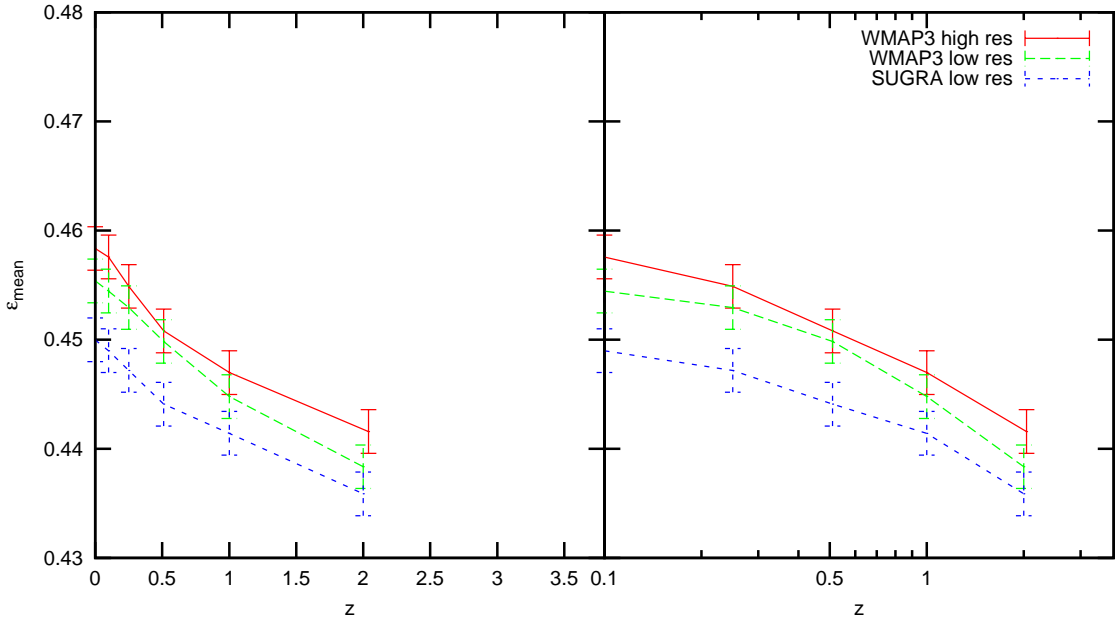


Figure 4.19: Mean ellipticities versus redshift for the low resolution simulations of WMAP3 and SUGRA models. Errorbars again represent redshift distortions.

we used two of our own low resolution simulations of WMAP3 and SUGRA DE models. The result is shown in figure 4.19. This figure seems to suggest that the theoretical results of Lee and Park (2009) and Lavaux and Wandelt (2010) may indeed be real. The SUGRA model, which fits to $w_a = 0.452$ (table 2.1), runs below the WMAP3 model which has $w_a = 0$, just like in figure 4.16. The differences are also of the same order of magnitude.

There are some inconsistencies. For one, the SUGRA model does not start at the same value as the WMAP3 model. Also, in figure 4.16 the lines diverge, whereas in figure 4.19 they first run parallel and later converge.

These facts suggest that some detail may be missing from this analysis. We have looked into two possible causes of the observed inconsistencies.

First we briefly investigated whether overdense regions in detected voids may cause any problems. Strictly speaking we should not count these as part of the void, especially overdense regions on the void borders. As explained by van de Weygaert and Platen (2009, §3.2.1), only the inner parts of the void are properly described by the homogeneous ellipsoidal model¹¹. Yet, the WVF algorithm counts all density field cells as voids, excepting only the border cells where voids meet. We have therefore tried discarding all overdense void cells.

In figure 4.20 we show the result of this procedure. About 14% of the volume in voids is eliminated in this way. The shape analysis based on these voids does indeed yield slightly different results, e.g. the mean ellipticities are slightly higher. Still, we do not find the strong redshift dependence found by Lee and Park (2009) and Lavaux and Wandelt (2010). It seems then that this is not the cause of the observed inconsistencies.

Secondly, we looked into the possibility that the differences between the model el-

¹¹Because the “role of surrounding material [will dominate], through the sweeping up of matter and the encounter with neighbouring features.”

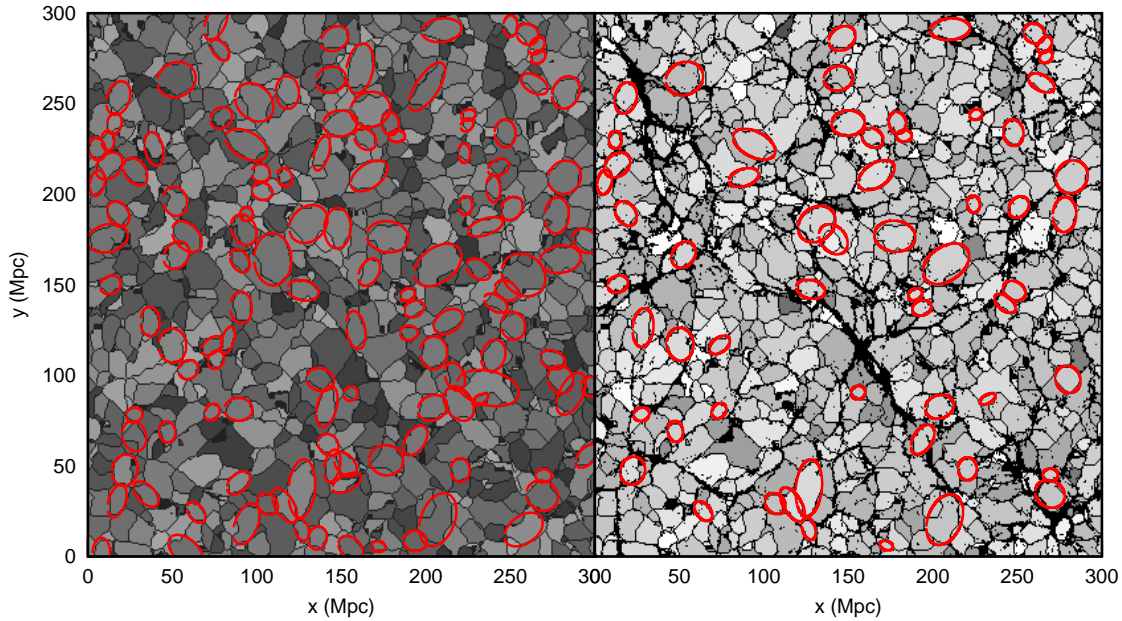


Figure 4.20: Comparison of the standard WVF void distribution in our WMAP3 $z = 0$ box to the WVF voids minus overdense regions (as described in the text).

lipticities are not primarily caused by different $w(z)$, but by some other cosmological parameter. We found a very interesting dependence on the amount of clustering. As we briefly mentioned in section 2.2.1, the different DE models have different values of σ_8 . This was necessary for proper normalisation at the CMB. In figure 4.21 we see that for both models there is a clear relation between σ_8 and the mean ellipticity. In fact, the underlying relation seems to be the same, as the lines overlap. The relation seems independent of redshift. Both lines consist of σ_8 measurements at redshifts of 0, 0.1, 0.25, 0.51, 1.0 and 2.04. Were they redshift dependent we should have been able to distinguish e.g. the point at the middle of the SUGRA line (which corresponds to $z \approx 0.5$) from the point at the same location of the WMAP3 line (which corresponds to $z \approx 1$). This strong correlation is especially surprising when we realize that the WMAP3 and SUGRA models differ the most in every other aspect we investigated.

It seems then that the main cause of the differences between these models is in fact σ_8 . Of course, in this case, the difference in DE models is the underlying cause of this difference through $D(z)$ in equation 2.9. Despite this fact, we have found nothing that can distinguish the specific influence on $D(z)$ of different DE models from other possible influences on σ_8 . This means that we can not use the mean ellipticity evolution to distinguish a Λ CDM (or other) model with a certain $\sigma_8(z)$ from a quintessence model with the same $\sigma_8(z)$. Because several cosmological parameters enter into this dependence through $D(z)$ (see equation 2.7), we can conclude that the probe of $\bar{\epsilon}$ is degenerate in $w(z)$ and all these other parameters.

We can thus conclude that it is not at all fully evident that the relation between $\bar{\epsilon}$ and redshift can unequivocally discern between different DE models. Neither in “real” data (haloes) nor in higher resolution simulated data can we properly reproduce the theoretical results from Lee and Park (2009) and Lavaux and Wandelt (2010). A clear dependence of mean ellipticity on the amount of clustering was found. This implies that

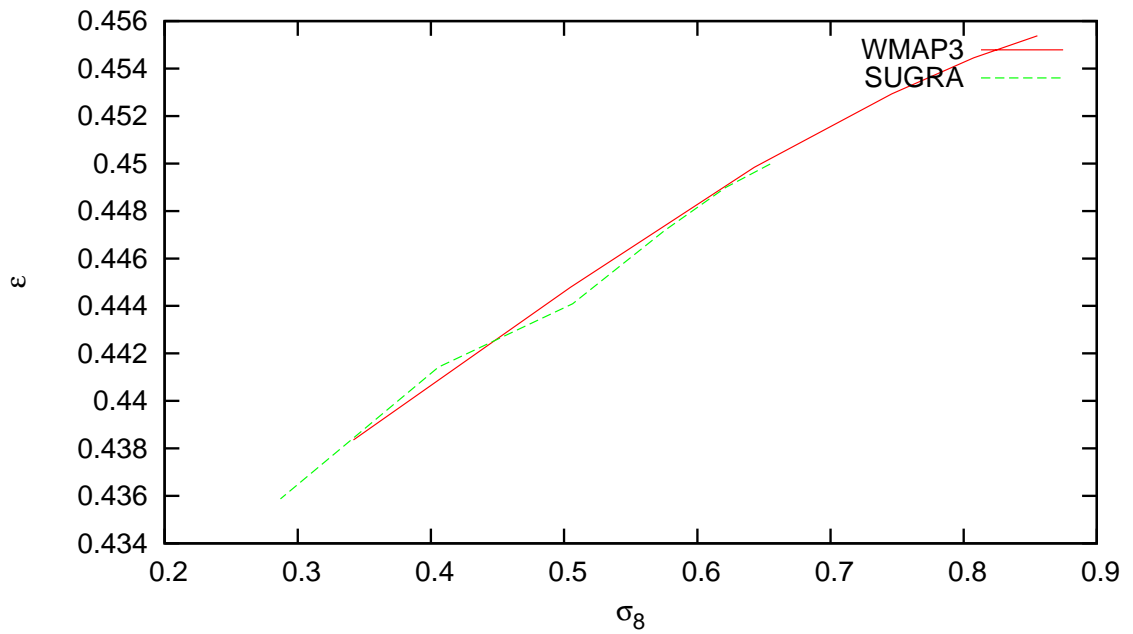


Figure 4.21: Mean ellipticities versus σ_8 for the low resolution simulations of WMAP3 and SUGRA models. The lines consist of σ_8 values of the two simulations at redshifts 0, 0.1, 0.25, 0.51, 1.0 and 2.04.

the only way to measure differences between DE models is through the differences in σ_8 . This makes a potential DE measurement degenerate with measurements of σ_8 itself.

In this section we will discuss the main question of this thesis: *can voids be used (in real observations) to probe the nature of dark energy?* To answer this question we have obtained and examined several measures of void properties. How did these measures perform as probes of dark energy? What difficulties were encountered in the transition to redshift space and halo data (and, implicitly, voids in observed galaxy distributions)? What does the possible degeneracy with σ_8 mean for these probes? And finally, what future possibilities are there? This with respect to these probes specifically as well as for the idea of voids as probes of dark energy in general? These are the leading questions that we will try to address in this chapter.

We will start by summarizing our main results on the possible probes we tested. From this we conclude that it seems unlikely that we will be able to use these probes (in their current form) on observations. Following that we will discuss the general problem of the σ_8 degeneracy. At the end of this section we will discuss the remaining open questions and provide some avenues for further research.

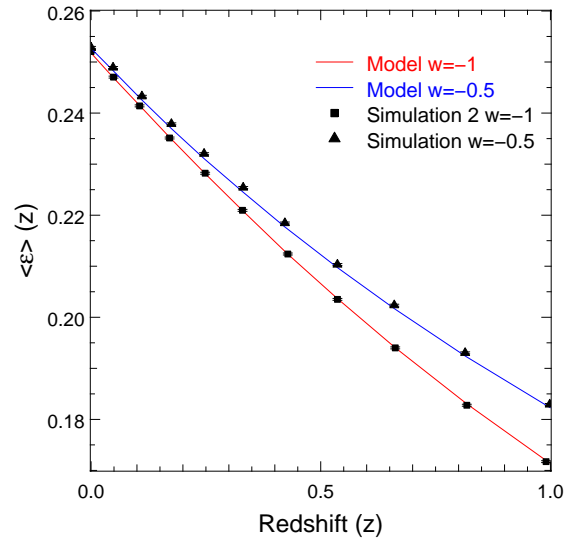
5.1 Results from our probes

5.1.1 Summary

Early on in our analysis, our suspicions were raised that our task of probing dark energy would not be an easy one. The analysis of the one-point pdfs suggested that redshift space distortions would have a great impact on any signal we would have liked to probe. From the two-point correlation functions we learned that it seemed hard to distinguish one of our models of time dependent DE from the earlier timesteps in the WMAP3 simulation. There were no clear distinguishing features in either of these statistics. It seemed that the viability for discerning models in real data would prove difficult. The analysis of void statistics proved to yield ambiguous results as well.

The results of our analyses were not as clear-cut as those of related studies (Lee and Park, 2009; Lavaux and Wandelt, 2010). We could qualitatively reproduce some of their claims in high resolution data sets. This was contrasted with the problems that arise when the effects of redshift distortion are included. Moreover, any measurable signal gets obscured when the halo distribution is probed. With the latter forming a realistic

Figure 5.1: Differences in the mean ellipticity evolution between models with $w = -1$ and $w = -0.5$. Both the results from theory (the red and blue lines) and the results from the corresponding N-body simulations (triangles and squares) are shown. Figure from Lavaux and Wandelt (2010).



representation of a galaxy distribution, in practice, these effects render unfeasible any attempts at the actual use of the measurement of void shapes as probes of dark energy.

These results from simulated observations give little hope for our probes of dark energy. The practical problems of redshift distortions and the sparsity and complex biasing of the galaxy distribution are significant. Even though most measures had some merit in simulations of the full dark matter distribution, when dealing with galaxies in redshift surveys, the chances of detecting a signal of the nature of dark energy are slim to nothing.

5.1.2 Theory: results from N-body simulations

Our project was largely based on the claims of Park and Lee (2007) and Lavaux and Wandelt (2010). The mean ellipticity of voids as a function of redshift $\bar{e}(z)$ was expected to be a sensitive probe of the dark energy equation of state parameter $w(z)$. We tested this claim on several simulations of the dark matter distribution. In each simulation a different model for dark energy was used. Five different models were thus compared: the Λ CDM model and four models of dark energy as a time-dependent scalar field.

The results from these probes of the *full dark matter distribution* seemed promising at first. Using the approximated ellipsoidal void shapes, we indeed detected the predicted decrease with redshift of the mean ellipticity (figure 4.15). Using our 256^3 particle simulations, we could further show that there was a detectable difference in the void shape evolution of different models of dark energy (figure 4.19).

However, there were some differences with the theoretical results of Lee and Park (2009) and Lavaux and Wandelt (2010). Lavaux and Wandelt (2010) were able to approach the theoretical results very accurately with their simulations (see figure 5.1). In our case the ellipticities at $z = 0$ differed significantly for the different models. In Lee and Park (2009) the ellipticities at $z = 0$ are equal and in Lavaux and Wandelt (2010) they differ only very little if they differ at all¹. Also, the \bar{e} versus z lines diverge at higher redshifts in Lee and Park (2009) and Lavaux and Wandelt (2010). In our case they run more or less parallel; if any divergence is present it is not significant.

¹We can not really tell from the figure because of the overlapping datapoints at $z = 0$

At this point we started to suspect that these discrepancies were caused by some other different parameter in the simulations than $w(z)$. It turned out that $\bar{\epsilon}$ correlated very strongly with σ_8 (figure 4.21). In fact, this relation seemed independent of redshift and DE-model. We obtain a very tight straight line from the σ_8 values of several timesteps in the two simulations that differ the most in terms of $w(z)$, namely the WMAP3 and SUGRA models. This implies that the differences we measured in the mean ellipticities are only dependent on redshift because σ_8 differs at different redshifts. In other words: the mean ellipticity seems dependent on σ_8 rather than on redshift.

Of course the values of σ_8 differ because of the different models of dark energy. σ_8 was normalized at the CMB and because of the dependence of the linear growth factor on $w(z)$ we gained different values of σ_8 . However, the model of dark energy is not the only parameter that influences σ_8 . This means that the measurement of mean ellipticity does not uniquely probe the model of dark energy. It is a measurement that is degenerate in all the parameters that determine σ_8 at different redshifts, i.e. all the parameters that are contained in $D(z)$, the linear growth factor. This means that the mean ellipticity probes the linear growth factor as a function of redshift.

The other probes of the full DM particle distributions can be explained similarly. Throughout our analyses we saw that any difference between models strongly resembled the differences between the different timesteps of the WMAP3 simulation. There were no clear distinguishing features in any of the tests, other than the apparent amount of structure formation. To summarize some examples:

- In the qualitative comparison of models in figures 2.5 and 2.6 we concluded that the main differences were in the amount of structure formation.
- From the halo data in table 3.1 we concluded the same thing.
- Both the one-point pdfs (figure 4.4) and the two-point correlation functions (figures 4.5 and 4.6) showed us no clearly distinguishable features (again, other than the fact that the different model realizations at $z = 0$ are similar to higher redshift results of the WMAP3 simulation).
- The same conclusions were reached for the (modified) void probability functions in the upper two left panels of figures 4.7 and 4.9.

We can conclude that according to our results, mean ellipticities can probe the cosmological model. However, they only probe the model in its totality as represented by σ_8 through $D(z)$. It can not distinguish between the effects of the specific parameters on which $D(z)$ depends, of which $w(z)$ is only one example. It might be possible that by combining $\bar{\epsilon}(z)$ measurements with additional independent constraints we may be able to bring down the errors on the estimated values of cosmological parameters. This may be an interesting topic for further study. However, as we will discuss next, there are other complications that may complicate the practical execution of these measurements.

5.1.3 Practice: results from (simulated) observations

The ultimate goal of our project was to test whether our probes can be used in real observations. This meant that we needed to account for the fact that real data use redshift as a distance estimator. We needed to transform the positions and velocities of particles

in our simulations to redshift space. This transformation causes distortions like the “fingers of god” and the stretching out of voids in the radial direction. Different positions of the observer will cause different distortions. This is due to the different directions of the particle velocities. These cause the magnitudes of a particle’s velocity to be dependent on the observer’s location. The possible range of differences in redshift space distortions for different observers cause a systematic uncertainty in our measurements that we need to take into account when searching for signals of dark energy.

The redshift space distortion turned out to be a significant source of uncertainty in all our tests. Due to this, the one-point pdf was rendered useless to discriminate between cosmological models (left panel of figure 4.4). The VPF could only be used at small radii (bottom left panel of figure 4.7). The modified VPF, which we developed for the purpose of overcoming this and other VPF shortcomings, had relatively little redshift space scatter (bottom left panel of figure 4.9)².

Another complication when dealing with real observations is the fact that we cannot (yet) directly observe the full matter distribution. Our direct source of data is the galaxy distribution. The complication in using galaxies to probe the dark matter distribution is the long standing problem of *biasing* (Kaiser, 1987; Tegmark and Peebles, 1998); while the galaxy distribution reflects the underlying matter distribution, the relation is not necessarily one-to-one. This problem has been recognized to affect voids as well; the comparison of voids defined by galaxies to voids defined by the full dark matter distribution is not straightforward when the biasing is complex (Platen, 2009; Arbabi-Bidgoli and Müller, 2002; Furlanetto and Piran, 2006). Furthermore, the use of a halo sample may introduce discreteness effects. This would be due to the low number of particles compared to a full DM particle distribution.

To assess these two effects, we investigated the halo distribution in our simulations and implicitly assumed this to be representative of the galaxy distribution. This resulted in the total disqualification of the VPF, significantly decreased the use of the MVPF and fully obscured the mean ellipticity versus redshift relation.

The differences in the VPFs of different models that were present in the full DM distributions were still present in the halo distributions, but they became immeasurably small and thus insignificant. The redshift distortion is dominant by far over the differences between models in the VPFs. The results were not as dramatic for the MVPF, though still it seems unlikely that it will yield measurable differences. The redshift distortion is of the same order of magnitude as the differences between MVPFs of different models. This means that the MVPF may still be useful to exclude wildly exotic models. Whether we will specifically need the MVPF, instead of other measures, to exclude such a model may be doubtful.

The MVPF is close to being useful as a probe in real observations. Because of this fact, it may prove prudent to put some final effort into trying to improve it. One possibility that was mentioned earlier is to sample the MVPF from a density field. This will likely remove the sawtooth pattern caused by the discreteness of the particle distribution³. It may be that information will be lost and its use will decline further. It may equally well be that the MVPF sensitivity to DE models peaks at the scales currently confused by the discreteness effects. It would be easy to implement this modification

²The void shape relations were not tested in redshift space. The shape distributions are expected to be stable under redshift space transformations (Hoyle and Vogeley, 2002).

³Note that this may also be a simulation artefact.

and we will therefore pursue this further improvement.

The void shape distribution relations seemed to disappear completely in the halo distributions. We found that this was partly due the number of haloes and partly to their spatial distribution. We first tested the influence of the number density by taking random subsamples of the full simulation with an equal amount of particles as there were haloes in the halo sample. This gave results similar to the halo results, but with a small yet marked deviation. This implies that also the spatial distribution of haloes may have an impact on the shape measurements. It seems then that we have here an example of the above mentioned complexity of biasing which is affecting void measurements. Two separate effects thus play a role here: the sparsity of the halo sample and the intrinsic biasing problem.

5.2 The σ_8 degeneracy problem

We will shortly elaborate on the problem with σ_8 we discovered. The main issue is that the relation we found seems to have gone unnoticed in the literature thus far. Our hypothesis in this discussion is that the relation is in fact real and we will show that there are examples of it to be found in the literature.

We suspect that Lavaux and Wandelt (2010) and Lee and Park (2009) normalize their value of σ_8 at $z = 0$. This does not become fully clear from the texts, but they do not mention otherwise. Also, if they had normalized σ_8 at the CMB, like we did, their value of σ_8 for the $w = -0.5$ model would be far lower. It would be even smaller than that of our SUGRA model. The SUGRA model has a lower (more negative) average value of w than -0.5 , as can be seen in figure 2.1. A higher (less negative) value of w means a lower value of σ_8 (this can be seen by combining equations 2.9, 2.7 and 1.13).

This means that their values of σ_8 at the CMB must differ for the different models of dark energy they test. If their σ_8 's are equal at $z = 0$, then they will differ at later redshifts through the equation of the linear extrapolation of σ_8 to higher redshifts. Lavaux and Wandelt (2010) themselves mention this equation:

$$\sigma_8(z) = \sigma(z = 0) \times \frac{D(z)}{D(z = 0)}. \quad (5.1)$$

They use this relation only to insert $\sigma_8(z)$ in the model of the redshift evolution of the ellipticity (equation 1.32).

According to our results, this is in fact the only cause of the redshift dependence of the ellipticity. In fact, if they have normalized σ_8 at $z = 0$ we can now explain why the ellipticity evolution of different models starts at the exact same ellipticity in both Lavaux and Wandelt (2010) and Lee and Park (2009). Under our hypothesis, this is simply because the σ_8 's are equal.

The fact that their relations diverge, while ours run parallel, can also be understood. The divergence can be explained by the differences in the growth factor for different values of w , combined with the boundary condition of the σ_8 's starting at the same value at $z = 0$. The lack of divergence (starting from $z = 0$) in our case is then caused by the lack of this boundary condition at $z = 0$. We would, however, expect a divergence of the lines at z_{CMB} , because that is where we have set σ_8 to be equal.

Another piece of evidence that our hypothesis is correct is given by Lavaux and Wandelt (2010). They do a small test with two different simulated realizations with the

same cosmological parameters. They find that the two realizations differ slightly in $\bar{\epsilon}$ versus z . They note that the realizations also differ slightly in σ_8 , which thus confirms our hypothesis⁴.

5.3 Open questions

Several open questions remain. Two of the most outstanding ones we present here. First, we shortly elaborate on the possible influence of void finding algorithms. In addition, we forward an interesting observation can be made regarding the extended quintessence models.

Void finders

We argued that the main cause of the inconsistencies between our results and those of Lee and Park (2009) and Lavaux and Wandelt (2010) is in the value of σ_8 . There is, however, one further distinction between our analysis and theirs. The void finding algorithms and even the algorithms used to determine shapes are all different ones.

Park and Lee (2007) determine void shapes by calculating an inertia tensor on the basis of the positions of haloes in the voids. To determine which voids the haloes belong to, they use the void finder of Hoyle and Vogeley (2002) (abbreviated by HV02) which is also based on halo positions. The assumption of Park and Lee (2007) is that the shape of the halo distribution properly probes the underlying void shapes. However, we have shown that this is not the case. Rather, a significant amount of information is lost in the transition of a full dark matter distribution to a halo distribution. Our halo results do not at all match the results from Lee and Park (2009), whereas the full DM particle distribution results do qualitatively agree with them.

Of course, HV02 is based on halo positions and so it will by definition not see any decrease in information (as the extra information is not there to begin with). Indeed, Colberg et al. (2008) show that the voids found by HV02 are very different. They seem bounded by overdensities of haloes, not just by any overdensity. This poses the question: why are HV02 voids still sensitive to changes in w_a (or σ_8), whereas WVF+DTFE voids based on halo data are not? What do the HV02 voids probe that the WVF+DTFE halo voids do not? To this question we have no clear answer. It seems to us that WVF+DTFE actually probes the cosmic web in more detail than HV02 can. It should therefore contain more information. It could be, however, that the added information actually obscures the information we are looking for. In other words, the extra information acts as noise.

Another possibility may be that the DTFE method is not suited for sparsely probed distributions like halo distributions. It may contain artefacts due to the coarseness of the resulting Delaunay tessellation. These might be the cause of the noise mentioned above.

Lavaux and Wandelt (2010) use yet another void finding algorithm (henceforth called LW10). This one uses more information than WVF+DTFE. They include both particle positions and velocities. Of course the result is then expected to differ from that of WVF+DTFE, as what is probed is physically different from the WVF+DTFE voids.

⁴They conclude from this that the deviation from the σ_8 that was used as input for the initial conditions can be corrected for. However, to correct for this, the original value of σ_8 is necessary. In observations this value is only available through secondary measures.

Whether these “phase-space voids” from LW10 are better probes of the cosmological parameters remains to be seen. At least it seems that WVF is superior in identifying the voids that we also identify by eye. Platen (2009) also showed that the void shapes inferred from WVF align very accurately with the tidal tensor eigenvectors. This made it especially suited for testing the claimed relations of Park and Lee (2007), as they derived their relations from the tidal field as well. It may, however, turn out that the inclusion of velocities is crucial in the pinning down of the cosmological model.

Whatever the case, a detailed comparison of the voids found by all these different methods should be made (as already suggested by Colberg et al. (2008)). If we are to properly compare the results of our analyses, the role of the different methods needs to be understood. The current plethora of void definitions sometimes seems to obscure important differences rather than enlighten our analyses. A proper distinction in e.g. static/position-space and dynamical/phase-space voids should be made (where we would actually prefer to not call the latter class voids, but rather something like ‘cosmic outflow regions’).

Related to this discussion is an interesting remark that Park and Lee (2007) make at the end of their paper: “We expect that our numerical result would not change sensitively with respect to the void-finding algorithm, given the fact that the ellipticity of a void here is defined in terms of the spatial distribution of galaxies that make up the void but not by the boundary shape of a void.” In other words, they claim that an essential point may be that not the voids themselves but the distribution of haloes in the voids are sensitive to changes in the dark energy model. It may be that indeed there is a significant difference between the two. It seems, however, that it may make observations even harder to realize, as there are scant numbers of galaxies in voids. It is in any case an interesting point that deserves further study. This requires a far more detailed account of the halo distribution and also a thorough comparison of different halo finders and halo definitions.

Extended quintessence models

A remarkable, though little emphasised fact is that the EQ models differ so slightly from the other models of DE. Although their physical basis is radically different from the other models - coupling through gravity versus no coupling at all except through the Friedmann equation - they constitute only a moderate alteration of standard cosmology compared with e.g. a SUGRA model, which all the four models differ radically from.

It seems likely that the constraints on the coupling constant from Acquaviva et al. (2005) were too stringent to really make a difference. As our analysis shows, this will make it hard to distinguish between Λ CDM and a universe with EQ. Whether or not this makes the distinction irrelevant is a question we cannot answer without further investigation into other possible probes. It may be that other probes are more sensitive to effects from EQ. Probes from the era of matter dominance, where EQn differs the most from EQp (Pettorino and Baccigalupi, 2008), may for example enable us to discard at least one of the models.

We briefly summarize the main findings of this thesis.

Our main question was whether voids could be used as probes of the nature of dark energy in real observations. We have investigated one-point pdfs, two-point correlation functions, (modified) void probability functions and void shape parameters. We concluded that *neither of these probes are suitable for discerning models of DE in real observations*. The three main reasons for this are *redshift distortions, the sparsity of the halo sample (discreteness effects) and the spatial distribution of the halo sample (complex biasing)*.

We also compared our high resolution results to similar results from the literature (Lee and Park, 2009; Lavaux and Wandelt, 2010). *We found a strong correlation of mean void ellipticity with σ_8* . This correlation explains our results as well as those from the literature, without the need for the claimed redshift dependence of mean void ellipticity. *We conclude that the void ellipticity evolution is a probe of σ_8 , not of the nature of dark energy*. Possible constraints on DE models from this probe may only be attained by combining results with other independent probes.

We further conclude that a *thorough comparison of void finding algorithms is desirable* to be able to properly compare results from different algorithms. The same goes for halo finders: Park and Lee (2007) suggest that a crucial detail in their void shape determination is that they use haloes instead of the void itself. *The extended quintessence models may contain some interesting new information* that further research may uncover, especially with respect to the era of matter dominance (as mentioned in section 1.2.2 and in Pettorino and Baccigalupi (2008)). Finally, there is some *room for improvement for the MVPF*. It may be useful to try to apply the MVPF on a density field instead of on a particle distribution.

ACKNOWLEDGEMENTS

Many thanks go out to a lot of people for helping me in various ways through the course of this project.

This project was initially meant to be a collaboration between Rien and I and Roman Juskiwicz and Wojciech Hellwing, but due to a shift in the project's focus, this collaboration never really got off the ground. However, the project would never have started if it were not for these two people and for this, the good discussions on the subject and the useful ideas in the starting phase, I want to express my deepest gratitude.

The mentioned shift in focus was caused by the unexpected data we were provided with by Klaus Dolag. He already had exactly the right data for our project, which meant that we could skip doing the simulations ourselves and focus on the analysis of the data. He also provided us with an advanced non-public version of the GADGET code by Volker Springel.

I also want to thank all the members of Rien's posse. Obviously, I owe Rien himself for his great overall advise as my supervisor on this project. Other great contributions were made by Erwin Platen, Marius Cautun, Pablo Araya Melo, Johan Hidding and Wendy Docters. Erwin helped me with two of the key ingredients of this work, the DTFE and the WVF, as well as with general hints and advise on other matters. With Marius' help I figured out the intricate details of GADGET simulations and other technical matters like power spectrum estimation. Pablo helped me set up the basics of what was needed to simulate the things we did. Johan, being an expert on making damned pretty pictures, gave me some essential plotting tips and also helped me in implementing the details of discrete fourier transformations. Wendy helped with the Fourier transformations as well as giving me a vital heads-up on an error in my initial conditions generator. Another special thanks goes out to Keimpe Nevenzeel for proofreading chapter 1. And in general, I want to thank all the members of Rien's group for the many useful discussions we had.

A large part of the project was spent programming. Luckily, the Kapteyn Institute harbors some excellent programming talents. In particular I want to thank Maarten Breddels for his suggestion of a lot of useful computational methods and libraries. Further kudos go out to Hugo Buddelmeijer, Jarno Ruwen, Derek Land and Jakob van Bethlehem, all of whom have more than once saved me in my adventures through programming land. For some very useful, time saving tips on the CGAL library I owe Manuel Caroli my thanks. And of course, I want to thank the Kapteyn Computer Group, Martin Vogelaar, Eite Tiesinga, Wim Zwitser and Hans Terlouw, for their invaluable hardware

and software support.

A great deal of thanks go out to the people around me that were there in the times when I was not working. To all the students of the Kapteyn: thanks for keeping me off my work every now and then. The daily discussions over coffee, though usually quite useless, were nonetheless very entertaining! Special thanks go out to Jarno Ruwen for his expertise in the brewing of dark energy (see section A for a sample) and Eva Busekool for the logistics behind this effort. I thank my fellow members of the board of the Bètastuf, Wouter Oosterheert, Jaap Oosterbroek and Jasper van Dijk, for a year of further distraction, but also a year of fruitful cooperation and especially for their mental support during the final weeks of this project.

I want to thank my friends, especially Gerwin de Boer, Jos Dontje and Nick Ziegls, for the steady supply of cold beers and yoghurt-drinks, for the overall gezelligheid after work hours and for their neverending effort to get me to start watching soccer.

Finally, I want to thank Femke van der Honing and my family for their interest, love and support.

- Acquaviva, V., Baccigalupi, C., Leach, S. M., Liddle, A. R., and Perrotta, F. (2005). Structure formation constraints on the Jordan-Brans-Dicke theory. *PhRvD*, 71(10):id.104025.
- Amanullah, R., Lidman, C., Rubin, D., Aldering, G., Astier, P., Barbary, K., Burns, M. S., Conley, A., Dawson, K. S., Deustua, S. E., Doi, M., Fabbro, S., Faccioli, L., Fakhouri, H. K., Folatelli, G., Fruchter, A. S., Furusawa, H., Garavini, G., Goldhaber, G., Goobar, A., Groom, D. E., Hook, I., Howell, D. A., Kashikawa, N., Kim, A. G., Knop, R. A., Kowalski, M., Linder, E., Meyers, J., Morokuma, T., Nobili, S., Nordin, J., Nugent, P. E., Östman, L., Pain, R., Panagia, N., Perlmutter, S., Raux, J., Ruiz-Lapuente, P., Spadafora, A. L., Strovink, M., Suzuki, N., Wang, L., Wood-Vasey, W. M., Yasuda, N., and Supernova Cosmology Project, T. (2010). Spectra and Hubble Space Telescope Light Curves of Six Type Ia Supernovae at 0.511 μ m and 1.12 μ m and the Union2 Compilation. *ApJ*, 716(1):712–738.
- Aragón Calvo, M. A. (2007). *Morphology and Dynamics of the Cosmic Web*. PhD thesis, Rijksuniversiteit Groningen.
- Arbabi-Bidgoli, S. and Müller, V. (2002). Void scaling and void profiles in cold dark matter models. *MNRAS*, 332(1):205–214.
- Baccigalupi, C., Matarrese, S., and Perrotta, F. (2000). Tracking extended quintessence. *PhRvD*, 62(12):id.123510.
- Bagla, J. S. and Ray, S. (2003). Performance characteristics of TreePM codes. *NewA*, 8(7):665–677.
- Betancort-Rijo, J., Patiri, S. G., Prada, F., and Romano, A. E. (2009). The statistics of voids as a tool to constrain cosmological parameters: Ω_m and Ω_b . *MNRAS*, 400(4):1835–1849.
- Biswas, R., Alizadeh, E., and Wandelt, B. D. (2010). Voids as a Precision Probe of Dark Energy. *arXiv:1002.0014*.
- Boisseau, B., Esposito-Farèse, G., Polarski, D., and Starobinsky, A. A. (2000). Reconstruction of a Scalar-Tensor Theory of Gravity in an Accelerating Universe. *PhRvL*, 85(11):2236–2239.

- Bond, J. R., Kofman, L., and Pogosyan, D. (1996). How filaments of galaxies are woven into the cosmic web. *Nature*, 380(6575):603–606.
- Brax, P. and Martin, J. (2000). Robustness of quintessence. *PhRvD*, 61(10):id.103502.
- Caldwell, Robert R.; Kamionkowski, M. (2009). The Physics of Cosmic Acceleration. *ARNPS*, 59:397–429.
- Chincarini, G. and Rood, H. J. (1975). Size of the Coma cluster. *Nature*, 257:294, 295.
- Cimatti, A., Leibundgut, B., Lilly, S., Nichol, R., Refregier, A., Rosati, P., Steinmetz, M., Thatte, N., Valentijn, E., Amara, A., Baugh, C., Guzzo, L., Longair, M., Wang, Y., Boisnard, L., Duvet, L., Lumb, D., and Saavedra Criado, G. (2009). Euclid Science Requirements Document. *ESA Science document*, (2). Reference: DEM-SA-Dc-00001.
- Colberg, J. M., Pearce, F., Foster, C., Platen, E., Brunino, R., Neyrinck, M., Basilakos, S., Fairall, A., Feldman, H., Gottlöber, S., Hahn, O., Hoyle, F., Müller, V., Nelson, L., Plionis, M., Porciani, C., Shandarin, S., Vogeley, M. S., and van de Weygaert, R. (2008). The Aspen-Amsterdam void finder comparison project. *MNRAS*, 387(2):933–944.
- Colberg, J. M., Sheth, R. K., Diaferio, A., Gao, L., and Yoshida, N. (2005). Voids in a LCDM universe. *MNRAS*, 360(1):216–226.
- Copeland, E. J., Sami, M., and Tsujikawa, S. (2006). Dynamics of Dark Energy. *IJMPD*, 15(11):1753–1935.
- Davis, M., Efstathiou, G., Frenk, C. S., and White, S. D. M. (1985). The evolution of large-scale structure in a universe dominated by cold dark matter. *ApJ*, 292(1):371–394.
- Davis, M. and Peebles, P. J. E. (1983). A survey of galaxy redshifts. V - The two-point position and velocity correlations. *ApJ*, 267(1):465–482.
- Dolag, K., Bartelmann, M., Perrotta, F., Baccigalupi, C., Moscardini, L., Meneghetti, M., and Tormen, G. (2004). Numerical study of halo concentrations in dark-energy cosmologies. *A&A*, 416:853–864.
- Dolag, K., Pettorino, V., Moscardini, L., Bacci, C., Meneghetti, M., Bartelmann, M., and De Boni, C. (2010). Hydrodynamical simulations of galaxy clusters in Dark Energy cosmologies. *MNRAS*. In preparation.
- Dubinski, J., da Costa, L. N., Goldwirth, D. S., Lecar, M., and Piran, T. (1993). Void evolution and the large-scale structure. *ApJ*, 410(2):458–468.
- Einasto, J., Einasto, M., Gramann, M., and Saar, E. (1991). Structure and formation of superclusters. XIII - The void probability function. *MNRAS*, 248:593–605.
- Einasto, J., Joveer, M., and Saar, E. (1980). Superclusters and galaxy formation. *Nature*, 283:47, 48.
- Foster, C. and Nelson, L. A. (2009). The Size, Shape, and Orientation of Cosmological Voids in the Sloan Digital Sky Survey. *ApJ*, 699(2):1252–1260.

- Freedman, D., van Nieuwenhuizen, P., and Ferrara, S. (1976). Progress Toward A Theory Of Supergravity. *PhRvD*, 13:3214–3218.
- Frieman, J. A., Turner, M. S., and Huterer, D. (2008). Dark Energy and the Accelerating Universe. *ARA&A*, 46:385–432.
- Furlanetto, S. R. and Piran, T. (2006). The evidence of absence: galaxy voids in the excursion set formalism. *MNRAS*, 366(2):467–479.
- Gregory, S. A. and Thompson, L. A. (1978). The Coma/A1367 supercluster and its environs. *ApJ*, 222(1):784–799.
- Groth, E. J. and Peebles, P. J. E. (1977). Statistical analysis of catalogs of extragalactic objects. VII - Two- and three-point correlation functions for the high-resolution Shane-Wirtanen catalog of galaxies. *ApJ*, 217(1):385–405.
- Hahn, O., Porciani, C., Carollo, C. M., and Dekel, A. (2007). Properties of dark matter haloes in clusters, filaments, sheets and voids. *MNRAS*, 375(2):489–499.
- Hamilton, A. J. S. (1993). Toward Better Ways to Measure the Galaxy Correlation Function. *ApJ*, 417:19.
- Hawking, S. W. and Ellis, G. F. R. (1973). *The large-scale structure of space-time*. Cambridge University Press.
- Hicken, M., Wood-Vasey, W. M., Blondin, S., Challis, P., Jha, S., Kelly, P. L., Rest, A., and Kirshner, R. P. (2009). Improved Dark Energy Constraints from 100 New CfA Supernova Type Ia Light Curves. *ApJ*, 700(2):1097–1140.
- Holtzman, J. A., Marriner, J., Kessler, R., Sako, M., Dilday, B., Frieman, J. A., Schneider, D. P., Bassett, B., Becker, A., Cinabro, D., DeJongh, F., Depoy, D. L., Doi, M., Garnavich, P. M., Hogan, C. J., Jha, S., Konishi, K., Lampeitl, H., Marshall, J. L., McGinnis, D., Miknaitis, G., Nichol, R. C., Prieto, J. L., Riess, A. G., Richmond, M. W., Romani, R., Smith, M., Takahashi, N., Tokita, K., van der Heyden, K., Yasuda, N., and Zheng, C. (2008). The Sloan Digital Sky Survey-II: Photometry and Supernova IA Light Curves from the 2005 Data. *AJ*, 136(6):2306–2320.
- Hoyle, F. and Vogeley, M. S. (2002). Voids in the Point Source Catalogue Survey and the Updated Zwicky Catalog. *ApJ*, 566(2):641–651.
- Huterer, D. and Turner, M. S. (1999). Prospects for probing the dark energy via supernova distance measurements. *PhRvD*, 60(8):id.081301.
- Huterer, D. and Turner, M. S. (2001). Probing dark energy: Methods and strategies. *PhRvD*, 64(12):123527.
- Icke, V. (1984). Voids and filaments. *MNRAS*, 206:1P–3P.
- Jennings, E., Baugh, C. M., and Pascoli, S. (2010). Modelling redshift space distortions in hierarchical cosmologies. *eprint arXiv:1003.4282*.
- Kaiser, N. (1987). Clustering in real space and in redshift space. *MNRAS*, 227:1–21.

- Kirshner, R. P., Oemler, A., J., Schechter, P. L., and Shectman, S. A. (1981). A million cubic megaparsec void in Bootes. *ApJ*, 248:L57–L60.
- Komatsu, E., Smith, K. M., Dunkley, J., Bennett, C. L., Gold, B., Hinshaw, G., Jarosik, N., Larson, D., Nolte, M. R., Page, L., Spergel, D. N., Halpern, M., Hill, R. S., Kogut, A., Limon, M., Meyer, S. S., Odegard, N., Tucker, G. S., Weiland, J. L., Wollack, E., and Wright, E. L. (2010). Seven-Year Wilkinson Microwave Anisotropy Probe (WMAP) Observations: Cosmological Interpretation. *eprint arXiv:1001.4538*.
- Kowalski, M., Rubin, D., Aldering, G., Agostinho, R. J., Amadon, A., Amanullah, R., Bannard, C., Barbary, K., Blanc, G., Challis, P. J., Conley, A., Connolly, N. V., Covarrubias, R., Dawson, K. S., Deustua, S. E., Ellis, R., Fabbro, S., Fadeyev, V., Fan, X., Farris, B., Folatelli, G., Frye, B. L., Garavini, G., Gates, E. L., Germany, L., Goldhaber, G., Goldman, B., Goobar, A., Groom, D. E., Haissinski, J., Hardin, D., Hook, I., Kent, S., Kim, A. G., Knop, R. A., Lidman, C., Linder, E. V., Mendez, J., Meyers, J., Miller, G. J., Moniez, M., Mouro, A. M., Newberg, H., Nobili, S., Nugent, P. E., Pain, R., Perdureau, O., Perlmutter, S., Phillips, M. M., Prasad, V., Quimby, R., Regnault, N., Rich, J., Rubenstein, E. P., Ruiz-Lapuente, P., Santos, F. D., Schaefer, B. E., Schommer, R. A., Smith, R. C., Soderberg, A. M., Spadafora, A. L., Strolger, L.-G., Strovink, M., Suntzeff, N. B., Suzuki, N., Thomas, R. C., Walton, N. A., Wang, L., Wood-Vasey, W. M., and Yun, J. L. (2008). Improved Cosmological Constraints from New, Old, and Combined Supernova Data Sets. *ApJ*, 686(2):749–778.
- Lachièze-Rey, M. and Maurogordato, S. (1987). The Void Probability Function as a Statistical Indicator. *Observational Cosmology; Proceedings of the IAU Symposium*, page 359.
- Landy, S. D. and Szalay, A. S. (1993). Bias and variance of angular correlation functions. *ApJ*, 412(1):64–71.
- Larson, D., Dunkley, J., Hinshaw, G., Komatsu, E., Nolte, M. R., Bennett, C. L., Gold, B., Halpern, M., Hill, R. S., Jarosik, N., Kogut, A., Limon, M., Meyer, S. S., Odegard, N., Page, L., Smith, K. M., Spergel, D. N., Tucker, G. S., Weiland, J. L., Wollack, E., and Wright, E. L. (2010). Seven-Year Wilkinson Microwave Anisotropy Probe (WMAP) Observations: Power Spectra and WMAP-Derived Parameters. *eprint arXiv:1001.4635*.
- Lavaux, G. and Wandelt, B. D. (2010). Precision cosmology with voids: definition, methods, dynamics. *MNRAS*, 403(3):1392–1408.
- Lee, J. and Park, D. (2009). Constraining the Dark Energy Equation of State with Cosmic Voids. *ApJ*, 696(1):L10–L12.
- Leibundgut, B. (2001). Cosmological Implications from Observations of Type Ia Supernovae. *ARA&A*, 39:67–98.
- Linder, E. V. (2003). Exploring the Expansion History of the Universe. *PhRvL*, 90(9):091301.
- Linder, E. V. (2008). The dynamics of quintessence, the quintessence of dynamics. *GR&Gr*, 40(2-3):329–356.

- Linder, E. V. (2010). Constraining Models of Dark Energy. *ARXIV*, page 1004.4646.
- Martinez, V. J. and Saar, E. (2002). *Statistics of the Galaxy Distribution*. Chapman & Hall/CRC.
- Maurogordato, S. (2006). The Void Probability function and related statistics. In *Cosmic voids: much ado about nothing*. Presentation at a colloquium at the Trippenhuis, Amsterdam, The Netherlands.
- Montero-Dorta, A. D. and Prada, F. (2009). The SDSS DR6 luminosity functions of galaxies. *MNRAS*, 399(3):1106–1118.
- Müller, V., Arbabi-Bidgoli, S., Einasto, J., and Tucker, D. (2000). Voids in the Las Campanas Redshift Survey versus cold dark matter models. *MNRAS*, 318(1):280–288.
- Neyrinck, M. C. (2008). ZOBOV: a parameter-free void-finding algorithm. *MNRAS*, 386(4):2101–2109.
- Ostriker, J. P. and Steinhardt, P. J. (1995). Cosmic Concordance. *eprint arXiv:astro-ph/9505066*.
- Park, D. and Lee, J. (2007). Void Ellipticity Distribution as a Probe of Cosmology. *PhRvL*, 98(8):id.081301.
- Peebles, P. J. E. (1973). Statistical Analysis of Catalogs of Extragalactic Objects. I. Theory. *ApJ*, 185:413–440.
- Peebles, P. J. E. and Groth, E. J. (1976). An integral constraint for the evolution of the galaxy two-point correlation function. *A&A*, 53(1):131–140.
- Pelupessy, F. I., Schaap, W. E., and van de Weygaert, R. (2003). Density estimators in particle hydrodynamics. DTFE versus regular SPH. *A&A*, 403:389–398.
- Percival, W. J. and White, M. (2009). Testing cosmological structure formation using redshift-space distortions. *MNRAS*, 393(1):297–308.
- Perlmutter, S., Aldering, G., Goldhaber, G., Knop, R. A., Nugent, P., Castro, P. G., Deustua, S., Fabbro, S., Goobar, A., Groom, D. E., Hook, I. M., Kim, A. G., Kim, M. Y., Lee, J. C., Nunes, N. J., Pain, R., Pennypacker, C. R., Quimby, R., Lidman, C., Ellis, R. S., Irwin, M., McMahon, R. G., Ruiz-Lapuente, P., Walton, N., Schaefer, B., Boyle, B. J., Filippenko, A. V., Matheson, T., Fruchter, A. S., Panagia, N., Newberg, H. J. M., Couch, W. J., and Project, T. S. C. (1999). Measurements of Omega and Lambda from 42 High-Redshift Supernovae. *ApJ*, 517(2):565–586.
- Perrotta, F. and Baccigalupi, C. (2002). On the dark energy clustering properties. *PhRvD*, 65(12):id.123505.
- Perrotta, F., Baccigalupi, C., and Matarrese, S. (2000). Extended quintessence. *PhRvD*, 61(2):id.023507.
- Pettorino, V. and Baccigalupi, C. (2008). Coupled and extended quintessence: Theoretical differences and structure formation. *PhRvD*, 77(10):id.103003.

- Pettorino, V., Baccigalupi, C., and Perrotta, F. (2005). On the dark energy clustering properties. *JCAP*, (12):003.
- Phillips, M. M. (1993). The absolute magnitudes of Type IA supernovae. *ApJL*, 413(2):L105–L108.
- Platen, E. (2009). *A Void Perspective of the Cosmic Web*. PhD thesis, Rijksuniversiteit Groningen.
- Platen, E., van de Weygaert, R., and Jones, B. J. T. (2007). A cosmic watershed: the WVF void detection technique. *MNRAS*, 380(2):551–570.
- Platen, E., van de Weygaert, R., and Jones, B. J. T. (2008). Alignment of voids in the cosmic web. *MNRAS*, 387(1):128–136.
- Plionis, M. and Basilakos, S. (2002). The size and shape of local voids. *MNRAS*, 330(2):399–404.
- Press, W. H. and Davis, M. (1982). How to identify and weigh virialized clusters of galaxies in a complete redshift catalog. *ApJ*, 259(1):449–473.
- Primack, J. R. and Abrams, N. E. (2007). *The View From the Center of the Universe: Discovering Our Extraordinary Place in the Cosmos*. Riverhead Trade.
- Ratra, B. and Peebles, P. J. E. (1988). Cosmological consequences of a rolling homogeneous scalar field. *PhRvD*, 37(12):3406–3427.
- Riess, A. G., Filippenko, A. V., Challis, P., Clocchiatti, A., Diercks, A., Garnavich, P. M., Gilliland, R. L., Hogan, C. J., Jha, S., Kirshner, R. P., Leibundgut, B., Phillips, M. M., Reiss, D., Schmidt, B. P., Schommer, R. A., Smith, R. C., Spyromilio, J., Stubbs, C., Suntzeff, N. B., and Tonry, J. (1998). Observational Evidence from Supernovae for an Accelerating Universe and a Cosmological Constant. *AJ*, 116(3):1009–1038.
- Rivolo, A. R. (1986). The two-point galaxy correlation function of the Local Supercluster. *AA*, 301(1):70–76.
- Ryden, B. S. and Melott, A. L. (1996). Voids in Real Space and in Redshift Space. *ApJ*, 470:160.
- Schaap, W. E. (2007). *DTFE: the Delaunay Tessellation Field Estimator*. PhD thesis, Rijksuniversiteit Groningen.
- Schaap, W. E. and van de Weygaert, R. (2000). Continuous fields and discrete samples: reconstruction through Delaunay tessellations. *A&A*, 363:L29–L32.
- Shandarin, S., Feldman, H. A., Heitmann, K., and Habib, S. (2006). Shapes and sizes of voids in the Lambda cold dark matter universe: excursion set approach. *MNRAS*, 367(4):1629–1640.
- Sheth, R. K. (1996). Random dilutions, generating functions, and the void probability distribution function. *MNRAS*, 278(1):101–110.
- Sheth, R. K. and van de Weygaert, R. (2004). A hierarchy of voids: much ado about nothing. *MNRAS*, 350(2):517–538.

- Springel, V. (2005). The cosmological simulation code **GADGET-2**. *MNRAS*, 364(4):1105–1134.
- Springel, V., White, S. D. M., Jenkins, A., Frenk, C. S., Yoshida, N., Gao, L., Navarro, J., Thacker, R., Croton, D., Helly, J., Peacock, J. A., Cole, S., Thomas, P., Couchman, H., Evrard, A., Colberg, J., and Pearce, F. (2005). Simulations of the formation, evolution and clustering of galaxies and quasars. *Nature*, 435(7042):629–636.
- Springel, V., White, S. D. M., Tormen, G., and Kauffmann, G. (2001). Populating a cluster of galaxies - I. Results at $z=0$. *MNRAS*, 328(3):726–750.
- Stanonik, K., Platen, E., Aragon-Calvo, M. A., van Gorkom, J. H., van de Weygaert, R., van der Hulst, J. M., Kovac, K., Yip, C. W., and Peebles, P. J. E. (2009a). Only the Lonely: HI Imaging of Void Galaxies. *eprint arXiv*, page 0909.2869.
- Stanonik, K., Platen, E., Aragón-Calvo, M. A., van Gorkom, J. H., van de Weygaert, R., van der Hulst, J. M., and Peebles, P. J. E. (2009b). Polar Disk Galaxy Found in Wall Between Voids. *ApJL*, 696(1):L6–L9.
- Szapudi, I. (1998). A New Method for Calculating Counts in Cells. *ApJ*, 497(2):16.
- Tegmark, M. and Peebles, P. J. E. (1998). The Time Evolution of Bias. *ApJL*, 500:L79.
- van de Weygaert, R. and Platen, E. (2009). Cosmic Voids: structure, dynamics and galaxies. *arXiv*, page 0912.2997. invited review COSPA2008.
- van de Weygaert, R., Platen, E., Tigrak, E., Hidding, J., van der Hulst, T., Aragon-Calvo, M. A., Stanonik, K., and van Gorkom, J. (2009). The Cosmically Depressed: Life, Sociology and Identity of Voids. *eprint arXiv:0912.3473*.
- van de Weygaert, R. and van Kampen, E. (1993). Voids in Gravitational Instability Scenarios - Part One - Global Density and Velocity Fields in an Einstein - De-Sitter Universe. *MNRAS*, 263(2):481.
- van Riet, T. (2007). *Cosmic Acceleration in Kaluza-Klein Supergravity*. PhD thesis, Rijksuniversiteit Groningen.
- Vogeley, M. S., Geller, M. J., and Huchra, J. P. (1991). Void statistics of the CfA redshift survey. *ApJ*, 382(1):44–54.
- Wetterich, C. (1988). Cosmologies with variable Newton’s “constant”. *Nuclear Physics B*, 302(4):645–667.
- White, S. D. M. (1979). The hierarchy of correlation functions and its relation to other measures of galaxy clustering. *MNRAS*, 186:145–154.
- Xu, G. (1995). A New Parallel N-Body Gravity Solver: TPM. *ApJS*, 98:355.
- Zel’Dovich, Y. B. (1970). Gravitational instability: An approximate theory for large density perturbations. *A&A*, 5:84–89.

APPENDIX A

COFFEE AND CREAM

Apart from being the great catalyst of science we know, love and could not live without, coffee, our daily dose of dark energy, can serve a broader purpose as a tool in science outreach activities. The recipe is simple. Take one hot cup of coffee and pour in a decent amount of cream. Now, just put the cup down and wait a few minutes. Soon, filaments will start forming as in figure A.1(a) (highlighted in figure A.1(b)). Because of their constant evolution (see figure A.1(c), which was taken only a few seconds later) we can imagine the coffee surface to represent a fly-through of the 3D large scale structure, i.e. it automatically loops through adjacent slices of the 3D distribution. When the cream is stirred through properly as in figure A.1(d) we have the initial homogeneous state of the universe.

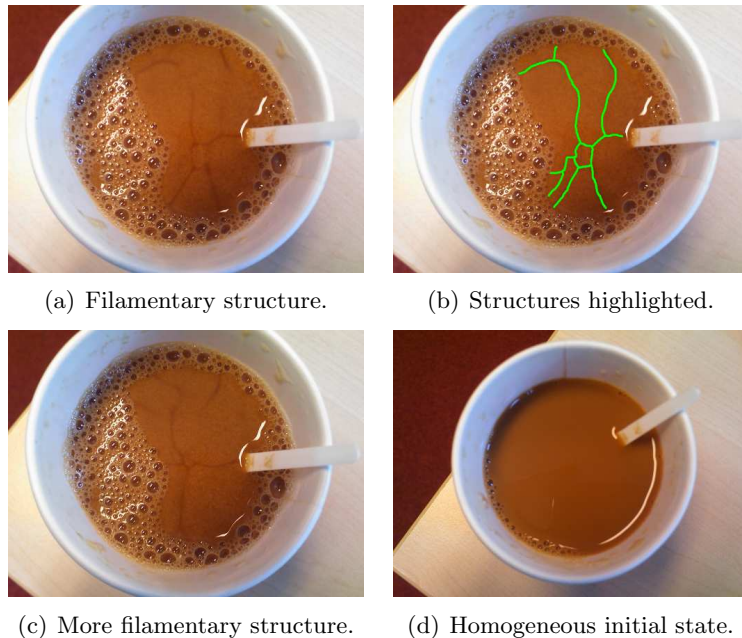


Figure A.1: Simulations of the large scale structure of the universe in a cup of coffee with cream.

APPENDIX B

“CONCORDANCE” COSMOLOGY

A term first coined in an unpublished paper (Ostriker and Steinhardt, 1995), concordance cosmology is what we call our current standard model of the universe. The following is a list of key concepts in the understanding of this model:

- The cosmological principle
- The Friedmann-Lemaître-Robertson-Walker (FLRW) metric
- The Friedmann equations

In this section we will highlight some of the steps necessary to describe this model of the universe. A more detailed derivation, dealing in particular with the addition of scalar fields like quintessence, can be found in van Riet (2007).

The cosmological principle states that on large enough scales (say $\gtrsim 8h^{-1}$ Mpc) the universe is homogeneous and isotropic, i.e. matter and energy are distributed evenly and in every direction we see roughly the same things. When applied to Einstein’s general relativistic field equations, this yields a simplification of the description of (the geometry of) the universe in the form of the FLRW metric¹. In its most general form, this metric can be written as follows:

$$ds^2 = c^2 dt^2 - a(t) dx^2, \quad (\text{B.2})$$

where s is the distance between two points in space-time, x is the (three-dimensional) space coordinate and $a(t)$ is the time dependent scale factor which describes the uniform expansion (or contraction) of an FLRW universe.

In general relativity, we can describe the density and flux of energy and matter with the energy-momentum tensor T_{ij} . The geometry of space-time on the other hand is described by the metric tensor g_{ij} . Einstein coupled these two quantities in the so-called Einstein equation:

$$G_{ij} - \Lambda g_{ij} = \frac{8\pi G}{c^4} T_{ij}, \quad (\text{B.3})$$

¹A metric describes the geometry of space-time in general relativity. In general we can write this as

$$ds^2 = g_{ij}(x) dx^i dx^j, \quad (\text{B.1})$$

where x is a four-dimensional space-time coordinate, s is the distance between two points in space-time and $g_{ij}(x)$ is the metric tensor. We use the Einstein summation convention for vector and tensor indices.

where G_{ij} is the Einstein tensor², Λ is the cosmological constant and G and c are Newton's gravitational constant and the speed of light respectively.

We can combine the FLRW metric given in equation B.2 with the Einstein equation to find the dynamical equations that govern energy and matter in a homogeneous and isotropic universe. These dynamical equations are called the Friedmann equations and they are the following:

$$\left(\frac{\dot{a}}{a}\right)^2 = \frac{8\pi G}{3}\rho - \frac{kc^2}{a^2} + \frac{\Lambda c^2}{3} = \frac{8\pi G}{3}\rho' - \frac{kc^2}{a^2} \quad (\text{B.4})$$

$$\frac{\ddot{a}}{a} = -\frac{4\pi G}{3}\left(\rho + \frac{3p}{c^2}\right) + \frac{\Lambda c^2}{3} = -\frac{4\pi G}{3}\left(\rho' + \frac{3p'}{c^2}\right) \quad (\text{B.5})$$

$$\dot{\rho} = -3\frac{\dot{a}}{a}\left(\rho + \frac{p}{c^2}\right), \quad (\text{B.6})$$

where ρ is density in units of kg, k is the curvature parameter (which is -1 , 0 or 1 for respectively an open/hyperbolic universe, a flat/Euclidian universe or a closed/spherical universe), describing the overall geometry of the universe, and p is a pressure. To solve these equations one more equation is needed and that is the equation of state of the several components of the universe. Assuming these components behave as perfect collisionless fluids (which is a decent assumption on universal scales) we can write them as

$$p_i = w_i \rho_i, \quad (\text{B.7})$$

where now ρ_i is the energy density of a certain universal constituent, w_i is the associated equation of state parameter (which can vary in time) and p_i is the pressure that is defined by this equation.

²The Einstein tensor is made up of the metric tensor and its first and second derivatives.

Below we include the original research plan. We have deviated significantly from this, because the high resolution data, kindly and on forehand unexpectedly provided by Klaus Dolag, proved more than sufficient for our analyses. The time planning turned out to be a little on the tight side, but we managed in the end.

C.1 Motivation and goals

Cosmology is currently widely held to be in a so-called state of ‘concordance’, which gives the impression that all of the main cosmological questions are answered. Observational limits however still leave considerable room for cosmological models other than the standard Λ CDM model with concordance parameters. Together with Rien van de Weijgaert, Roman Juszkiewicz¹ and his PhD student Wojciech Hellwing we want to set up a collaboration on inspecting void properties and other cosmological statistics in non-standard cosmological models. We thus hope to find observable cosmological probes of the specific non-standard models in question.

Rien and I will look specifically at models with non-standard descriptions of dark energy, while Roman and Wojciech investigate models with modified gravity. The models we will definitely try to investigate are that of $w \neq -1$ and quintessence (which uses a time dependent w). Another possible model to include (when time allows) is that of a Chaplygin gas in which dark matter and dark energy are coupled and maybe along the way we will find other interesting models to investigate.

C.2 Methods

We will run several N-body numerical experiments of these modified cosmologies using the GADGET-2 code. We will implement the non-standard models in the code ourselves, run these on initial conditions of a Gaussian random field propagated to a suitable redshift using the Zel’dovich approximation and compare them to runs with standard Λ CDM model and parameters. We hope to do several of these runs for each parameter/model set to be able to draw statistically significant conclusions.

¹Nicolaus Copernicus Astronomical Center, Warsaw, Poland

Our main cosmological probe will be voids, which because of their large scale nature are expected to be sensitive probes of the dark energy model, dark energy being a large scale (both spatially and temporally) cosmological component. Void finding algorithms, like the Watershed Void Finder by Erwin Platen, will be invaluable to this analysis. Other possible probes include baryonic acoustic oscillations, clustering properties and more standard cosmological statistics like the power spectrum.

One of the important aspects of the project is to be able to produce observational probes. This means that it would be a great asset to include baryonic matter in the simulations, otherwise our probes would be limited to indirect observational evidence through the effects of dark matter only. GADGET-2 is capable of handling SPH simulations, which is a possible way to include this. Perhaps more importantly we need our probes to be useful in redshift space as opposed to normal space, because this is currently the only viable means of radial distance estimation on the cosmological scales we are interested in.

C.3 Research plan

Here we give a somewhat more structured plan of the steps involved in the project and the time they are expected to take. The Groot Onderzoek project is worth 60 ECTS, equivalent to 1680 hours of work, 210 full 8 hour days, 42 full 5 day weeks. Officially starting in September 2009 this means that we should be done at the end of June 2010, assuming full time commitment, which is the intention (all other requirements for the MSc Astronomy are fulfilled). However, because we have already done some 6 weeks of preliminary work, there should be some extra breathing space. We will nevertheless put forward a planning that covers the weeks from September 2009 up to and including June 2010 in which the first steps have already been covered, leaving us with a slight headstart and thus giving us some extra time during the year.

<i>Task</i>	<i>Weeks</i>
Literature study of the subject	36-38
Figuring out which exact situations we should simulate	39,40
Getting to know the N-body software	41,42
<i>BREAK (trip to Madrid and wedding)</i>	43
Building initial conditions	44-46
Running Λ CDM simulations with pure DM ...	47
... and with baryonic matter as well	48
Modifying the N-body software for the non-standard simulations	47,48
Running non-standard simulations with pure DM ...	49
... and with baryonic matter as well	50
Getting to know the void finding and other statistical software	50,51
<i>BREAK (Christmas vacation)</i>	52,53
Converting from x,y,z to x,y,redshift space	1,2
Obtaining void statistics for the simulations we have run	3-5
Obtaining other statistics	6-8
Analysis and comparison of statistics	9-11
Writing the thesis and tying up loose ends	12-24
Preparing and giving presentation	25,26